Probing Cell Mechanotransduction and Electric Activity with Microfluidic Platforms

By

Lijie Yang

Dissertation
Submitted to the Faculty of the
Graduate School of Vanderbilt University
in partial fulfillment of the requirements
for the degree of

DOCTOR OF PHILOSOPHY
in

Mechanical Engineering
June 30, 2017
Nashville, Tennessee

Approved:

Deyu Li, Ph.D.

Haoxiang Luo, Ph.D.

Leon M. Bellan, Ph.D.

Yaqiong Xu, Ph.D.

Donna J. Webb, Ph.D.

ACKNOWLEDGEMENTS

This work is based on the studies of cell mechanical and electrical activities as well as organism behaviors with a series of technological innovations. I am grateful for my advisor, committee members, colleagues, friends, and family in inspiring me to start, preserve and finish this journey.

First, I am thankful and fortunate to have Dr. Deyu Li as my advisor. He brought a depth of knowledge into this work and enlightened me in the course of pursuing my PhD degree. As a Chinese proverb says, “Give a man a fish and you feed him for a day. Teach a man to fish and you feed him for a lifetime.” Dr. Li encouraged new ideas and provided thoughtful feedback; more importantly, he trained me into an independent thinker and researcher with a dialectical mind and a scientific skepticism in searching after truth.

Second, I would like to express my appreciation to Dr. Yaqiong Xu and Dr. Donna J. Webb for constantly providing insights and guidance during the five years of research collaboration.

Also, I express my deep gratitude to the rest of my committee members, Dr. Haoxiang Luo and Dr. Leon M. Bellan. Thanks for the time, support, and constructive advices during my PhD graduate study.

Next, I would like to thank my dear colleagues and friends, Dr. Yang Yang, Kyle Otte, Dr. Bryson Brewer, Dr. Kirsten Heikkinen Dodson, Qian Zhang, Lin Yang, Yin Zhang, Long Wang, Dr. Léolène Jean Carrington, Begum Erdogan, Dr. Mingjian Shi, Dr. Mingfang Ao, and Rui Wang. Without their support and the spice they added to my life, this path would not be so fruitful and delightful.

Finally, I want to thank my parents, Jinbo Yang and Xiuqing Wang, as well as my fiancé Dr. Yaxi Shao. At the moments when I was trapped by obstacles, they have always been with me and let me realize that “Every cloud has a silver lining.” I am tremendously thankful to have them in my life.

TABLE OF CONTENTS

Page

LIST OF TABLES

Page

LIST OF FIGURES

Page

CHAPTER I

INTRODUCTION

1.1 Background

It is amazingly puzzling and intriguing how cells detect and respond to mechanical, chemical, and electrical stimuli, and make vital cellular decisions accordingly. Generations of researchers have put unremitting efforts into developing approaches and tools to unravel the mysteries of cellular activities at both molecular and behavioral levels. However, there are still many issues remaining to be addressed.

In this dissertation, cell mechanotransduction and electrical activity as well as organismal behaviors were investigated through a series of novel microfluidic platforms. Mechanotransduction is a ubiquitous property that allows cells to convert "mechanical inputs" to "biological outputs"[1]. Additionally, defects in mechanotransduction can lead to pathogenesis of various human diseases[2,3]. Therefore, understanding the mechanisms underlying mechanotransduction is of great importance for biological and pathological purposes. Innovative techniques such as optical, magnetic, and mechanical tools have been developed and employed to explore cell mechanotransduction *in vitro*. Importantly, microfluidics, with the merits of low-cost, simple flow pattern, precise control, and compatibility with high-resolution imaging, set foot in biological research and gained wide popularity since late 1980s[4]. With the advent of microfluidics, precisely controlled forces can be applied to an isolated single cell, a population of cells, co-cultured cells of different types and even organisms.

In addition to cell mechanotransduction studies, another compelling issue in biology is the electrical activity detection of neural systems with high spatiotemporal resolutions. Electrical activity occurring in the central nervous system (CNS) is fundamental to our brain functions and has drawn extensive attention for almost 200 years[5]. In the CNS, neuron-to-neuron communication relies on transient and local membrane potential change[6]. To interpret the physiological information encoded in the action potentials, instruments with millisecond temporal resolution, sub-micron spatial resolution and millivolt charge sensitivity are required[6]. So far, technological innovations such as patch-clamping, optical imaging, and microelectrode arrays (MEAs) have provided unprecedented opportunities to understand neuronal electrical activity; however, it is still difficult for these technologies to obtain information over a large neural network with high spatiotemporal resolutions.

This introductory chapter provides a brief description of relevant background on mechanotransduction and electrical signal transmission in neural systems, and also describes the existing tools harnessed in previous studies. In addition, the history, principle, and advantages of microfluidics, the fundamental technique in this work, are briefly introduced.

1.2 Mechanotransduction

1.2.1 What is Mechanotransduction?

Mechanotransduction denotes a cellular property that translates mechanical stimuli from its immediate surroundings into biological signaling cascades. In return, these signaling pathways allow cells to adapt to the new local microenvironment at subcellular, cellular, or extracellular level, such as activation of ion channels, reorganization of actin filaments, myosin, and cytoskeleton, alteration in cell morphology, proliferation, differentiation, contractility,

motility, orientation, as well as the chemical composition and structural organization of the extra cellular matrix (ECM)[7,8]. In this process, ECM, transmembrane receptors, and intracellular structures are three key players[8]. Tansmembrane receptors (e.g. integrins) transmit mechanical load from the "outside" (ECM) to the "inside" (intracellular structures such as actin filaments, non-muscle myosin, and related proteins) of cells. The intracellular structures further pass the mechanical signals throughout the whole cell.

1.2.2 Physiological and Pathological Examples

Mechanotransduction is critical for cell health and tissue homeostasis. It occurs in most cells and organs, from the simplest to the most complex ones[7]. For example, sensory cells such as hair cells in inner ears can transduce the mechanical stimuli of sound, gravity, and head movement into biochemical/electrophysiological signals by opening cation channels[9]. Mechanotransduction occurs in bone formation and restoration, too. The shape, size, and density of bones are closely related to both dynamic and chronic mechanical loading[10]. Also, muscles constantly adjust the force generation capacity and flexibility in response to changes in external forces through downstream signaling cascades[11]. Moreover, the distribution and size of blood vessels are regulated by pressure, shear stress, and circumferential stretch exerted on the vessel walls, thereby adjusting blood flow to meet the demands under different conditions[12]. In addition to these stress-loaded cells and tissues, researchers have also been studying mechanotransduction in a broader context, such as embryogenesis[13].

Extensive evidence has shown that mechanotransduction plays a vital role in the development and maintenance of cells and tissues. From another perspective, defects in mechanotransduction can lead to pathogenesis of human diseases, such as muscular dystrophies,

cardiomyopathy, cancer progression and metastasis[14], CNS pathophysiology[15], and loss of hearing[16]. Especially, the function of mechanotransduction in cancer, one of the most fatal diseases, has drawn significant attention in the past two decades. The abnormal changes in mechanical properties as well as structural arrangement in the ECM and the force-dependent signaling adaptions such as integrin expression, activity, and adhesions[7,17] have been proven to facilitate tumorgenesis and transition of tumor cells from a relatively quiescent to a malignant phenotype. Another pathological example is scar formation and fibrosis. Scar formation is promoted in highly mechanical stressed wounds and suppressed in less stressed conditions[18]. This provides insights on the role of mechanical forces in the regulation of wound healing process. Note that during this process, fibroblasts are critical contributors in the production and repair of fibrotic matrix and are closely involved in tissue regeneration[19]. Meanwhile, upon mechanical stimulation, signaling expression by fibroblasts on collagen, alpha-smooth muscle actin (α-SMA), a marker of human hypertrophic scarring and myofibroblasts, and pro-fibrotic chemokines are significantly enhanced, suggesting that fibroblasts are key players in wound fibrosis[20]. The mechanosensitivity and the important biological role of fibroblasts make them an excellent subject for mechanotransduction study.

1.2.3 Technologies to Investigate Cell Mechanotransduction

Cells *in vivo* are exposed to various types of mechanical stimuli, such as stretching, compression, shear force, and rigidity change of the physical environment. For example, both articular cartilage and cardiac fibroblasts are subjected to tensile and compressive loads[21]. Endothelial cells that line the inner surface of blood vessels experience hemodynamic and shear forces produced by blood flow and pressure[22]. Tumor growth in a limited physical environment will elevate interstitial fluid pressure and exert compressive force to tumor body as well as the

surrounding normal cells and tissue[23]. Furthermore, tumors can also change the rigidity of the local environment because they are believed to be stiffer than the normal tissue[3]. To date, extensive studies have been conducted, providing a wealth of understandings on regulation of cell-matrix interactions, cell functions, and tissue hemostasis in response to mechanical stretching, compression, shear force, and stiffening of the physical environment.

I. Stretching

Various techniques based on optical, magnetic, and mechanical approaches have been employed to apply stretching force to cells precisely. Optical tweezers (OT) have been used to trap and stretch single cells to characterize cell mechanical properties following two common schemes. One is to stretch a cell through two attached microbeads bonded to the cell via ligands or antibodies. Typically one bead is fixed to a substrate such as a glass slide, while the other one shifts position to apply stretching force to the cell[24]. The other way uses two counter-propagating divergent laser beams to immobilize and stretch a single cell[25,26]; this is because the total force acting on the cell is zero but the surface forces are additive, leading to a stretching of the cell along with the axis of the beam. The magnitude of the stretching force is determined by the mechanical and morphological properties of specific cells, reflective index, and laser power[24]. This technique has been applied in biomechanical characterization of cells such as measuring cell stiffness[27]; and it has also been used to investigate cell behaviors such as the relationship between the deformability and progression of cancer cells[28].

In addition to OT, magnetic tweezers (MT) is also a widely-used tool to manipulate and stretch single cells and molecules. In this approach, magnetic beads attached to the cell surface via ligands or antibodies are controlled by a magnetic field to apply mechanical stretching force[24,29]. More complex magnetic system, such as the integrated magnetic microtissue tester

(MMT)[30], allows researchers to investigate cell behavior and mechanical characteristics under stretching when co-cultured with other cells in a three-dimensional (3D) matrix. More specifically, in MMT, cells in a hydrogel construct are suspended over two micro-cantilevers. One cantilever works as an anchor while the other one with a nickel sphere attached to the tip works as a magnetic pillar. Under an inhomogeneous magnetic field, the displacement of pillar tip can apply tensile force to the cells in a 3D construct[30].

Both OT and MT find wide use in single-cell studies given their high specificity and spatial resolution. However, they both require complex optical or magnetic instruments as well as intensive labor. Moreover, low yield makes OT or MT difficult to conduct collective cellular behavior studies. Customer-made mechanical stretching devices spanning from micro to macro scales, as an interesting alternative, are able to examine single cells as well as collective behavior of co-cultured cell systems upon stretching[31,32]. These platforms, together with high resolution microscopy, offer many opportunities to study mechanotransduction at different scales spanning protein, single cell, cell population, and even organ with a significantly improved throughput compared to OT and MT. Generally, cells are subject to tensile force via a stretchable, elastic membrane, such as silicone. The mechanical stretching can be imparted through different means (Fig. 1.1), including horizontally dislocating movable anchors[31–35], protruding an indenter upward[33,36–38], or vacuum suction[39]. Essentially, deformation of the elastic membrane stretches cells attached to the surface. Depending on the design, these devices can provide uniaxial, biaxial, and equiaxial stretching.

For example, microfluidic devices such as Huh et al.'s "Lung on a Chip" and Kim et al.'s "Gut on a Chip" allow for uniaxial stretch application to cells attached to a suspended membrane in the cell chamber by applying vacuum pressure to two adjacent chambers[31,35]. Building upon

these designs, a configuration with four vacuum chambers located at each side of the cell chamber can provide a full and independent control of a biaxial strain field[40]. In this dissertation, inspired by Huh et al.'s design, we modified the fabrication process to construct a more user-friendly stretching platform with better control of applied strain to study the mechanotransduction response of fibroblasts.

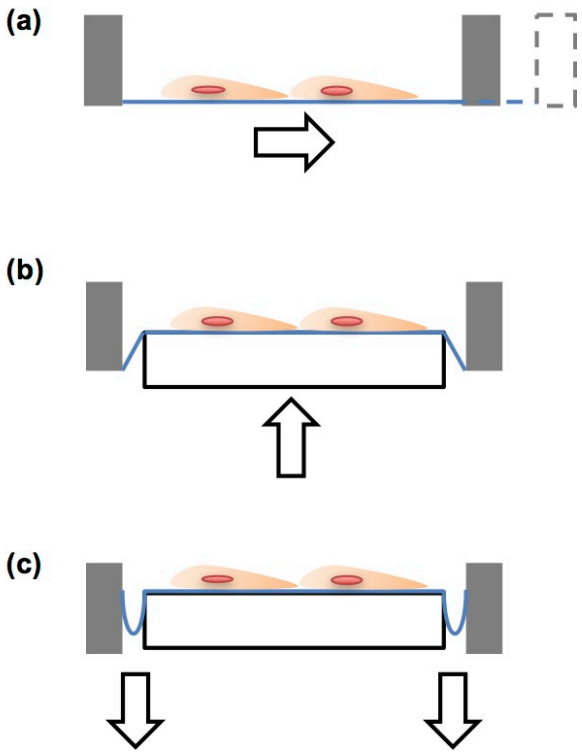

Figure 1.1 Schematics depicting three schemes of mechanical stretchers. Tensile stress is applied by (a) horizontally dislocating movable anchors, (b) protruding an indenter upward, (c) vacuum suction.

These stretching platforms have proven to be effective tools to study cellular activities under precisely-controlled mechanical stimuli. Especially, researchers gradually unfolded the myth of cell reorientation upon stretching with the accumulation of scientific evidences. A large number of reports have demonstrated that cells subjected to a cyclic uniaxial stretch tend to reorient themselves away from or perpendicular to the stretching direction[41–46]. This adaptation

of orientation has been further quantitatively examined and reported to be force duration dependent because the reorientation was not observed under insufficient period (15 min per day on three consecutive days) of the stimulation[47]. In addition to duration, the magnitude of strain has been proven as an influential factor and its effect varies among different types of cells. A tolerance of 2% tensile strain has been reported for arterial smooth muscle cells[48], while 4.2% for fibroblasts, 6.4% for osteoblasts[41], 3.5% for melanocytes[49], and 4.4% for bone marrow mesenchymal stem cells[50], have been disclosed. Below these thresholds, no reorientation was detected for these cell types. Another contribution of these platforms lies in the pursuit of understanding on how cell proliferation and signaling change upon stretching. It has been revealed that stretching promotes cell proliferation in a strain-dependent manner. For example, the proliferation of human osteoblasts is significantly increased under a cyclic tensile strain of 1%, while 2.4%, 5.3%, and 8.8% have minor influence[47]. Also, fibroblast proliferation shows a slight increase at 4% stretching and a more significant increase at 8%[51]. Besides cell orientation and proliferation, mRNA expression and protein secretion such as collagen types I and III, tenascin-C[51–53], integrin $\alpha 5$ and $\beta 1$[54], vascular endothelial growth factor (VEGF)[55], and transforming growth factor $\beta 1$ (TGF-$\beta 1$)[51] are upregulated in response to streching.

II. Compression

In addition to mechanical stretching, compression is also a common type of mechanical stimuli *in vivo*. Studies on the impact of compression on gene expression[56–61], cell morphology[58,62,63], alignment[58,64–66], differentiation[60,61,67–70], and proliferation/apoptosis[59,71] exhibit fruitful progress with the assistance of innovative approaches.

A typical compression bioreactor consists of a piston controlled by a weight or a motor/drive assembly that applies force on cells, a micro-porous filter that allows media to

penetrate through, and a chamber that contains the media and cells. This apparatus has been implemented to compress monolayers of metastatic murine mammary carcinoma cells and concluded that compressive force suppresses cancer cell proliferation and induces apoptosis[71]. Another study on human osteoblast-like MG-63 cells confirmed this conclusion, and quantitatively related this apoptotic response with the applied force magnitude and duration[72]. This setup has also been employed to study the influence of mechanical compression on cell morphology and orientation. For example, glioblastoma and breast cancer cells have been proven to elongate and reorient themselves perpendicular to the load direction upon a 50% compressive strain. Similar behavior has been observed in fibroblasts and smooth muscle cells[66]. Additionally, gene expressions involved in weakening cell-cell contact, increasing ECM degradation, and promoting invasion are upregulated upon compression exerted using this apparatus[69]. This apparatus also contributes to studies on cell migration and differentiation. For example, it is reported that compressive force promotes cancer cell invasion via stimulating the formation of leader cells and increasing cell–substrate adhesion[23], upregulates osteoclastogenesis in periodontal ligament cells[68], and facilitates chondrogenesis and the related proteins expression (such as Sox-9, aggrecan, type II collagen and TGF-β receptors) in bone marrow stromal cells and human embryoid body-derived cells[60,61,73,74]. Furthermore, altered expression levels of integrin β1 upon compression was also revealed[58].

Another bioreactor allowing for horizontal compressive force application to cell/collagen constructs has been reported recently. This bioreactor is composed of a two-compartment petri dish with a partition wall in the middle and two platens set at each side. The platens were affixed to a pair of micromanipulators, which could move toward and away from the partition wall, thereby providing programed cyclic compression on the disc-shaped cell/collagen constructs[64]. It

is compatible with optical imaging through an inverted microscope; therefore, the loading process and cell response can be recorded dynamically. This reactor has been implemented to examine cell reorientation and protein expression for human mesenchymal stem cells (hMSCs). It has been shown that hMSCs tend to orientate themselves along the direction of the compressive loading, and the reorientation depends on collagen-concentration of the construct[64].

One more useful technique is a four-point bending setup in which cells were cultured on a type I collagen-coated plate suspended on two outer anchors. The plate was bent downward by pushing down two inner points resulting in a compressive force application to the cells adhering to the plate[75]. One report utilized this setup to examine changes in the differentiation of adipose-derived stem cells (ASCs) in response to compression and demonstrated that compressive force inhibited adipogenesis of ASCs[76].

A microfluidic device with a pneumatic control recently emerged to study the effect of compression on cells[63]. This device consists of one pressure chamber on the top and one cell culture chamber at the bottom. The deformation of the ceiling of the cell culture chamber induced by the air-pressurized top chamber leads to a compressive force exertion on cells. To precisely control the magnitude of the force and to avoid cells being smashed, micropillars were deposited on the bottom substrate. Under compression, Si et al. found that the morphology of Escherichia coli cells changed from rod-like to a flat pancake-like shape. More interestingly, the change is reversible for these bacteria cells: when compression was removed, the shape returned back to rod-like after several generations[63].

III. Shear Force

Vascular endothelial cells (EC) are constantly exposed to shear forces induced by blood flow. A steady laminar blood flow is essential to vessel homeostasis[77,78]. It is well acknowledged that shear stress can be sensed and transduced to biological signaling such as GTPases, mitogen-activated protein kinases (MAPKs), protein kinase C, and focal adhesion kinase (FAK), platelet-derived growth factor (PDGF), TGF-β, the potent vasodilators NO, and other ECM regulating factors[79,80]. In addition, EC proliferation[81], apoptosis, migration[82], membrane permeability, morphology and alignment[81], reorganization of stress fibers (SFs), and mechanical properties[81] are all affected by shear stress in a magnitude, duration, and flow pattern dependent manner[83,84]. Accordingly, disrupted shear flow can cause post-surgical neointimal hyperplasia, in-stent restenosis, vein bypass graft failure, and transplant vasculopathy, as well as aortic valve calcification[78]. A series of flow-exposing apparatuses designed to tackle shear-force related puzzles gained broad recognition and utilization. These platforms typically consist of a substrate for the growth of a monolayer of ECs and a compartment allowing for application of shear force to cells[79,85–87]. This scheme has been integrated with microfluidic techniques, precisely providing different flow patterns in the EC-cultured channel. For example, one work reported a microfluidic chip with delicately designed microscale barriers in the path of the flow to provide three modes of shear stresses (uniform, linear gradient, and non-uniform) at different locations[88]. Another work varied shear strains in the microchannel through introducing discrete steps of different heights on the substrate[89]. It is noted that ECs are not the only cell type exposed to shear force; meanwhile, vascular smooth muscle cells (SMC) that rest in a neighboring layer of ECs also indirectly experience shear force and present adaptive behaviors. Techniques that allow for examination of ECs in response to shear force in the presence of SMCs are necessary. By

modifying the original flow-exposing apparatus and co-culturing ECs and SMCs in 4 modes, (1) culture ECs on SMCs on one side of the substrate, (2) culture ECs and SMCs on opposite sides of a porous membrane, (3) culture ECs in a shared media with SMCs without direct contact with SMCs, and (4) culture ECs on a SMC/collagen matrix, researchers provided a new perspective on EC-SMC interaction upon shear flow[85]. In brief, this platform has been proven to be an effective tool to investigate the effect of shear force on ECs.

IV. Rigidity

Living cells can sense changes in the stiffness of the substrate or ECM to which cells adhere through focal adhesion proteins and hence tailor cellular activities to the new rigidity of the physical environment. A stiffness-tunable polymer/gel substrate is beneficial to the investigation on such cellular behaviors in response to various rigidities. The variability is achieved by changing the extent of polymer cross-linking. Typical polymers such as polyacrylamide (PA)[89–92] and polyvinyl chloride (PVC)[93] have been broadly adopted. For example, a mixture of PVC and a plasticizer in different ratios can modulate the stiffness of the material from 20 to 60 kPa[93]. In another work, a gradient of rigidity generated by placing two droplets of PA with bis-acrylamide components in different concentrations adjacent to each other on a coverslip has been reported to affect cell migration[92]. In addition, poly(dimethylsiloxane) (PDMS) substrates with varying ratios of the base to the curing agent have also been used to provide different substrate stiffness[94].

An elastomeric PDMS micropost array has also been demonstrated for studying the effect of substrate stiffness on cells. Different substrate rigidities are achieved by varying the post heights. This tool has been employed to examine the influence of rigidity on cell morphology, focal adhesions, cell traction force, cell differentiation, and migration[95–97].

1.3 Neuronal Electric Activity Sensing

In addition to cell mechanotransduction, neuron electric activity is also a focus of this work. Neurons in the central nervous system (CNS), the most complex and dynamic network that nature has developed, receive information from peripheral neurons and process the information, all through electrical signal transmission and integration[98]. A typical neuron consists of a cell body (soma), an axon, and many dendrites. An axon is a neuronal extension transmitting chemical and electrical signaling to downstream neurons. Dendrites are highly branched-out structures that receive incoming information via small membranous protrusions (dendritic spines) and transmit to the cell body[99]. Neuron-neuron communication occurs at synapses, highly specific connections between pre-synaptic axonal terminals and post-synaptic dendritic spines, propagating information encoded as a pattern of action potentials (spikes)[100,101]. Synapses are plastic and able to change their strength in response to their electrical activities, which is referred to as synaptic plasticity[102]. Synaptic plasticity has been increasingly recognized as a relevant feature of learning and memory, and abnormalities of plasticity are believed to be involved in many CNS disorders[101]. Given that neurons are the fundamental building blocks of CNS, understanding neurons and their interactions, at cellular and molecular levels, is the cornerstone of neurobiology and of great importance for brain physiological and pathophysiological studies.

Considering the critical function of neurons and the severity of CNS disorders, extensive attention has been drawn to neuronal studies for more than 200 years[103]. Immense efforts have been invested to design and develop tools capable of detecting synaptic electrical activities. With the assistance of modern tools, such as patch-clamping, optical imaging, and microelectrode arrays (MEAs), researchers have learned more about the nervous system in the last fifty years than ever before[104].

Electrophysiology recording offers great opportunities to study single or multiple ion channels of neurons since the discovery of the patch-clamping technique by Bert Sakmann and Erwin Neher in 1976[105]. This technique allows for accurate measurement of single ion channel activity at high sensitivity and temporal resolution, and won the 1991 Nobel Prize in Physiology or Medicine[106]. Patch-clamping method employs a pipette with a tiny opening to make tight contact with a small patch of cell membrane. By applying a gentle suction, it forms a high-resistance (giga-ohm) seal at the gap between the pipette and the membrane. This way, ions that flow through the open ion channel enter the pipette and then are detected by an electronic amplifier. Patch-clamping technique enables researchers to listen to the "language" of neurons directly without the need of a "translator" to transform neuronal electrical signals to other signals; therefore, the main strengths are excellent time resolution, sensitivity, and signal-to-noise ratio[103]. However, it requires delicate and intensive physical manipulation of fragile neurons and a complex experiment procedure, hence yielding a very low throughput[106]. Although planar patch-clamping and automated patch-clamping emerged and have the potential of increasing throughput by measuring multiple neurons simultaneously[107,108], accurately guiding isolated cells to the sensing region and forming gigaseals to achieve low noise measurement are still technically challenging[109]. It is even more difficult to apply automated patch-clamping technique to patch on small structures such as axons, dendrites, and soma of neurons[109].

On the contrary, optical imaging techniques, such as fluorescent voltage-sensitive dyes (VSDs) or calcium indicators, do not require physical contact and allow for neuronal activity measurement with high spatial precision over a wide range of scales[103], which serves as a powerful alternative approach for patch-clamping. However, VSDs label both internal and plasma membranes; the former does not contribute to the signal but to the fluorescent intensity in

the background, resulting in a low signal-to-noise ratio. In addition, phototoxicity and photobleaching limit the application of VSDs[6,103,110]. Calcium probes have an advantage over VSDs on signal-to-noise ratio because it is genetically targeted to specific molecules. Despite this advantage, the inherent weakness of this methodology is signal translation time. The slow time course of intracellular calcium signals triggered by action potentials[111] largely limits the temporal resolution of this technique.

Another alternative approach is MEAs that employs microelectrodes to simultaneously record a neuronal network at a time scale of milliseconds[107]. The biggest challenge of this approach lies in the limitation on the size and number of electrodes, preventing electric measurement at subcellular level. Recently, the complementary metal-oxide-semiconductor (CMOS) based high-density MEAs, taking advantages of active switches and integrated circuits as well as more advanced lithographic techniques, made a great process in resolving spatial signals down to a few microns and mapping neuronal electric activity at subcellular level[112,113].

1.4 Microfluidics

Microfluidics has been extensively adopted in biological and biomedical studies owing to many advantages over conventional approaches. Compared to traditional tubes and dishes, much less amount of sample is consumed with microfluidic chips in a bioassay or cell culture process; and therefore, it is of low-consumption. In addition, because of the small size, flow in microchannels is laminar, which is simpler, more controllable and predictable. Furthermore, it is feasible to realize precise modulation and stimulation of single or populations of cells using microfluidics. Importantly, high-throughput parallel assays can be achieved through multiple microchannels on one chip[114].

Microfluidic devices are fabricated through soft lithography developed by George Whitesides et al.[114,115]. Briefly, soft lithography uses a replica-molding scheme to create a patterned elastomer, PDMS, from a master mold pre-fabricated through photolithography. PDMS has unique and advantageous material attributes over other typical micromachining material such as silicon and metal. It is transparent, and hence compatible with visual observation and optical imaging. Its biocompatibility allows for long-time cell culture and bioassays. The permeability to gases provides cells with the access to oxygen, which is critical to cell health. The wettability is adjustable to meet multiple purposes: its natural hydrophobic property enables it to seal reversibly with most dry, smooth surfaces; while the surface can be altered to be hydrophilic with oxygen-plasma treatment and irreversibly bonded to glass. This hydrophilicity will last if the PDMS is kept in contact with water; however, if it is exposed to air, the hydrophobic groups will recover on the surface to reduce the surface free energy[116]. PDMS is elastic so it can be easily released from the replica and kept intact. Also, this elasticity makes pressure-driven valves possible[117]. These valves rely on the deformation of PDMS under pressure, providing inexpensive and reliable flow control. More interestingly, PDMS is a mixture of polymer and a curing agent typically in a ratio of 10:1; however, the ratio can be tuned to yield different stiffness. This is an effective and easy approach for studying the effect of rigidity on cellular behaviors[94,95]. Although PDMS offers these benefits, it has some drawbacks. First, it absorbs small hydrophobic molecules and leaches uncured oligomers[118]. To address this issue, numerous surface treatments such as layer-by-layer deposition of polyanions and polycations, sol-gel coating[119], salinization, and deliberate protein absorption[120] have been reported. Secondly, the fact that PDMS is gas-permeable can be harmful for some applications. PDMS allows water

vapor to permeate through, causing the loss of stored media in microchannels[121]. Despite these disadvantages, PDMS is still the most widely adopted material for microfluidics.

1.5 Dissertation Overview

This dissertation describes the design and application of a class of microfluidic platforms to explore cell mechanical and electrical activities as well as organism behaviors.

The dissertation consists of the following sections:

Chapter I provides a review on mechanotransduction with respect to the definition, physiological and pathological examples as well as innovative approaches, followed by a comparison of existing sensing tools for neuron electrical activity measurement and a brief introduction on microfluidics history and fabrication.

Chapter II presents a microfluidic stretching platform and reveals the mechanotransductive behaviors of fibroblasts in response to mechanical stretching and force relaxation. It demonstrates that mechanical stimuli are deterministic factors in activating normal fibroblasts (NAFs) and deactivating cancer-associated fibroblasts (CAFs). Also, it describes a microfluidic stretcher design integrated with graphene transistors for detecting the electrical activity of neurons subjected to mechanical stretching.

Chapter III shows that NAFs are aligned to specific angles while CAFs maintain a random distribution in response to compression in a 3D matrix. A mathematical model based on the minimum energy principle is laid out to explain the observation, disclosing the important role of stress fibers and inherent cell contractility in cell reorientation.

Chapter IV showcases a novel graphene transistor based microfluidic sensing platform capable of measuring single depolarization event of neurons upon chemical stimulation at single synaptic and dendritic level. This platform possesses advantages in terms of high spatiotemporal resolution, charge sensitivity, signal-to-noise ratio, ease of operation, compatibility with high-resolution confocal microscopy, and sustainability of long-term cell culture over conventional tools.

Chapter V exhibits a microfluidic diode design capable of simultaneously sorting worms by size at a high throughput and allowing for worm collection or immobilization for further investigation. This novel design leads to a unidirectional worm transport and hence remarkably enhances the sorting efficiency and accuracy. More importantly, this feature allows for worm sorting at relatively low flow rates; and therefore, the device is of practical use in sorting worms with the presence of egg clusters and debris.

Chapter VI summarizes the progress described in this work and discusses the future outlook of employing microfluidic platforms to study biomechanical and electrical activities.

CHAPTER II

INVESTIGATION OF THE EFFECTS OF MECHANICAL STRETCHING AND RELAXATION ON CELLS USING A MICROFLUIDIC STRETCHER

2.1 Motivation

As discussed in Chapter I, most cells are able to detect and respond to mechanical forces in the surrounding physical environment. In this chapter, we examined the effects of mechanical stretching and force relaxation on an important cell type: fibroblasts. Fibroblasts are responsible for producing many types of ECM constituents such as type I, III, and V collagen. Also, they are critical mediators of scar formation and tissue fibrosis in wound healing process. In healing wounds or fibrotic tissues, fibroblasts that synthesize higher levels of ECM constituents and proliferate more than normal fibroblasts (NAFs) are referred to as "activated" fibroblasts[122]. A similar activated phenotype known as cancer-associated fibroblasts (CAFs) is found in tumors and believed to be a key facilitator of tumor growth, progression[122], and metastasis[32]. Previous studies have been done to characterize CAF gene expression, signaling pathways, and tumor promoting functions, but a fundamental question, that is, how CAFs are produced (CAF genesis), remains elusive. To untangle this puzzle, researchers conducted extensive studies of multiple biochemical factors while biophysical factors have received relatively less attention. However, biophysical effects may play important roles in CAF genesis given the altered mechanical microenvironment in tumor and the vital role of mechanical stress in fibroblast morphology, orientation, proliferation, SF organization, gene expression, and protein synthesis. Therefore, the first goal in this chapter is to explore the contribution of mechanical stretching in NAF activation

using a microfluidic stretcher. We first demonstrated that stretched NAFs lead to aligned fibronectin and directed cancer cell migration along the aligned ECM. These phenotypes of NAFs induced by stretching are different from NAFs without stretching but similar to CAFs, indicating that mechanical stretching plays an essential role in NAF activation and CAF genesis, thus facilitating cancer invasion. Then the following question arises: is it possible to deprive some of the CAF phenotypes by relaxing the inherent mechanical stress of CAFs so that CAFs present more NAF-like phenotypes? We hypothesized that relaxation of the inherent stress of CAFs could "deactivate" CAFs by changing fibronectin deposition and expressing downregulated α-SMA (the phenotypical marker of activated fibroblasts[123]), and thereby suppressing directed migration of cancer cells. In this chapter, a series of experimental studies were conducted using a microfluidic stretcher to answer the above questions. The evidences presented here could potentially provide insights into therapeutic strategies targeting on tumor stroma.

Mechanical forces not only affect the fate of fibroblasts, but also are the principle culprits in traumatic brain injury (TBI). It has been reported that stretching and tearing neuronal and axonal membranes by forces such as a bump, a blow, a jolt to the head, or a penetrating head injury are the main causes of neuronal and synaptic dysfunction in TBI. These mechanical impacts contribute to about 30% of all injury deaths[124]. TBI consists of two phases[125]: in the first phase, the immediate damage is due to the direct mechanical impact, often referred to as the primary injury; in the later phase, second brain injury will occur as a result of an inflammatory response. During the second phase, a series of biochemical activities are triggered to delay tissue damage, such as upregulated release of excitatory neurotransmitters (i.e. glutamate, aspartate), activation of N-methyl-D-aspartate, α-amino-3-hydroxy-5-methyl-4-isoxazolpropionate, and

voltage-dependent Ca^{2+}- and Na^{+}-channels[126]. Meanwhile, extra fluid and nutrients accumulate at the affected area to help heal the damage, which further causes swelling. When this swelling happens in other areas of the body, it is beneficial to injury healing. However, brain swelling occurring in a confined skull can be very dangerous because this process imposes excessive mechanical forces to the injured and uninjured area. In addition, brain swelling, different from the primary injury, is a gradual and slow process, and can last up to 5 days after the initial impact[127]. Despite progress in TBI research, the molecular-level neurobiology knowledge on TBI is still lacking, mainly because of the lack of effective tools for dynamically probing individual synapses and ion channels under mechanical stimuli. Here, we first employed the microfluidic stretcher to stretch neurons in different modes and examined cell viability. Further, a neuron-glia co-culture microfluidic stretcher integrated with graphene probes is proposed in order to investigate synaptic electric activity with a single synapse resolution upon various modes of mechanical stimuli.

2.2 Microfluidic Stretcher Design, Fabrication and Characterization

Inspired by the "Lung-on-a-Chip" microdevice developed by Huh et al.[35], the microfluidic stretcher device is composed of three layers of PDMS and a coverslip substrate. As shown in Fig. 2.1, a 10 μm-thick PDMS membrane is sandwiched by a 1 mm-thick top layer and a 100 μm-thick open channel bottom layer. These three layers are aligned and bonded together to form a central cell-culture chamber and two outer vacuum chambers. By applying vacuum pressure to the side chambers, the walls separating the middle cell culture chamber and the vacuum chambers deform outward, causing horizontal mechanical stretching of the suspended membrane as well as the cells cultured on the membrane in the central chamber. The central cell chamber is 5 mm long and 1 mm wide and connected with 200 μm-wide inlet and outlet

channels, forming an expansion in the middle to reduce flow speed and promote cells to settle down in the chamber.

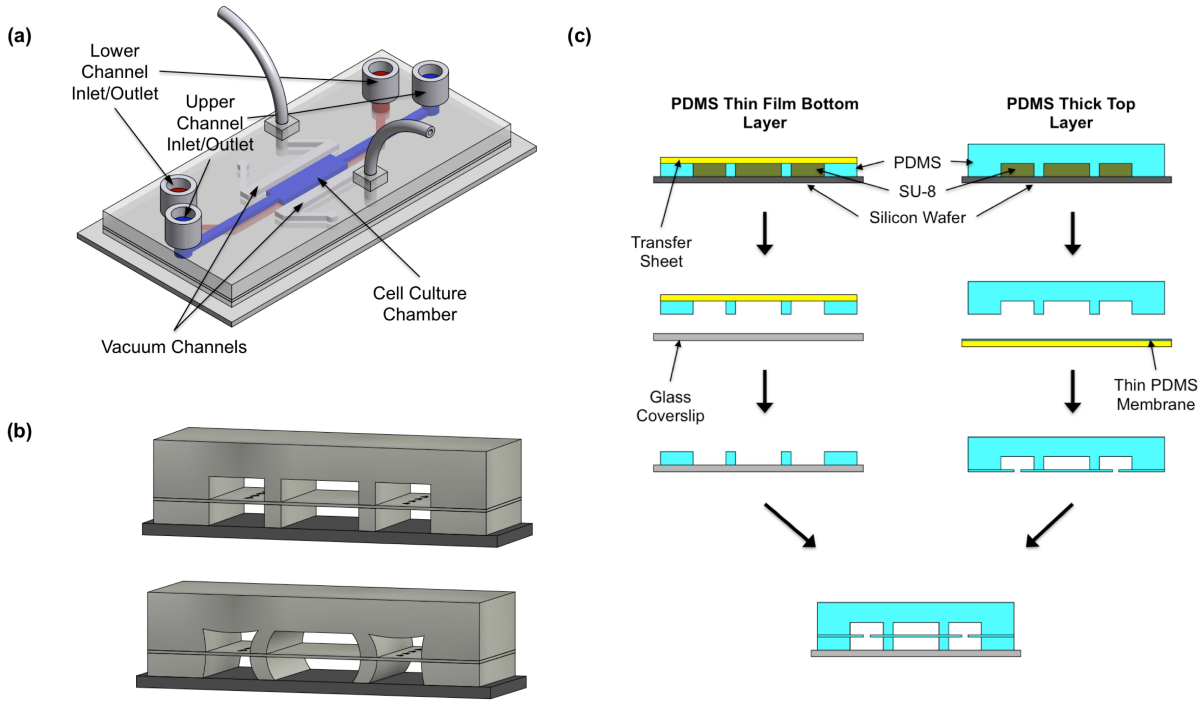

Figure 2.1 Schematic of a microfluidic stretcher device and the fabrication procedure. (a) A three-dimensional schematic (not to scale) of the stretcher platform. (b) A cross-sectional view of the device in the relaxed state (top) and stretched state (bottom) after a vacuum pressure is applied to the outer chambers. (c) Fabrication of the device involves constructing a bottom open-channel layer, a thick top layer, and a thin membrane. These components are assembled and bonded on a glass coverslip.

Based on Huh et al.'s design, we made several modifications to the device fabrication. First, in Huh et al.'s work, to connect the lower and upper sections of the vacuum chambers, the membrane was etched away by flowing in a PDMS etchant comprising tetrabutylammonium fluoride and N-methylpyrrolidinone into the two chambers. The etchant is highly flammable and carcinogenic, and difficult to control precisely owing to the rapid etching speed. More importantly, when pumped into vacuum chambers, the etchant inevitably affects the area other

than the membrane such as the sidewalls that divide the cell chamber and the vacuum chambers. Importantly, the thickness of the walls is closely related to the deflection and the resulting strain of the membrane. Given that the etching rate is relatively high, it is difficult to achieve consistent strain from device to device. Instead of etching away the membrane, holes were simply punched on the membrane using a 30"-gauge needle. Doing so, the stretcher in this work provides more accurately-controlled and more consistent mechanical strains in systematic bioassays. Secondly, the thick bottom layer in the Huh et al.'s design was replaced with an open-channel thin layer (100 μm) to allow for high magnification microscopic imaging on subcellular structures.

The three PDMS layers are generated using different protocols. The thick top layer is fabricated using standard soft-lithography techniques via PDMS replica molding (Ellsworth Adhesives, Germantown, WI) as previously described[32,128]. Basically, a pre-polymer PDMS solution was mixed with a curing agent at a ratio of 10:1 and poured over a master mold fabricated through photolithography. After degassing for 1 h and curing in a 70°C oven for 2 h, PDMS was fully polymerized and then cut out and peeled off the mold. Holes were punched through the PDMS piece for the media and air access. The 10 μm-thick membrane, on the other hand, was fabricated by spin-coating liquid PDMS mixture at 4000 RPM for 30 s on a plastic fluoropolymer coated polyester (PE) transfer sheet (Scotchpak™ 1002 Release Liner, 3M™, St. Paul, MN) that was taped to a petri dish lid in advance. The bottom PDMS layer was fabricated following the protocols described by Hsu et al. previously[129]. More specifically, a little amount of PDMS mixture was spread over the mold and covered by a 3" x 3" PE sheet. After degassing for 30 min, a flat and rigid edge was employed to remove the air bubbles trapped between the mold and the sheet. Then 5 pounds of weight was placed on the top of the sheet and the mold to ensure a clean contact. The PE sheet with an open channel PDMS layer can be peeled off the

mold after curing for 5 h.

After this, the three layers of PDMS together with a 100 μm-thick glass coverslip (No. 1, VWR Vista Vision, Suwanee, GA) were assembled. First, the top PDMS layer underwent oxygen plasma treatment and was bonded to the PDMS membrane. The PE sheet was peeled off the top assembly after bonding. Holes were punched on the membrane at the vacuum chambers under microscope using a 30"-gauge needle. Next, the open channel PDMS layer was bonded to a coverslip, after which the PE sheet was removed from the bottom assembly. Finally, the top and bottom parts were aligned and bonded together. Pyrex® cloning cylinders (10 mm × 10 mm) (Fisher Scientific, Pittsburg, PA) served as media reservoirs were glued over the punched holes using liquid PDMS mixture. Tygon tubing (0.20" ID x 0.60" OD) (Cole-Parmer, Vernon Hills, IL) was inserted to the air access holes so that vacuum can be applied through the tubing. The assembled microfluidic device was placed in the oven at 70°C for 1 h to cure the liquid PDMS and then sterilized under UV light for 1 h.

In order to characterize the achieved membrane strain versus the applied vacuum pressure, fluorescein isothiocyanate (FITC) was pumped into the upper central chamber to visualize the membrane deformation through confocal microscopy when excited by a 491 nm laser line. To precisely locate the membrane, a vertical stack of images was taken with 0.2 μm distance between individual planes at both the left and right edges of the central cell chamber using a Plan Fluor 40X objective (NA 1.3) and a Hamamatsu ImagEM EM-CCD camera. These images allowed us to reconstruct a 3D view and find the plane that represents the top of the membrane. The displacement of the outer edge of the membrane was measured using ImageJ software (NIH, http://rsb.info.nih.gov/ij) upon different vacuum pressures. Strain of the membrane was calculated based on the equation $\varepsilon = \Delta L/L$. Here, ΔL is the deformation of the

membrane that equals to the membrane edge displacement and *L* is the width of the membrane, 1000 µm. Multiple vacuum pressure, 0, 25, 50, and 75 kPa were applied. At each pressure, the data shown in Fig 2.2 (c) represents an average of 5 independent experimental measurements.

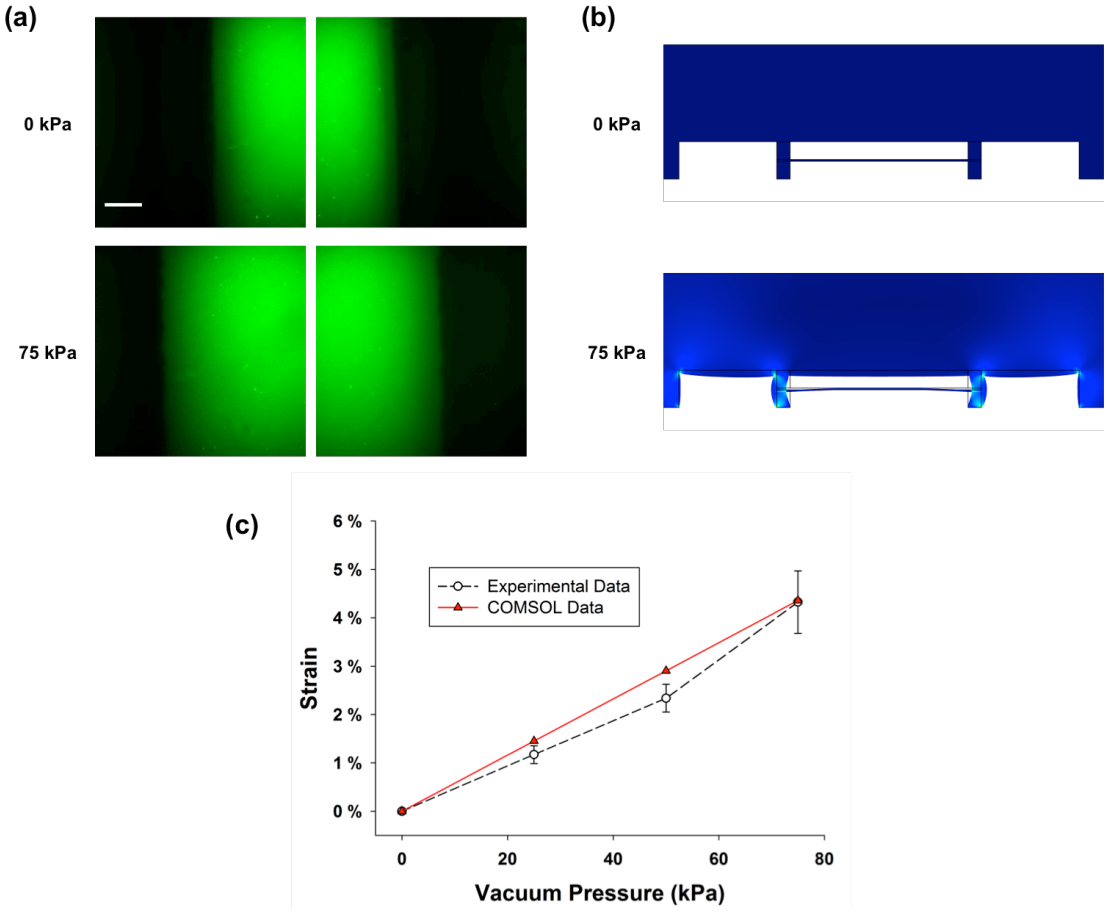

Figure 2.2 Experimental characterization and finite element modeling results of the microfluidic stretcher platform. (a) Characteristic images of the top of the PDMS membrane under different vacuum pressures through confocal microscopy. Scale bar = 20 µm. (b) Visualization of the displacement of the PDMS membrane and sidewalls at different vacuum pressures determined using COMSOL Multiphysics™. (c) Comparison of the strains observed at different vacuum pressures between experimental data and model predictions. The error bars associated with the experimental data represent standard deviation. Five separate devices were tested to generate the experimental data.

In addition to experimental characterization, finite element modeling (FEM) was performed using COMSOL Multiphysics™. More specifically, the Solid Mechanics module was

employed to carry out a stationary and two-dimensional simulation. It is worth noting that the Young's modulus of PDMS changes with crosslinking ratios, dimensions, fabrication processes, and measurement methods. As reported in the literature, the Young's modulus varies from 12 kPa to 6.61 MPa[130–134]. Given the significant variations of thickness at different regions, different Young's moduli were applied accordingly. In the bulk PDMS area, a modulus of 1.8 MPa was chosen[130,132], while for the sidewalls (75 μm thick) and the membrane (10 μm thick), 1.14 MPa and 1.9 MPa were adopted, respectively, as the Young's modulus of PDMS under 200 μm thick is thickness dependent[134]. A density of 965 kg/m^3 and a Poisson's ratio of 0.45 were employed for PDMS. The total amount of mesh elements is 83086. Finer mesh was applied for key domains such as sidewalls and the membrane. By setting the same vacuum pressure as in the experiments, the stress distribution (Fig. 2.2 (b)) and membrane strain (Fig. 2.2 (c)) at each pressure were simulated. The plotted experimental and modeling data in Fig. 2.2 (c) present a good agreement on the linear relationship between the membrane strain and applied pressure, providing a convenient performance characteristic chart of the microfluidic stretcher.

The validated COMSOL™ model also provides design guidelines for the microfluidic stretcher. The modeling results in Fig. 2.3 indicate that the membrane width and sidewall height can significantly affect the deformation and the strain of the membrane. As shown in Fig. 2.3 (a), the deformation of the membrane increases with the membrane width and sidewall height. As for strain, Fig. 2.3 (b) shows that membranes of smallest width yield the highest strain. The results also indicate that changing the sidewall height can effectively alter the strain and when the side wall height is less than 50 μm, the deformation and strain are too small for practical purpose.

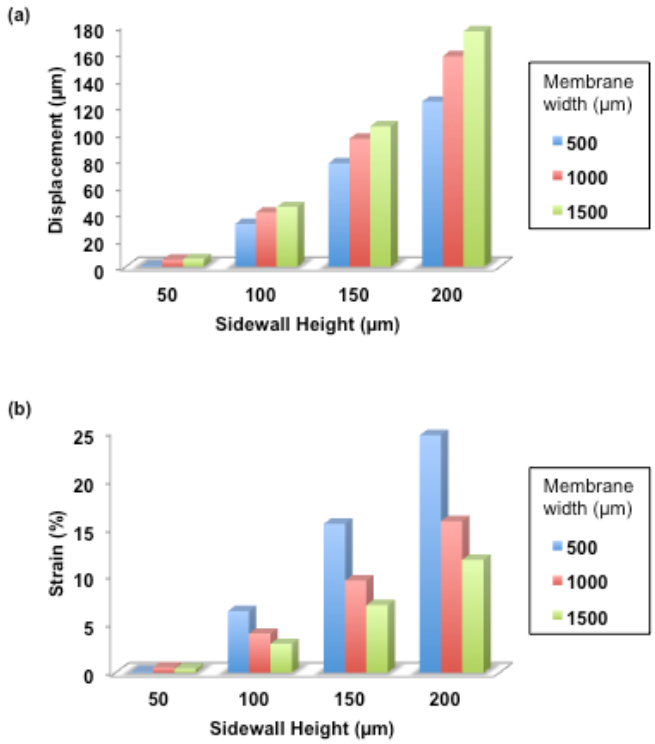

Figure 2.3 Results of COMSOL™ modeling on membrane displacement and strain with respect to membrane widths (500 μm, 1000 μm, and 1500 μm) and sidewall heights (50 μm, 100 μm, 150 μm, and 200 μm) at a vacuum pressure of 75 kPa. (a) Membrane displacement. (b) Membrane strain. The group with a membrane width of 500 μm is represented by a blue column, while 1000 μm and 1500 μm are denoted by red and green columns, respectively.

2.3 Effects of Stretching/Relaxation on NAFs/CAFs

2.3.1 Material and Methods

I. NAF and CAF Cell Isolation and Maintenance

NAFs were isolated from benign prostate hyperplasias and CAFs were isolated from prostate tumors, following the protocols published previously[135]. Fibroblasts were cultured in Roswell Park Memorial Institute medium (RPMI) 1640 with 10% fetal bovine serum (FBS) and penicillin-streptomycin and the cultures were used up to passage 10 for experiments.

II. Cell Loading and Operation of Microfluidic Stretchers

To examine the effect of mechanical stretching and relaxation on NAFs and CAFs, four sets of experiments were arranged: NAF stretching assay, NAF control group, CAF force relaxation assay, and CAF control group, labeled as #1, #2, #3, and #4, as shown in Table 2.1.

Table 2.1 Device serial numbers and purposes

Device Number	Cell Type	Purpose
#1	NAFs	Stretching assay
#2		Control group
#3	CAFs	Force relaxation assay
#4		Control group

To start the assays, the suspended PDMS membrane in the stretcher #3 was stretched to ~4% strain by depressurizing the vacuum chambers, whereas the PDMS membranes in the device #1, #2, and #4 were left unstretched.

After NAFs and CAFs were trypsinized, a 20 µl solution with 10,000 cells was loaded to device #1 ~ #4 through cells loading reservoir (upper channel inlet in Fig. 2.1) to the culture chamber. The flow was slowed down by an addition of 18 µl of cell solution to the upper channel outlet. Fig 2.4 illustrates the operation of devices #1 and #3. Cells were then cultured on the membrane for 2 h for attachment in an incubator at 37°C with 5% CO_2 for all four devices. For the stretching assay with device #1, after NAFs were well attached, both inlets of the vacuum chambers were connected to a vacuum line installed into the incubator in advance. A vacuum

pressure of 67.7 kPa, corresponding to a ~4% membrane strain, was applied for overnight (Fig 2.4 (b)). For the force relaxation assay with device #3, after 2 h of culturing at an initial ~4% strain, the stretched membrane was released (see Fig. 2.4 (d)) and the CAFs were cultured for overnight at an unstressed state.

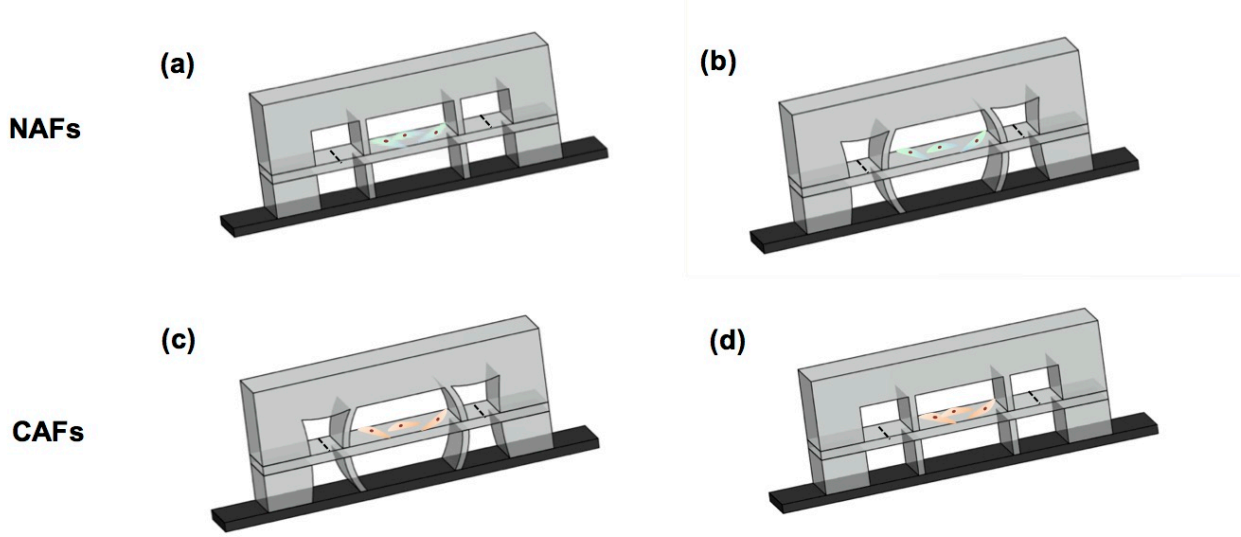

Figure 2.4 Stretching/Relaxation assays on NAFs and CAFs, respectively. (a) NAFs were loaded to device #1 and cultured for 2 h in a cell culture incubator at 37°C for attachment. (b) After 2 h, stretching was applied through a vacuum line. NAFs were continuously cultured in a stretched state overnight. (c) CAFs were loaded to a pre-stretched device and cultured for 2 h in the incubator for attachment. (d) After 2 h, the stress was released. CAFs were continuously cultured in a relaxed state overnight. NAFs are marked in cyan while CAFs are denoted by orange color.

III. Immunofluorescence Staining and Imaging

NAFs and CAFs were fixed in the devices after 12 h stretching and relaxation using 4% paraformaldehyde with 0.12 M sucrose in PBS for 15 min. For fibronectin staining, an antibody against fibronectin (610077, BD Bioscience, San Jose, CA) was used, followed by Alexa Fluor 488 goat anti-mouse secondary antibody (Life Technology, Carlsbad, CA). Primary antibodies were diluted at 1:500 and secondary antibodies at 1:2000 in PBS with 0.2% Triton-X-100. Primary antibodies were incubated for 2 h; secondary antibodies were incubated for 45 min.

Excess and unbound antibody was completely washed out of the channel with PBS. The entire staining process was conducted at room temperature.

For α-SMA staining, cells were permeabilized for 3 min, using 0.2% Triton-X-100 in PBS. Samples were blocked using 20% normal goat serum in PBS. Antibodies were diluted in 5% goat serum in PBS. Antibodies used were as follows: Anti-fibronectin mouse monoclonal antibody (610077, BD Transduction Laboratories, San Jose, CA), anti-αSMA mouse monoclonal antibody (A5228, Sigma, St Louis, MO) and Alexa Fluor 488 goat anti-mouse secondary antibody (Life Technologies, Carlsbad, CA). Primary antibodies were incubated overnight at 4°C and secondary antibodies were incubated for 1 h at room temperature.

Prior to imaging, the devices were disassembled to extract the suspended PDMS membrane for higher magnification imaging. All images were taken using a Quorum WaveFX spinning disk confocal system equipped with a Nikon Eclipse Ti microscope, a Plan Fluor 40X objective (NA 1.3), and a Hamamatsu ImagEM EM-CCD camera. Image acquisition was performed using MetaMorph software (Molecular Devices, Sunnyvale, CA).

IV. Image Quantification

Average fluorescence intensity per cell was calculated by normalizing the background-subtracted integrated fluorescence intensity in individual cells to the unit area using MetaMorph software.

2.3.2 Results

I. Fibronectin Pattern

To examine the effects of mechanical force on the activation of NAFs and deactivation of CAFs, fibronectin as a critical component of ECM was first examined. The organization of the

fibronectin produced by stretched NAFs was noticeably different from that of the control group. The fibronectin produced by NAFs in the control device formed a random network (Fig. 2.5 (a)), while the fibronectin secreted by stretched NAFs formed a more aligned, linear network (Fig. 2.5 (b)). The organization of the fibronectin produced by CAFs shows an opposite trend: CAFs in the control device deposited highly aligned, fiber-like fibronectin (Fig. 2.5 (c)); while in the relaxed condition, CAFs deposited random distributed fibronectin (Fig. 2.5 (d)), similar to NAF control group. Therefore, NAFs and CAFs subject to mechanical stretching and relaxation switched phenotype in terms of deposited fibronectin pattern.

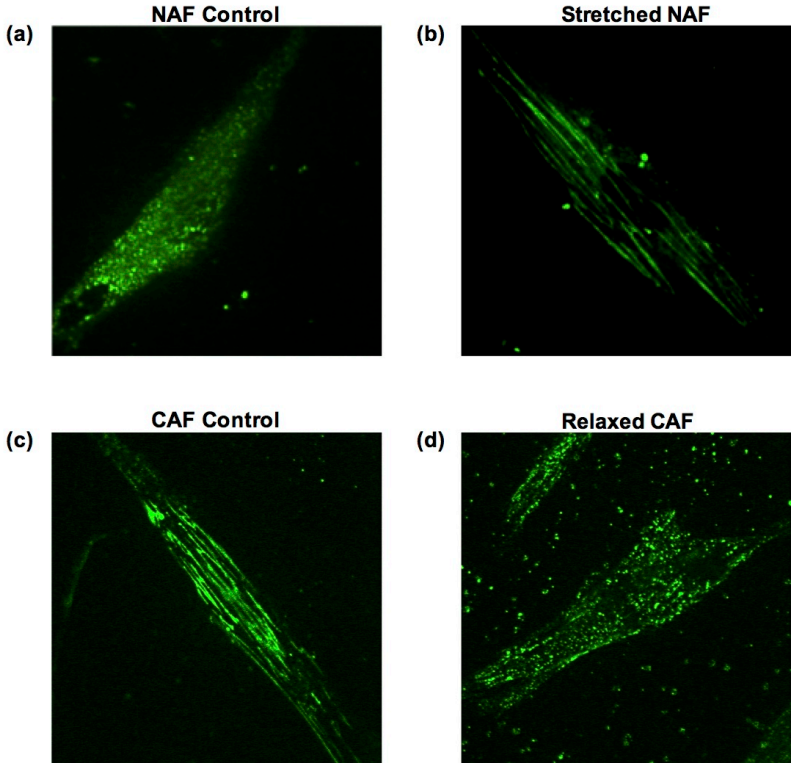

Figure 2.5 NAFs and CAFs expressed fibronectin exhibiting different patterns. (a) Control NAFs expressed random distributed fibronectin. (b) Stretched NAFs expressed well-aligned fibronectin. (c) Control CAFs expressed well-aligned fibronectin. (d) Relaxed CAFs expressed random distributed fibronectin.

II. α-SMA Expression

As we know, α-SMA expression as well as upregulated formation of SFs are well-known markers of fibroblast activation[136]. Interestingly, we observed that the expression of α-SMA and SFs are significantly different in the control and relaxed CAFs. The CAFs in the control condition expressed remarkably higher level of α-SMA and more aligned SFs compared to the relaxed CAFs (Fig. 2.6 (a, b)). To quantitate this difference, fluorescent intensity of α-SMA for around 20 cells was measured and then plotted in Fig. 2.6 (c), showing a threefold downregulation of α-SMA in the relaxed CAFs in contrast to the control CAFs. The lower level α-SMA in SFs represents a decrease of cellular contractile activity[136] that is closely linked to ECM remodeling and stiffening, and the subsequent cancer cell migration[137]. Therefore, the relaxed CAFs show less activated, more NAF-like phenotype upon stretching relaxation.

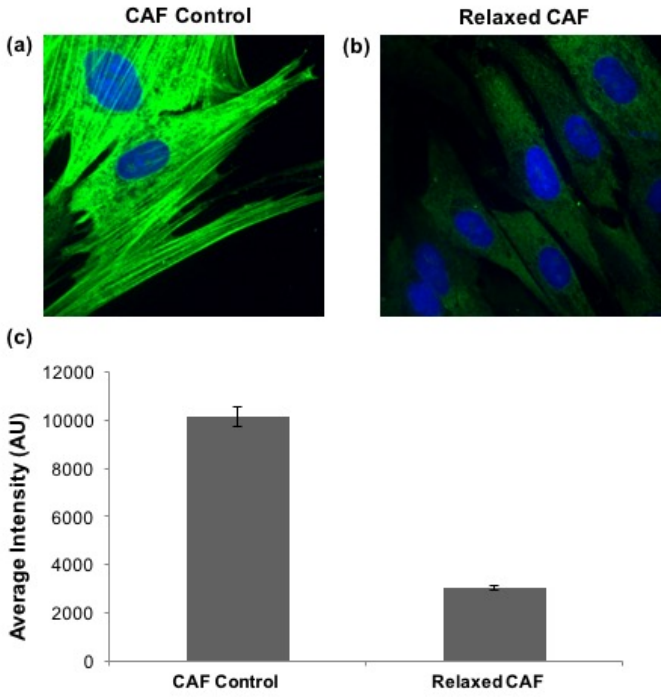

Figure 2.6 Different expression of α-SMA. α-SMA expression in (a) control CAFs and (b) relaxed CAFs. (c) The average fluorescent intensity of α-SMA in the control CAFs is threefold higher than the relaxed CAFs.

III. Cancer Cell Migration

The study of fibronectin alignment indicates that mechanical stretching activates NAFs in a way to induce more CAF-like fibronectin organization and force relaxation deactivates CAFs in the opposite manner. The examination of α-SMA reveals that relaxed CAFs express significantly lower level of the fibroblast activation marker. Taken together, the following questions will be raised: considering that cancer cells tend to migrate along the fibronectin deposited by fibroblasts[138], whether cancer cells co-cultured with stretched NAFs migrate in a manner similar to those co-cultured with control CAFs; moreover, whether cancer cells co-cultured with relaxed CAFs migrate in a manner similar to those co-cultured with control NAFs. To answer the first question, we co-cultured human head and neck cancer cells (SCC61) with stretched and unstretched (control) NAFs as well as control CAFs. We observed a great deal of similarity between cancer cell migration patterns when co-cultured with stretched NAFs (Fig. 2.7 (a), middle panel) and with CAFs (Fig. 2.7 (a), lower panel). On the contrary, cancer cells show random migration when co-cultured with NAFs in the control group (Fig. 2.7 (a), upper panel). The difference between different cancer cell migration patterns can be quantitatively assessed using a directional migration index (directionality), a ratio of the net (D) to total migrated distance (T), which is significantly higher for SCC61 cells co-cultured with stretched NAFs and CAFs as compared to with NAFs in the control group (Fig. 2.7 (b)).

At this moment, the second question, how cancer cells migrate when co-cultured with relaxed CAFs still waits for an answer. However, it is reasonable to hypothesize that cancer cell migration will be in a random manner as it is when co-cultured with NAFs since cancer cells tend to migrate along the fibronectin deposited by fibroblasts[138] and fibronectin deposited by relaxed CAFs and control NAFs shows similar alignment.

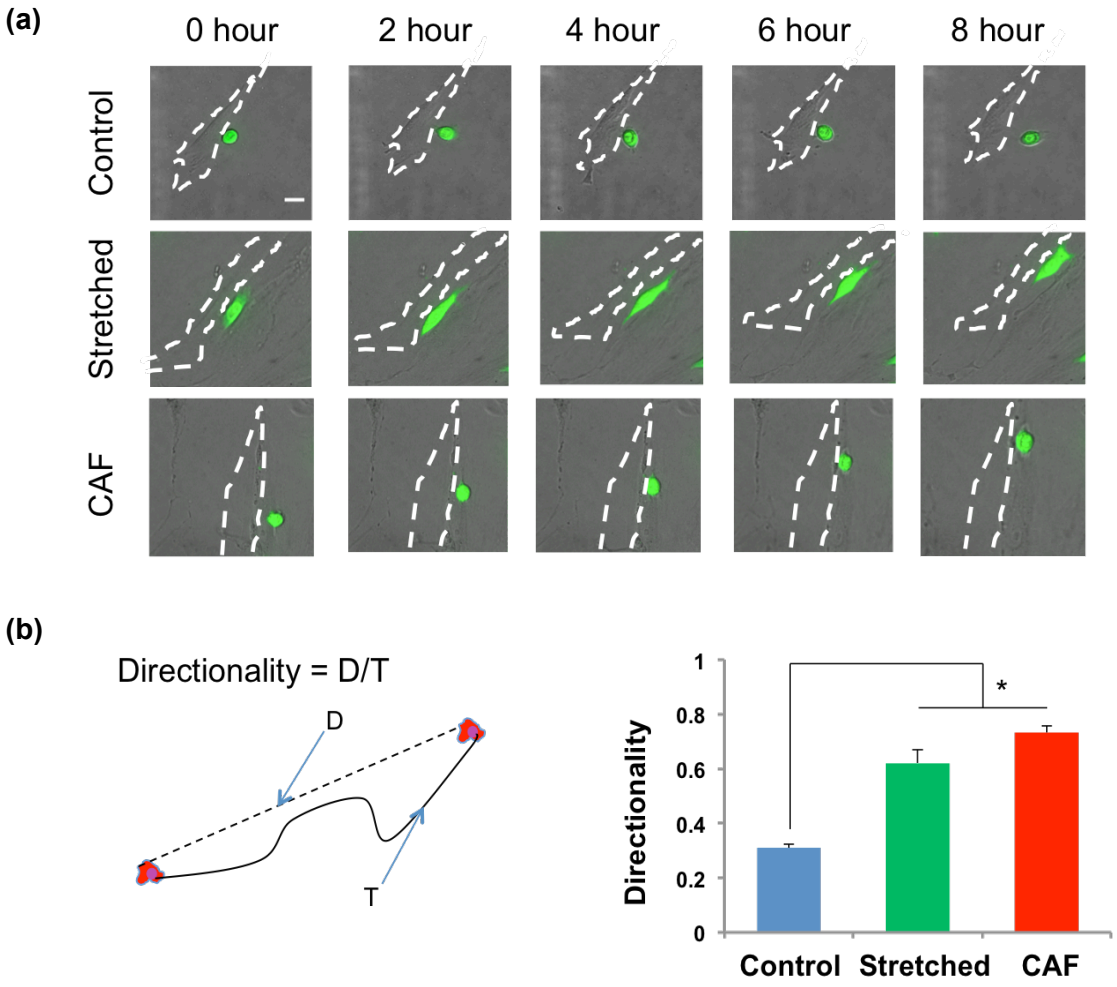

Figure 2.7 Stretched NAFs direct the migration of cancer cells. SCC61 cancer cells (green) were co-cultured with NAFs and CAFs, whose contour is shown with white dashed lines. (a) Time-lapse images show SCC61 cells move randomly when co-cultured with control NAFs (upper panel), but they move along stretched NAFs and migrate in a persistent way (middle panel) similar to SCC61 cells co-cultured with CAFs (lower panel). (b) SCC61 cells show a higher directionality when co-cultured with stretched NAFs or CAFs compared with control NAFs. Error bars represent S.E.M from 25 cells from three individual experiments (*p = 0.007).

In conclusion, we adapted and further improved a microfluidic platform that enables precise, consistent mechanical stretching on cells. Using this platform, the effects of mechanical stretching and relaxation on prostatic NAFs and CAFs were studied. Results indicate that mechanical stretching of NAFs leads to secretion of aligned fibronectin while relaxation of

inherent stress of CAFs results in secretion of randomly distributed fibronectin. Moreover, a significant downregulation of the activated-fibroblast marker, α-SMA, provides further evidence that relaxed CAFs express some NAF-like phenotype. Importantly, co-culture of stretched NAFs with SCC61 cells significantly enhanced cancer cell directional migration, which is similar to the migration patterned when co-cultured with control CAFs but different from the case with the control NAFs. All these results suggest that mechanical stretching and relaxation are critical players in NAF activation and CAF deactivation.

2.4 Investigation of Stretching Effect on Neurons

Mechanical stress also plays an important role in traumatic brain injury (TBI), as discussed in the motivation of this chapter. Here we applied the microfluidic stretcher to investigate cell viability under different stretching conditions.

2.4.1 Material and Methods

I. Cell Loading and Culture in the Microfluidic Stretcher

All stretcher devices were sterilized through UV radiation for 2 h. After sterilization, the cell chamber was coated with 200 µl of 1 mg/ml poly-L-lysine (PLL) (Sigma-Aldrich, St. Louis, MO) in 0.1 M borate buffer (pH 8.5) overnight in an incubator at 37°C. Excess PLL was removed from the chamber by flowing deionized water (sterilized) through the chamber for 2 h. The cell chamber was then equilibrated with B27-supplemented Neurobasal™ media (GIBCO™ Invitrogen, Carlsbad, CA) for 30 min. Hippocampal neurons isolated from dissected brains of E19 rat embryos (50,000 cells) were loaded into the cell chamber at a density of 500,000 cells/ml in neuronal media. The cells were allowed to attach to the PLL coated PDMS membrane in an incubator at 37°C with 5% CO_2 for 2-3 h. After attachment, 200 µl of B27-supplemented

Neurobasal™ media conditioned for 24 h over a confluent monolayer of glial cells (glia-conditioned media) was added to the cell chamber inlet; 100 μl glia-conditioned media was added to the outlet reservoirs to slow down the flow rate. The media was replenished every 36 h, along with the removal of the waste media collected in the outlet reservoir. After stretching, the neurons were stained with the live/dead cell imaging kit (Molecular Probes, Eugene, Oregon) for 20 min at room temperature.

II. Immunofluorescence Imaging

Images were taken using the aforementioned Quorum WaveFX spinning disk confocal system, which was equipped with a Nikon Eclipse Ti microscope, a Plan Fluor 20X objective (NA 0.5) and a Hamamatsu ImagEM EM-CCD camera. Image acquisition was performed using MetaMorph software (Molecular Devices, Sunnyvale, CA).

2.4.2 Results

In order to examine the effect of tensile force on neurons in both phases of TBI, i.e. primary injury phase and secondary injury phase, experiments were conducted under three conditions: (1) static overnight stretching, (2) 5-sec pulse stretching and subsequent release of the stretch, and (3) no stretching (control). The static slow mode is designed to mimic the continuous second injury, while the 5-sec fast mode is to study the immediate primary injury. Before stretching, cells in the three assays were cultured till spread out and extended neuronal processes (Fig. 2.8 (a), (d) and (g)). After being stretched in the microfluidic stretcher with a ~4% strain for long and short periods, neuron cells showed different morphologies and viability. With the overnight stretching, cells appeared in a distinct, round morphology and cell apoptosis occurred extensively (Fig. 2.8 (b) and (c)). In contrast, cells with 5-sec stretching and no stretching maintained initial morphology (Fig. 2.8 (e) and (h)). Cell death is marked with red

fluorescence through the live/dead cell imaging kit, as shown in Fig. 2.8 (c), (f) and (i). Clearly, while cell death is much more severe after overnight stretching, 5-sec stretching at ~4% strain did not cause noticeable cell death.

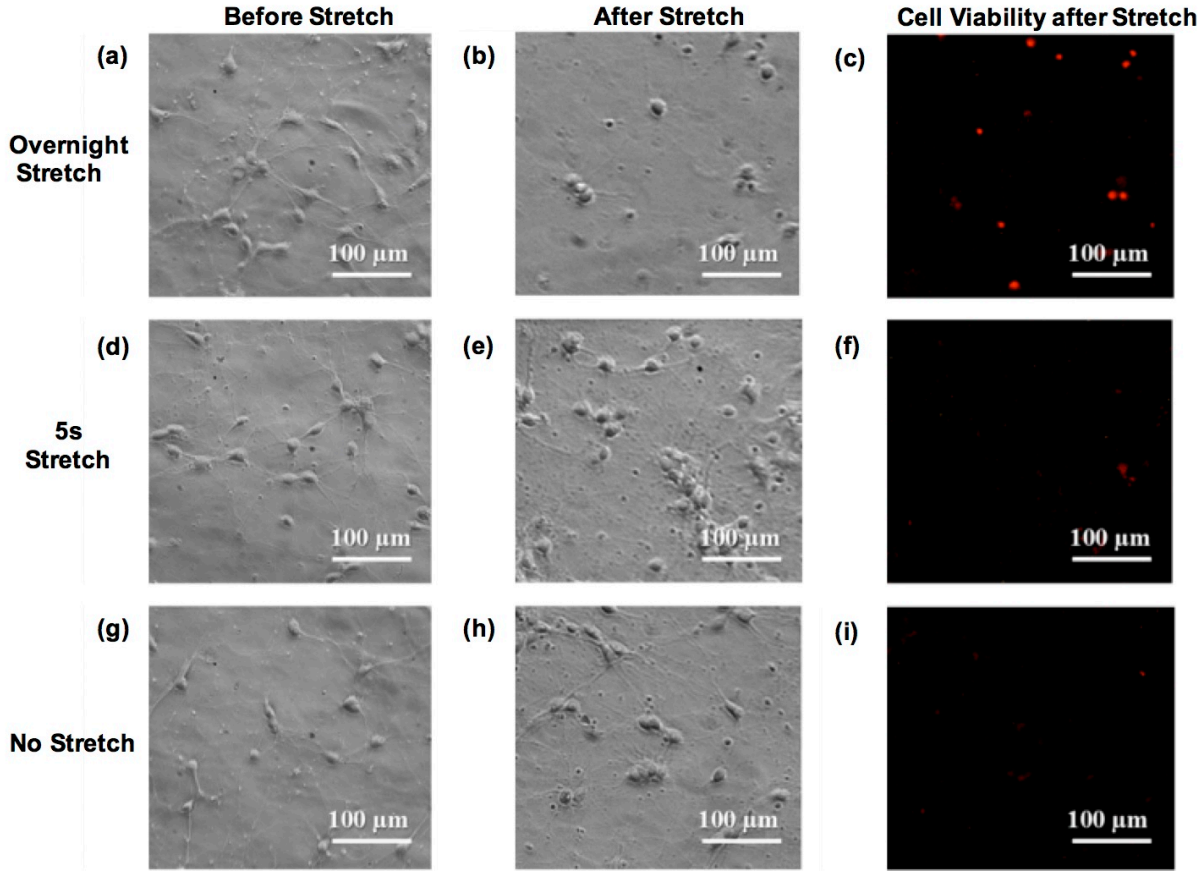

Figure 2.8 Optical images of neurons. Neuron images before (a) overnight stretching; (d) 5-sec stretching; and (g) no stretching control. Neuron images after (b) overnight stretching; (e) 5-sec stretching; and (h) no stretching control. Fluorescence indicators of dead neurons after (c) overnight stretching; (f) 5-sec stretching; and (i) no stretching control.

2.4.3 Design of A Microfluidic Stretcher Integrated with Graphene Probes

We revealed that mechanical stretching in different modes, although at the same strain, affects neuron morphology and viability differently. It is reasonable to believe that neuronal electric activities will be influenced by mechanical stimuli, too. To measure electrical activities,

a new microfluidic stretcher integrated with graphene transistors is proposed to allow for simultaneous electrical signal recording under mechanical stretching. This design is built upon the microfluidic stretcher and the graphene transistor based microfluidic co-culture sensing platform that will be introduced in Chapter IV. The device consists of 4 layers (see Fig 2.9). The first layer is a 100 μm-thick open-channel PDMS bottom layer bonded to a coverslip with a network of microchambers, forming support for two inner neuron culture chambers as well as two adjacent glia culture chambers on a suspended membrane. The reason of culturing neurons with the presence of glia cells is because glia cells have proven to enhance the health of neuronal cells[100]. The second layer is a 10 μm-thick PDMS membrane only anchored on the walls between vacuum chambers and glia chambers. Holes are punched at the vacuum chambers to connect the lower and upper segments. An array of gold electrodes is patterned on this membrane followed by a graphene layer placed on the top. The third layer stacked on the membrane is a PDMS piece possessing identical features as the first layer. This layer forms neuron and glia cell culture chambers and the upper half of the vacuum chambers. Neuron and glia cell culture chambers are connected with a series of 5 μm-tall microgroove valves. The fourth layer is a PDMS pressure chamber, which can be hydraulically pressurized, thereby deforming the microgrooves to separate neuron culture chambers and the outer glia culture chambers. By applying vacuum pressure to vacuum chambers via tubing, the wall between the vacuum and glia chambers deforms, imparting tensile stress on cells cultured on the suspended membrane, as shown in Fig. 2.9 (c). This design allows for future investigation on synaptic electric activity upon mechanical stimuli.

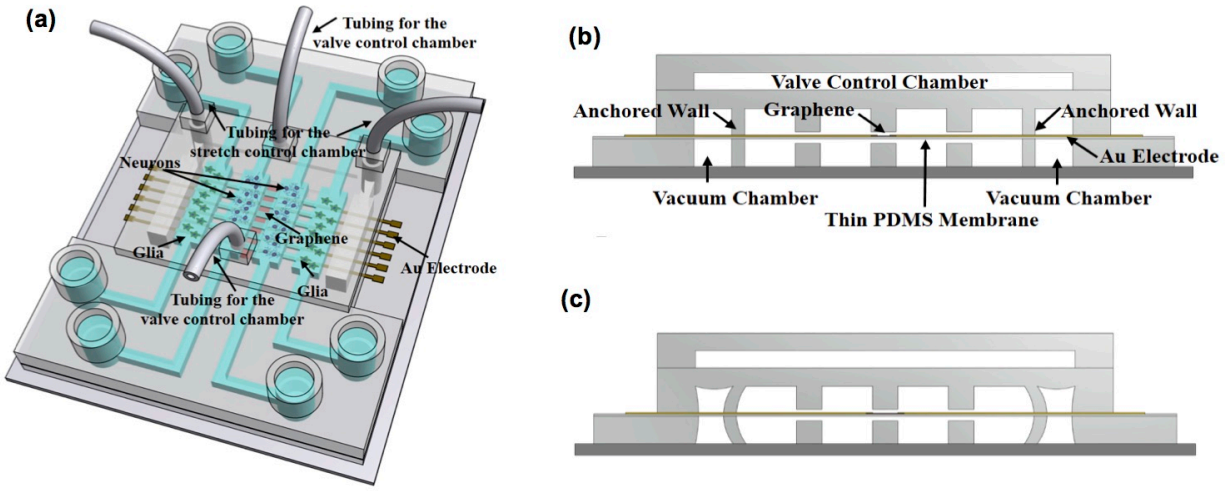

Figure 2.9 Schematic of a microfluidic stretcher integrated with graphene transistors. (a) Top view, (b) unstretched, and (c) stretched cross-section view.

2.5 Summary

In this chapter, we designed and constructed a series of microfluidic stretchers to examine cell mechanotransduction in response to mechanical stretching and stress relaxation. The stretcher was characterized using confocal microscopy and COMSOL^{TM} modeling, showing strain change with respect to vacuum pressures, sidewall heights, and cell chamber widths. We demonstrate that mechanical force is a critical factor in regulating the fate of NAFs and CAFs, and subsequently directing cancer cell migration in different manners via fibronectin organization. Further, we studied the morphology and viability of primary hippocampal neurons subject to different types of stretching. Clearly, long-time stretching inflicted more severe damage to neuron cells than the short-time pulse did at the same strain, indicating that the secondary brain injury may be more harmful than the primary injury. Additionally, a neuron-glia co-culture microfluidic stretcher integrated with graphene probes is proposed in order to investigate the electrical activities under various mechanical stimuli in the future.

CHAPTER III

INVESTIGATION OF THE EFFECT OF COMPRESSION ON NAFS/CAFS IN A THREE-DIMENSIONAL MATRIX

3.1 Motivation

In the last chapter, we discussed altered cellular phenotype and fate as well as viability in response to mechanical stretching and stress relaxation. In this chapter, we move to another mechanoresponsive behavior: cell reorientation. Numerous reports have demonstrated that cells cultured on an elastic substrate subjected to a uniaxial cyclic stretch tend to reorient themselves away from or perpendicular to the stretch direction[41–45,139–141], which is often referred to as stretch-avoidance or strain-avoidance[142]. Concurrent with cell reorientation, the remodeling of SFs in response to a stretch stimulus has also been observed. Ventral SFs, as the most commonly observed SF type, are long and extend most of the length of cells[143]. The two ends of ventral SFs are anchored to the ECM via focal adhesions (FAs), forming both outside-in and inside-out mechanotransduction pathways[144]. Numerous studies have suggested that SFs play a critical role in cell reorientation and morphogenesis under mechanical stimuli[41–43,145–148]. Furthermore, it has been shown that inhibition of SF formation leads to cell alignment with the stretch direction, indicating SFs are critical for cell stretch-avoidance or strain-avoidance[36].

The mechanism of the observed cell reorientation in response to a uniaxial stretch has been previously discussed. For example, one theoretical model proposed that actin filaments orient to the direction in which the deformation of the stretched substrate is minimal so that the energy of SFs is least disturbed[149]. This hypothesis was confirmed with experiments conducted

on both fibroblasts and endothelial cells. Another study suggested that the reorientation was driven by a dissipative process in which the passively stored cell elastic energy relaxed to a minimum through aligning cell bodies away from the stretch direction[43]. A statistical thermodynamics analysis considering passive mechanical responses and active subcellular dynamic remodeling predicts that cells tend to orient in the direction in which SF formation is energetically most favorable[150]. Other studies suggested that SFs would align in the direction in which the total energy reaches a minimum[141,145] and explained the realignment of SF-FA assembly in response to substrate stretching[151] on the basis of Maxwell's global criterion for stability. In addition to these analyses based on an energetic argument, it has also been predicted that stretch-induced SF disassembly is an important factor in determining the rate of cell alignment[147]. In short, it is believed that cell reorientation under stress is driven by the tendency of cell energy minimization, and that SFs play a critical role in mediating this process.

Despite these significant findings, some important issues of cell behavior under stress still need to be addressed. First, most studies of cell reorientation in response to a mechanical stimulus, whether experimental or theoretical, are conducted with cells on a flexible two-dimensional (2D) substrate, which is different from the 3D microenvironment *in vivo*. To date, only a few investigations have been carried out to probe cellular responses to mechanical forces in a 3D environment, and the resulting cell behaviors differ from those observed in 2D studies. For example, two studies reported that fibroblasts aligned themselves along the stretch direction in 3D, which is contradictory to the stretch-avoidance displayed in 2D[54,152,153]. This apparently inconsistent behavior has been hypothesized as a result of cells in 3D interacting with the matrix, sensing the applied force, and reorienting in a different manner[64]. However, this speculation does not adequately address the mechanisms by which cells behave differently in 2D and 3D

environments. Another report demonstrated that cells, as well as F-actin, exhibited stretch-avoidance at the surfaces of a collagen matrix but showed no preferable orientation in the core of the gel under stretching[154]. The authors hypothesized that the different cell behaviors observed at the surface and inside the gel are due to contact guidance from the collagen fibrils interfering with cell orientation in the bulk of the matrix; however, in another work[152], it was shown by scanning electron microscopy (SEM) for cell-seeded and cell-free collagen fibrils that contact guidance only plays a marginal role. As such, cell response to mechanical stimuli in 3D environments is different from and more complex than those observed on 2D substrates, and the underlying mechanism is still not clear.

Importantly, while the role of cell contractility in cell orientation has been recognized in previous stretching studies in 2D through inhibition of cell contractility[36,42,44,140,141], studies with 3D conditions are still lacking. Moreover, besides the tensile force that has been examined in most previous studies, compression is another common type of mechanical stimulus *in vivo*. For example, articular cartilage and cardiac fibroblasts experience both tensile and compressive forces[21]. Uncontrolled tumor growth in a limited space can induce a continuous mechanical compressive stress in the tumor and the surrounding cells and tissue[155]. Reports have shown that compression alters gene expression[56,57,59,156], cell morphology[156,157], differentiation[67], alignment[64,65,156], and proliferation/apoptosis[59]. Interestingly, it has been reported that fibroblasts and smooth muscle cells realign themselves perpendicular to the direction of compression due to the contact guidance of collagen fibrils[67]. However, again, this possibility has been discounted by SEM images of collagen fibrils in other reports [64,152]. As such, the mechanism underlying cell alignment in response to compression is still largely unknown.

In view of the fact that it is currently not clear how and why cells of different contractility realign in response to 3D compression, we investigated the response of human prostatic NAFs and CAFs to static compression in a 3D collagen I matrix. We experimentally demonstrate that a difference in cell contractility affects cell realignment in response to compression and construct a theoretical model based on the minimum energy principle to provide insights into the different behaviors of NAFs and CAFs under compression.

3.2 Material and Methods

3.2.1 Cell Culture

The human prostatic NAFs and CAFs used in this study were isolated as previously described[135]. Cells were maintained in Roswell Park Memorial Institute (RPMI) 1640 medium with 10% fetal bovine serum (FBS) and penicillin–streptomycin as previously described[32,158].

3.2.2 Preparation and Loading of 3D Collagen I Gel and Cell Mixture

NAFs and CAFs were labeled with CellTracker™ Green dye (Life technology, Carlsbad, CA) 24 h prior to being embedded in 3D collagen I gels (rat-tail type I collagen, BD Biosciences, Bedford, MA). Then, the collagen I was mixed in PBS to a final concentration of 2 mg/ml, and the pH was neutralized with 1 N NaOH on ice, per manufacturer's instructions. NAFs and CAFs were dissociated and re-suspended in RPMI culture media (250,000 cells/ml) on ice. Cells were then mixed with collagen I solution to a final suspension of ~75,000 cells/ml for each 2 mg/ml collagen I gel mixtures. Next, 700 µl of the cell-gel mixture was loaded into a 4-well Nunc™ Lab-Tek™ II Chamber Slide™ (Cole Parmer, Vernon Hills, IL) and incubated for 30 min at 37°C to allow the collagen I gel with embedded cells to solidify. Subsequently, culture media

was loaded into the cell chambers, and the cells were incubated at 37°C overnight and then used for compression assays and imaging[159].

3.2.3 The Cell-compression Fixture

The cell compression fixture is composed of three layers of glass slides (25 mm wide, 75 mm long and 1.0 mm thick, VWR International, LLC, Suwanee, GA). The middle layer consists of two shorter glass slides (32.5 mm long) that were stacked on top of the bottom glass slide with a ~10 mm gap in-between them (see Fig. 3.1 (a)). For the laterally confined case, the gap was made the same as the width of the cell-gel mixture. In this case, when subjected to vertical compression by another glass slide from the top (Fig. 3.1 (b)), the cell-gel mixture was restricted in the lateral direction denoted by the blue arrows in Fig. 3.1 (a), but could expand freely in the direction denoted by the red arrows. In the laterally unconfined scenario (see Fig. 3.1 (c)), the gap between the two middle layer glass slides was wider than the cell-gel mixture, allowing the mixture to expand freely in both directions under vertical compression (see Fig. 3.1 (d)). During the compression assay, the cell-gel mixture was carefully transferred from the Nunc™ Lab-Tek™ II Chamber Slide™ to the fixture, and another glass slide was placed on top as shown in Fig. 3.1 (b, d). The cell-gel mixture (1.4~1.5 mm thick) was compressed to 1 mm thick; thus, ~30% compressive strain was applied to the gel along the vertical direction. The assembly was secured using binder clips and submerged in a petri dish filled with media, and the cell-gel mixture was subjected to compression overnight (~18 h).

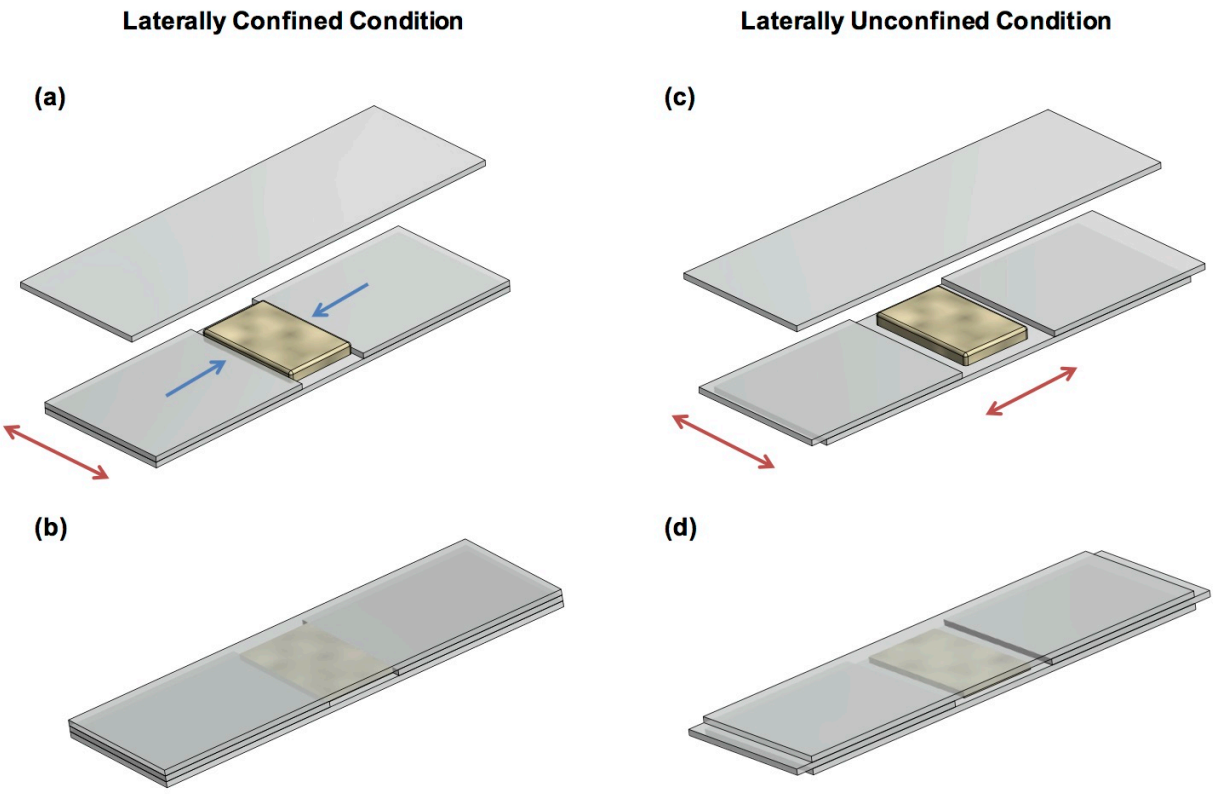

Figure 3.1 Schematic of the cell-compression assay. (a, b) In the laterally confined condition, the middle layer of glass slides formed a gap the same as the width of the cell-gel mixture so that the expansion of the gel in this direction was restricted. (c, d) In the laterally unconfined condition, the middle layer of glass slides formed a gap wider than the cell-gel mixture so that the gel can expand in both directions. The cell-gel mixture was compressed vertically by pressing another glass slide from the top. The blue arrows denote the laterally confined direction, while the red ones indicate the free (unconfined) directions.

3.2.4 Determining Cell Orientation Using Fluorescence Microscopy

Images of the cells in the 3D compression fixture were collected using a Quorum WaveFX-X1 spinning disk confocal system, which contained a Nikon Eclipse Ti microscope (Melville, NY), an EM-CCD camera (Hamamatsu, Hamamatsu City, Japan), and a 10X ADL objective (NA 0.25), with MetaMorph software. The Quorum confocal system has a Yokogawa CSU-X1 spinning disk (Yokogawa Electric Corporation, Newnan, GA) with Borealis

upgrade/modifications (Guelph, Canada) and the CellTracker™ Green dye was excited using a 491 nm laser line. The emission filter used was 525/50 from Semrock (Rochester, NY).

3.2.5 Determining Cell Orientation using Fast Fourier Transform

Fast Fourier Transform (FFT) was used as previously reported[160] to statistically characterize the cell orientation for each compression result. FFT was performed on a fluorescence confocal microscopy image of the cells using ImageJ software (NIH, http://rsb.info.nih.gov/ij) with the Oval Profile plug-in (authored by William O'Connnell). A 512 pixel diameter circle was overlapped with the FFT output image (2048×2048 pixels) in the center, and a radial summation of gray value intensities over the circle was conducted with a resolution of single radial degree. We further normalized the radial intensity through dividing it by the total intensity. Note that in order to generate more statistically significant data, nine representative fluorescence micrsocopy images from different locations within the cell-gel mixture were merged into a single montage. These stitched images were then analyzed using the FFT method described above.

3.2.6 Collagen Gel Contractility Assay

NAFs and CAFs were suspended in full growth medium at a density of 600,000 cells/ml. Rat tail collagen I was diluted to 3 mg/ml in PBS, and the pH was neutralized with 1 N NaOH. Cell suspension and the collagen I gel solution were mixed at a 1:2 ratio to get a final mixture with 200,000 cells/ml of cells and 2 mg/ml of collagen I gel. 600 µl of the above mixture was loaded into each well of a 12-well-plate and incubated at 37°C for 1 h to allow the gel to polymerize. Gels were then covered with 1 ml of medium and detached from plates using a pipette tip by gently circling around the inside wall of each well. Gels were incubated at 37°C for

the indicated time to allow for contraction. The gels were imaged, and the gel area was measured from scanned gel images using imageJ. Cell contractility was assessed by calculating the percentage of the final gel area to the initial gel area after different time periods.

3.2.7 Western Blot

Cell lysates from NAFs and CAFs were prepared using RIPA buffer (50 mM Tris-HCl, pH 7.4, 150 mM NaCl, 1% NP-40, 0.25% sodium deoxycholate and 1 mM EDTA), supplemented with a protease inhibitor cocktail (Sigma-Aldrich, San Louis, MO). Equal amount of cell lysates (30 μg) were run in polyacrylamide gels and transferred to nitrocellulose membranes, which were then blotted for α-SMA (clone 1A4) and anti-tubulin (clone DM1A) (Sigma-Aldrich). Infra-red dye conjugated secondary antibodies (IRDye 680 and 800, LI-COR Biosciences, Lincoln, NE) were used to detect bands in the Odyssey infrared imaging system (LI-COR Biosciences). Western blot band intensities were determined using Image Studio Lite version 4 (LI-COR Biosciences). α-SMA band intensity was normalized to tubulin, which was a loading control.

3.2.8 Transforming Growth Factor *β* (TGF-*β*) Stimulation Assay

The NAF-gel mixture was prepared following the same protocol as described in section 3.2.2 and 3.2.3, with 10 μl TGF-*β* (1 μg/ml) added to the media before being subjected to compression overnight (~18 h).

3.3 Experimental Results

The fluorescence images of NAFs and CAFs were taken at both the beginning and the end of the 3D compression assay. We found that CAFs exhibited a random distribution after

overnight compression in the laterally confined condition (see Fig. 3.2 (a, b)), i.e., no favorable orientation of CAFs was observed. In contrast, NAFs initially exhibiting a random distribution (Fig. 3.2 (f)) were aligned to the free direction (denoted by a red arrow) and away from the laterally confined direction (indicated by blue arrows) after compression, as shown in Fig. 3.2 (g).

To quantify the cell orientation, FFT was performed on the fluorescence images. The image of CAFs at the end of compression (Fig. 3.2 (b)) generates a round-shaped FFT output image with rather evenly distributed pixel intensities (Fig. 3.2 (c)) in which no particular angle is favored. In contrast, the image of compressed NAFs (Fig. 3.2 (g)) produces a spindle-shaped FFT image, as shown in Fig. 3.2 (h), meaning the pixel intensities are higher along one specific direction.

The FFT frequency distribution with respect to the angle was generated by carrying out a radial summation of the pixel intensities over the aforementioned circle for every degree between 0° and 179°. The FFT image is symmetrical; and therefore draws no distinction for the other semi-circle[161]. Fig. 3.2 (d) and (i) show the normalized summed pixel intensities versus angles, which provides a quantitative description of cell alignment. The shape and location of the peaks of the FFT plots exhibit the extent and direction to which the cells align. Fig. 3.2 (i) clearly shows a prominent peak at 90°, indicating that NAFs aligned along the free direction after being compressed overnight. It is worth noting that the FFT output images yield frequencies orthogonal to those in the original images[161]. On the other hand, Fig. 3.2 (d) shows that CAFs do not exhibit a preferred direction in which the pixel intensity is noticeably higher than those along other directions (note that the fluctuations are due to the limited number of samples and the distributed peaks are not preferred directions, which is verified by the fact that the peaks appear at different

angles in different tests). The same trends were observed for multiple trials and the average of the normalized intensities from four independent experimental results are plotted in Fig. 3.2 (e) and (j). For NAFs, the averaged distribution is very similar to that from each test while for CAFs, the fluctuation peaks are canceled out significantly after this operation, leading to an even flatter average distribution. The error bars in Fig. 3.2 (e) are significantly larger than those in Fig. 3.2 (j), further underscoring the random orientation of CAFs from experiment to experiment.

Importantly, not only did NAFs realign themselves in the horizontal plane to the free direction, but they also steered away from the compressed direction. A set of *z*-stack fluorescence images in Fig. 3.3 (a) clearly demonstrate that laterally confined compressed CAF cells distributed in different focal planes in a range of 70 μm. In contrast, laterally confined compressed NAFs, in Fig. 3.3 (b), located in almost the same focal plane under compression. The whole cell body gradually came into sight and went out of sight at the same time. Without any compression, NAF cells showed no favored direction and were situated in different focal planes with protrusions spanning 70 μm in the *z*-direction, as shown in Fig. 3.3 (c).

For the laterally unconfined case, the fluorescence images (Fig. 3.4 (a, e)), FFT output images (Fig. 3.4 (b, f)) and radial summation plots (Fig. 3.4 (c, g)) all show that similar to the laterally confined case, CAFs show a random distribution after being compressed overnight; however, the NAFs, instead of aligning to one direction, are reoriented into two directions with angles around 45° and 135° relative to the *x*-direction. Again, the trend was observed for multiple experiments (Fig. 3.4 (d, h)).

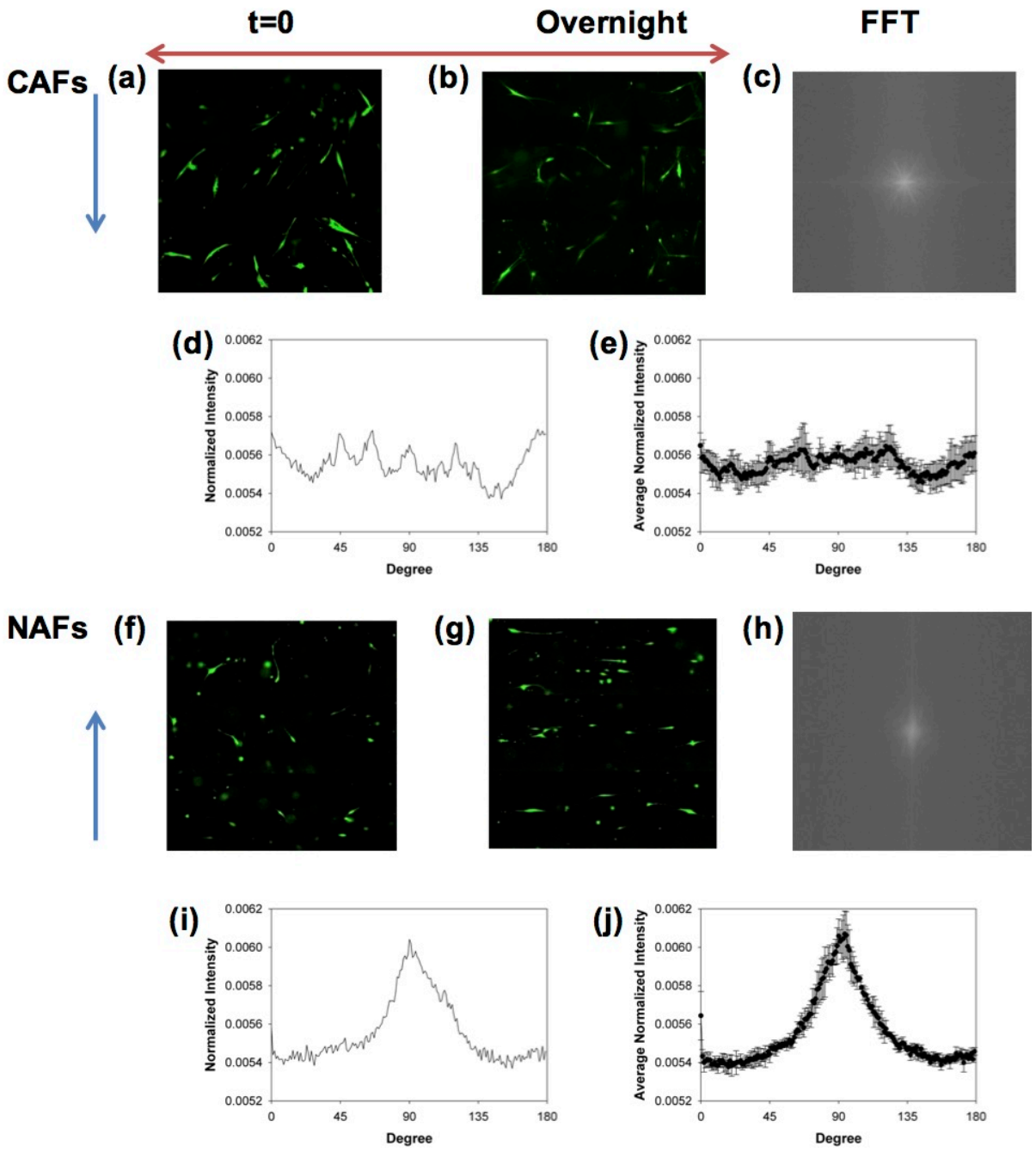

Figure 3.2 Different alignments of CAFs and NAFs exposed to laterally confined compression. (a, f) Montages of fluorescence images show CAFs and NAFs at the beginning of compression. (b, g) Montages of fluorescence images show CAFs and NAFs after overnight compression. (c, h) FFT output images of CAFs and NAFs after overnight compression. (d, i) Normalized radial summation of pixel intensities over a circle projection of FFT images of CAFs and NAFs after overnight compression. (e, j) The average normalized pixel intensity of CAFs and NAFs from four independent experiments. The blue and red arrows indicate the laterally confined and free directions, respectively.

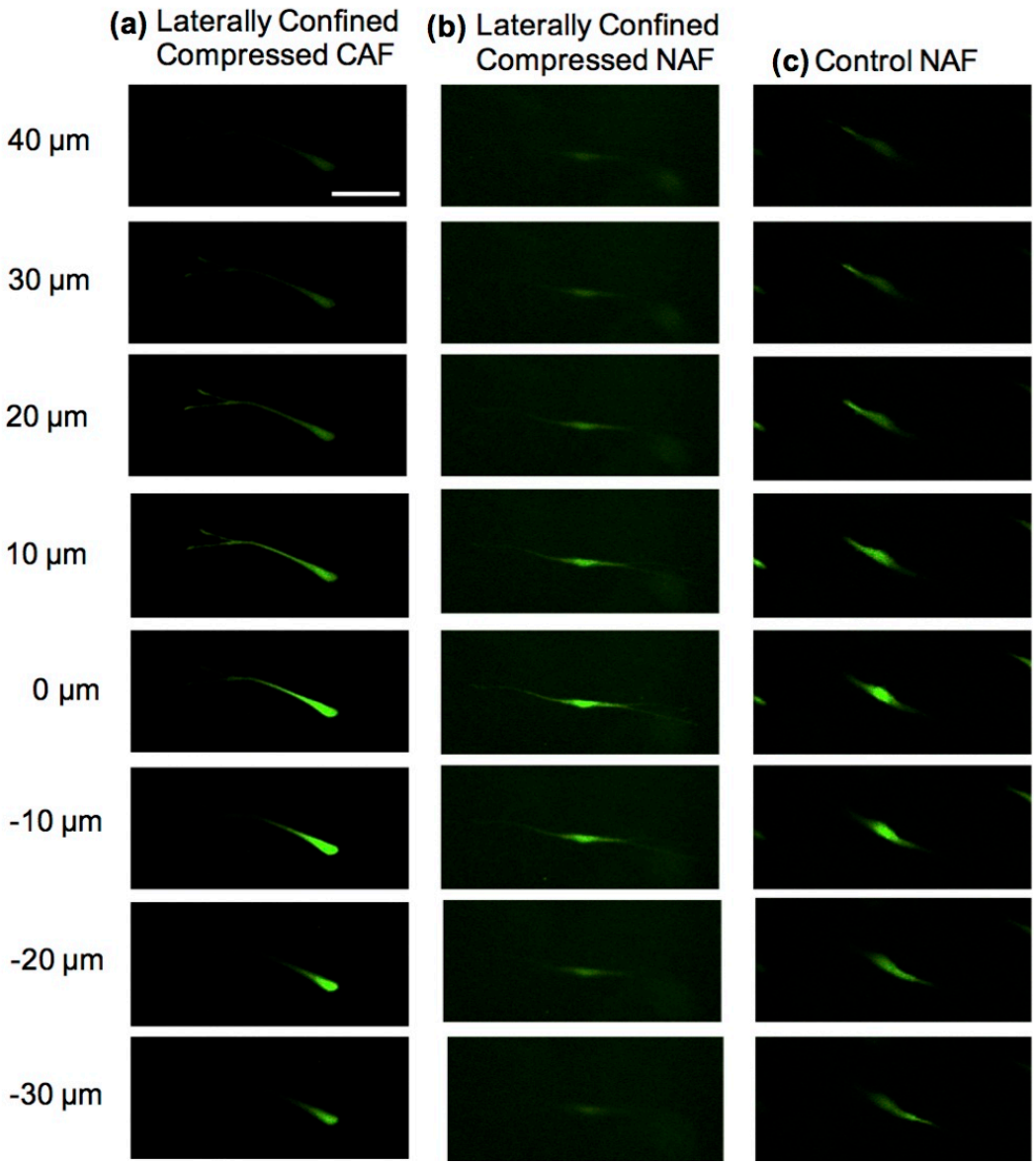

Fig. 3.3 Cell vertical orientation. (a) A CAF distributes in different focal planes under laterally confined compression. (b) A NAF realigns perpendicular to the compressed direction under laterally confined compression and locates in the same focal plane. (c) A NAF in the control group locates in different focal planes, the scale bar is 100 μm

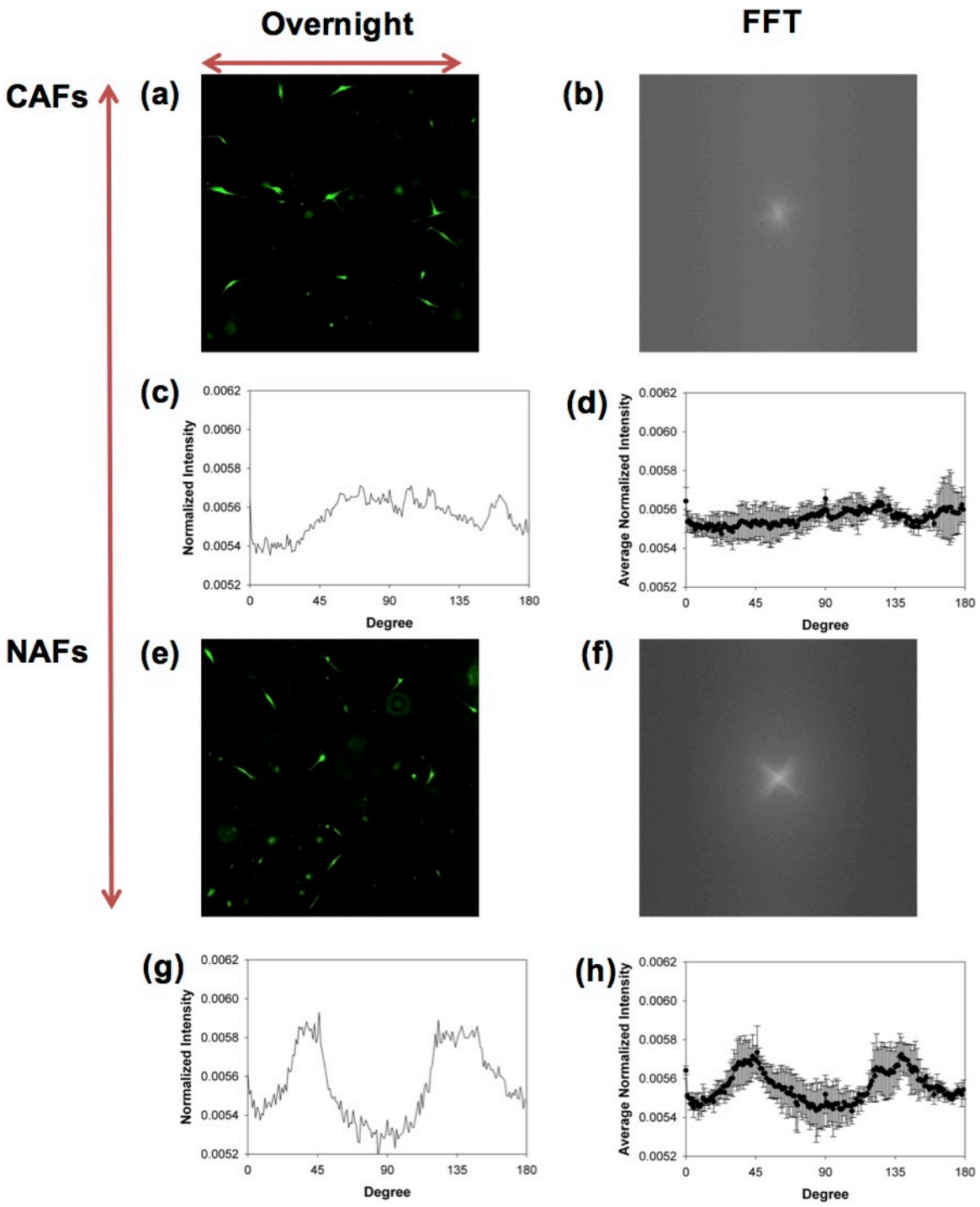

Figure 3.4 Different alignments of CAFs and NAFs exposed to laterally unconfined compression. (a, e) Montages of fluorescence images of CAFs and NAFs after overnight compression. (b, f) FFT output images of CAFs and NAFs after overnight compression. (c, g) Normalized radial summation of pixel intensities over a circle projection of FFT images of CAFs and NAFs. (d, h) The average normalized pixel intensity of CAFs and NAFs from three independent experiment. The red arrows show the free directions

3.4 Theoretical Modeling

3.4.1 Assumptions

In the theoretical modeling, we first deal with the laterally confined case and then extend the model to the laterally unconfined scenario. For the laterally confined case, we consider a single cell embedded in a collagen I gel subjecting to compression in the *z*-direction. The gel is confined in the *y*-direction but can expand freely in the *x*-direction. We construct the model based on the energy minimization principle, i.e., cells tend to realign themselves to achieve minimum energy. The model also considers the important role of SFs in the reorientation and morphogenesis of cells. We assume that the cell is composed of bundles of SFs that are parallel to the axis of the cell. From an energy consideration, this bundle can be regarded as equivalent to a single SF with corresponding stiffness of the whole bundle. Since the SF is composed of assembled actin filaments, we assume that the SF is a spring system that consists of a number of identical short actin filament springs connected in series.

For simplicity and based on the fact that the model is a thermodynamic analysis, we treat the collagen gel as an elastic material[162,163] with linear stress-strain relationship. The boundary conditions imposed led to no normal force in the *x*-direction at equilibrium; however, forces in the *y*- and *z*- directions always exist and will be transmitted to the cell. It is important to note that before reaching equilibrium, expansion of the gel in the *x*-direction will also stretch the cell.

The energy analysis on the cell was conducted following the minimum energy principle requiring that the equilibrium orientation of the cell should be energetically preferred. The favored orientation for cells exhibiting lower contractility is the free, unconfined *x*-direction in the case of laterally confined compression. This is because in the *x*-direction, the tension of the

cell caused by the expansion of the gel can be gradually relaxed by aggregated actin filaments. This argument is consistent with the fact that when exposed to external mechanical stress, actin filaments aggregate to form SFs[164]. The rearrangement and redistribution of actin filaments serve to reduce the overall stress[165]. As such, the strain on the cell that results from the elongation of individual actin filaments due to external stretch will be relaxed by additional actin filaments assembled into the SFs. Therefore, at the equilibrium length, we assume that the axial tension is eventually eliminated by the assembled actin filaments if the polarity of the cell body is aligned in the unconfined *x*-direction. By adjusting its orientation and assembling actin filaments, the total energy of the cell could be minimized.

Because living cells, even in the absence of external mechanical loads, possess pre-stressed SFs due to inherent cell contractility[151], we take this pre-stressed condition into account in our model. Previous studies have shown that the contractile force direction is parallel to the polarity of an elongated cell[166]. Recognizing that fibroblasts are highly elongated cells, it is reasonable to assume that the contractile force only exists in the polarized direction while contractile forces in other directions can be neglected. Importantly, it has been shown that SF shortening is rarely seen in normal live and healthy cells[143]; and therefore, the stress in the vertically compressed and laterally confined directions cannot be released by shortening SFs. Built on the above understanding, our model predicts that cells both with or without significant inherent contractility will realign in an equilibrium orientation where the total cell energy is minimized.

3.4.2 Model Formulation

Here we lay out a theoretical model based on the minimum energy principal in order to address the mechanism underlying cell reorientation in response to compression in 3D.

I. Laterally Confined Condition

a. Stress and strain analysis for the collagen gel

To model the cell reorientation, we first consider a small collagen gel cube surrounding a cell. According to the 3D Hooke's Law, at equilibrium, the strains ε along the *x*-, *y*-, and *z*-directions are as follows:

$$\varepsilon_x = \frac{1}{E_g}\left(\sigma_x - \nu_g\sigma_y - \nu_g\sigma_z\right), \tag{3.1}$$

$$\varepsilon_y = \frac{1}{E_g}\left(-\nu_g\sigma_x + \sigma_y - \nu_g\sigma_z\right), \tag{3.2}$$

$$\varepsilon_z = \frac{1}{E_g}\left(-\nu_g\sigma_x - \nu_g\sigma_y + \sigma_z\right). \tag{3.3}$$

Here ν_g is Poisson's ratio, E_g is Young's modulus, and σ_i is stress, assuming that the collagen gel is linear elastic. The gel is compressed along the *z*-direction and laterally the gel is confined in the *y*-direction but can expand freely in the *x*-direction. As such, we have $\sigma_x = 0$, $\varepsilon_y = 0$, and $\varepsilon_z = \Delta z/l_g$. Here Δz is the displacement caused by compression in the *z*-direction and l_g is the length of each side of the cube. The stresses in the *x*-, *y*-, and *z*- directions are therefore

$$\sigma_x = 0,$$

$$\sigma_y = E_g \varepsilon_z \nu_g \left(1 - {\nu_g}^2\right) = E_g \frac{\Delta z}{l_g} \nu_g \left(1 - {\nu_g}^2\right), \tag{3.4}$$

$$\sigma_z = E_g \varepsilon_z \left(1 - {\nu_g}^2\right) = E_g \frac{\Delta z}{l_g} \left(1 - {\nu_g}^2\right).$$

Meanwhile, the strains in the *x*-, *y*-, and *z*- directions can be re-written as

$$\varepsilon_x = -\varepsilon_z \nu_g \left(1 + \nu_g\right)^2 \left(1 - \nu_g\right),$$

$$\varepsilon_y = 0, \tag{3.5}$$

$$\varepsilon_z = \frac{\Delta z}{l_g}.$$

b. Energy analysis for the cell

The total energy E of a cell consists of the homeostatic elastic potential E_0 due to cell contraction[149], the elastic potential converted from the external mechanical load E_e, the chemical potentials of assembled actin filaments E_a and free actin filaments E_f, and the energy exchanged with the surrounding microenvironment E_s[167].

$$E = E_0 + E_e + E_a + E_f + E_s. \tag{3.6}$$

We consider the cell energy under two situations, i.e., with and without external mechanical load. Assuming that the cell axis forms angles of θ_x, θ_y, and θ_z with the coordinate

axes x, y and z (Fig. 3.5) and without losing any generality, we can set $0 \leq cos\theta_x \leq 1, 0 \leq cos\theta_y \leq 1, 0 \leq cos\theta_z \leq 1$.

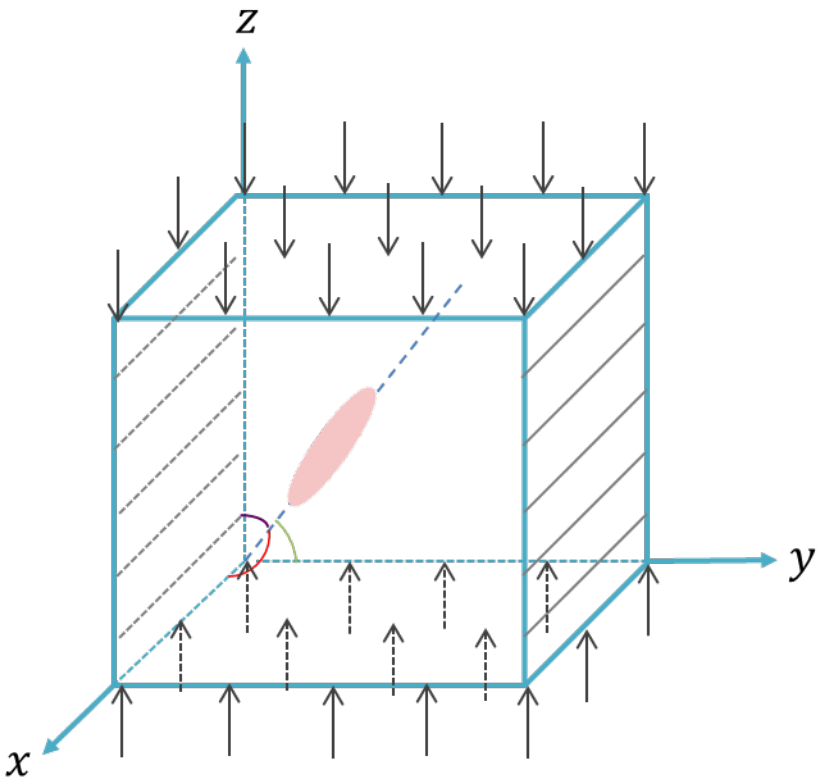

Figure 3.5 A single cell embedded in a cubic collagen gel. The cell represented by a pink oval forms angles of θ_x, θ_y and θ_z with coordinate axes x, y and z (denoted by red, green and purple curves). The gel-cell mixture is subjected to confinement in the y-direction and compression in the z-direction (denoted by black skew lines and black arrows, respectively).

1) Without an external mechanical load

With no external force, the total energy of the cell is

$$E = E_0 + E_a + E_f + E_s. \tag{3.7}$$

This can be expanded to

$$E = \frac{1}{2} k_{sf} (l\varepsilon_0)^2 + N_a \mu_a + N_f \mu_f + E_s, \tag{3.8}$$

where l is the length of the cell, ε_0 is the pre-stretched strain, μ_a and μ_f are the chemical potentials of assembled and disassembled actin filaments, N_a and N_f are the number of assembled and disassembled actin filaments.

We further assume that the cell is composed of a single equivalent SF that is parallel to the axis of the cell body and extend the length of the cell. Also, the SF consists of a number of actin filaments of length l_a. Each actin filament can be regarded as a spring with a spring constant of k_a; and therefore, the SF is a spring system composed of a series of identical actin filament springs. The spring constant of the SF is $k_{sf} = k_a / N_a$. Hence,

$$l = N_a l_a, \tag{3.9}$$

$$E = \frac{1}{2} \frac{k_a}{N_a} (N_a l_a \varepsilon_0)^2 + N_a \mu_a + N_f \mu_f + E_s. \tag{3.10}$$

Taking the derivative of E yields

$$dE = \frac{1}{2} k_a {l_a}^2 {\varepsilon_0}^2 dN_a + \mu_a dN_a + \mu_f dN_f + dE_s. \tag{3.11}$$

In cells, actins exist in two forms: actin filaments and free monomeric actins that can polymerize into actin filaments. The pool of actins is steady in a cell, and hence the total amount of actins is conserved[168], which leads to the following relation: $N_a + N_f = const$. Therefore, $dN_a = -dN_f$, and Eq. 3.11 can be rearranged as:

$$\frac{dE}{dN_a} = \frac{1}{2} k_a {l_a}^2 {\varepsilon_0}^2 + \mu_a - \mu_f + \frac{dE_s}{dN_a}. \tag{3.12}$$

At equilibrium, the cell energy achieves a minimum, and $dE/dN_a = 0$. Therefore,

$$\mu_a = \mu_f - e_0 - e_s, \tag{3.13}$$

where $e_s = dE_s/dN_a$; and $e_0 = k_a {l_a}^2 {\varepsilon_0}^2/2$, which is the elastic potential of each actin filament due to cell contraction.

2) With an external mechanical load

Under this condition, the total energy of the cell as given by Eq. 3.6 can be expanded as

$$E = N_a e_0 + \frac{1}{2} k_{sf} \left[\left(\varepsilon_{xc} l - \frac{\sigma_{yc} l}{k_{sf}} - \frac{\sigma_{zc} l}{k_{sf}} \right)^2 - (\varepsilon_0 l)^2 \right] + N_a \mu_a + N_f \mu_f + E_s, \tag{3.14}$$

Since we assume that the SF is a spring system along the long axis of the polarized cell body, only strains along this direction change the elastic potential and contribute to E_e. Here ε_{xc} is the strain along this axis of the cell body caused by the gel displacement in the *x*-direction, which is released by gradually assembled actin filaments before reaching equilibrium. This component results in stretching of the cell. σ_{yc} and σ_{zc} are the stress components along the long axis of the cell body caused by the forces applied to the cell from the gel in the y- and z-directions. The different signs of terms of $\varepsilon_{xc} l, \sigma_{yc} l/k_{sf}, \sigma_{zc} l/k_{sf}$ reflect the opposite directions. As such, the total strain along the long axis of the cell body is $\varepsilon_{xc} - \sigma_y cos\theta_y N_a/k_a - \sigma_z cos\theta_z N_a/k_a$. Since the pre-stretch energy has already been considered in the first term, the displacements in the second term are from the external mechanical load alone.

Now we consider ε_{xc}. The strain that results from the elongation of individual actin filaments due to gel expansion is eventually released by the assembly of additional actin filaments, and SF return back to the homeostatic state prior to the application of mechanical

force, as shown in Fig. 3.6 (a)~(c). This concept is consistent with previous observations that cells actively respond to perturbations from the ECM by re-establishing the homeostatic level of force and maintaining fiber strain under normal condition[148,169]. Therefore, SF elongation caused by gel expansion ε_x is achieved by more assembled actin filaments and ε_{xc} satisfy the equation as follows:

$$N_a l_a(1+\varepsilon_{xc}) = N_0 l_a(1+\varepsilon_x cos\theta_x), \tag{3.15}$$

where N_0 is the number of the assembled actin filaments prior to external stimulus. Therefore, the strain along the axis of the cell body caused by the displacement in the *x*-direction is:

$$\varepsilon_{xc} = \frac{N_0(1+\varepsilon_x cos\theta_x) - N_a}{N_a}. \tag{3.16}$$

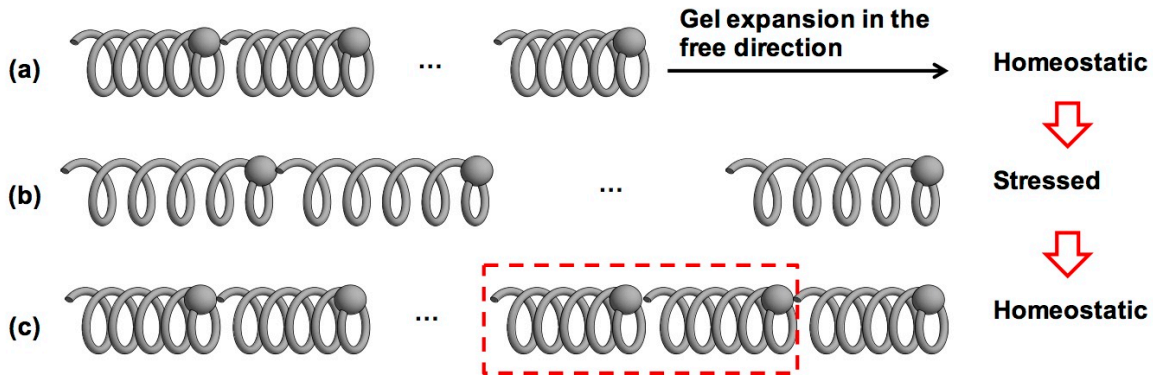

Figure 3.6 Actin filaments represented by individual springs connected in series to form a SF spring system. SF at homeostatic state (a) is elongated due to gel expansion. The tension caused by elongation of actin filaments (b) is relaxed with additional actin filaments assembled in the SF (c), then the homeostatic state is recovered.

Substituting Eq. 3.16 and $l = N_a l_a$ into Eq. 3.14 yields

$$E = N_a e_0 + \frac{k_a}{2N_a} {N_a}^2 {l_a}^2 \left\{ \left[\left(\frac{N_0(1+\varepsilon_x cos\theta_x) - N_a}{N_a} \right) - \frac{\sigma_y cos\theta_y N_a}{k_a} - \frac{\sigma_z cos\theta_z N_a}{k_a} \right]^2 - {\varepsilon_0}^2 \right\} + N_a\mu_a + N_f\mu_f + E_s. \quad (3.17)$$

For convenience, we define $F(N_a) = \left(\frac{N_0(1+\varepsilon_x cos\theta_x) - N_a}{N_a} \right) - \frac{\sigma_y cos\theta_y N_a}{k_a} - \frac{\sigma_z cos\theta_z N_a}{k_a}$. Then Eq. 3.17 can be simplified as

$$E = N_a e_0 + \frac{k_a}{2N_a} {N_a}^2 {l_a}^2 [F^2(N_a) - {\varepsilon_0}^2] + N_a\mu_a + N_f\mu_f + E_s. \quad (3.18)$$

When E reaches a minimum, the derivative of E with respect to N_a is zero:

$$\frac{dE}{dN_a} = \frac{k_a}{2} {l_a}^2 \{F(N_a)[2N_a F'(N_a) + F(N_a)] - {\varepsilon_0}^2\} + \left(e_0 + \mu_a - \mu_f + e_s\right) = 0. \quad (3.19)$$

In Eq. 3.13, we have already shown that $e_0 + \mu_a - \mu_f + e_s = 0$. As such,

$$\frac{dE}{dN_a} = \frac{k_a}{2} {l_a}^2 \{F(N_a)[2N_a F'(N_a) + F(N_a)] - {\varepsilon_0}^2\} = 0. \quad (3.20)$$

For sufficiently small homeostatic strain ε_0, we neglect ε_0 in Eq. 3.20, which leads to $\frac{k_a}{2} {l_a}^2 F(N_a)[2N_a F'(N_a) + F(N_a)] = 0$. The term $2N_a F'(N_a) + F(N_a)$ can be further expanded as

$$2N_a F'(N_a) + F(N_a) = -\frac{N_0(1+\varepsilon_x cos\theta_x)}{N_a} - 1 - \frac{3\sigma_y cos\theta_y N_a}{k_a} - \frac{3\sigma_z cos\theta_z N_a}{k_a}. \quad (3.21)$$

Since $cos^2\theta_x + cos^2\theta_y + cos^2\theta_z = 1$, $0 \le cos\theta_x \le 1$, $0 \le cos\theta_y \le 1$, $0 \le cos\theta_z \le 1$ and all the rest parameters are positive, Eq. 3.21 is always smaller than zero. Then to satisfy Eq. 20, $F(N_a)$ has to be zero.

$$F(N_a) = \left(\frac{N_0(1+\varepsilon_x cos\theta_x) - N_a}{N_a} \right) - \frac{\sigma_y cos\theta_y N_a}{k_a} - \frac{\sigma_z cos\theta_z N_a}{k_a} = 0. \quad (3.22)$$

According to the assumption that the strain along the long axis of the cell body caused by the displacement in the x-direction is released by the additional assembly of actin filaments, the first term $[N_0(1+\varepsilon_x cos\theta_x)-N_a]/N_a$ in Eq. 3.22 is zero at equilibrium.

Therefore,

$$cos\theta_y = cos\theta_z = 0,$$

$$cos\theta_x = \sqrt{1-cos^2\theta_y - cos^2\theta_z} = 1, \tag{3.23}$$

$$N_a = N_0(1+\varepsilon_x).$$

Under this condition, $\theta_x = 0°$, $\theta_y = \theta_z = 90°$. This means that cells are aligned to the *x*-direction and perpendicular to the *y*- and *z*- directions to achieve a minimum energy state. In this way, the homeostatic level of force is re-established.

On the other hand, for cells with large inherent stress, ε_0 cannot be neglected in Eq. 3.20, so $F(N_a)[2N_aF'(N_a)+F(N_a)]-{\varepsilon_0}^2=0$. This can be expanded as:

$$\left(-\frac{\sigma_y cos\theta_y N_a}{k_a}-\frac{\sigma_z cos\theta_z N_a}{k_a}\right)\left(-\frac{N_0(1+\varepsilon_x cos\theta_x)}{N_a}-1-\frac{3\sigma_y cos\theta_y N_a}{k_a}-\frac{3\sigma_z cos\theta_z N_a}{k_a}\right)={\varepsilon_0}^2. \tag{3.24}$$

Along with $cos^2\theta_x + cos^2\theta_y + cos^2\theta_z = 1$, there are three unknowns,θ_x, θ_y and θ_z and only two equations. Therefore, no specific combination of angle θ_x, θ_y and θ_z can be obtained and many combinations of θ_x, θ_y and θ_z can satisfy these two equations. This renders a random cell orientation distribution.

II. Laterally Unconfined Condition

Next, we extend the model to the laterally unconfined condition. In this case, cells are free to extend in both *x*- and *y*- directions.

Based on Eq. 3.1-3.3, the strains of the gel in the *x*- and *y*- directions are equal:

$$\varepsilon_x = \varepsilon_y. \tag{3.25}$$

Then, for cells with low inherent ε_0, Eq. 3.22 becomes

$$F(N_a) = \frac{N_0(1+\varepsilon_x cos\theta_x)-N_a}{N_a} + \frac{N_0(1+\varepsilon_y cos\theta_y)-N_a}{N_a} - \frac{\sigma_z cos\theta_z N_a}{k_a} = 0, \tag{3.26}$$

which leads to,

$$\begin{gathered} cos\,\theta_z = 0, \\ \varepsilon_x cos\theta_x = \varepsilon_y cos\theta_y \rightarrow cos\theta_x = cos\theta_y = \sqrt{\frac{1-cos^2\theta_z}{2}} = \frac{\sqrt{2}}{2}. \end{gathered} \tag{3.27}$$

Hence, $\theta_x = \theta_y = 45°,$ and $\theta_z = 90°$, indicating that cells are aligned diagonally with the *x*- and *y*- directions and perpendicular to the *z*-direction.

For cells with large inherent ε_0 such as CAFs, Eq. 3.24 becomes

$$\left(-\frac{\boldsymbol{\sigma}_z cos\theta_z N_a}{k_a}\right)\left(-\frac{N_0(1+\varepsilon_x cos\theta_x)}{N_a} - 1 - \frac{N_0(1+\varepsilon_y cos\theta_y)}{N_a} - 1 - \frac{3\sigma_z cos\theta_z N_a}{k_a}\right) = {\varepsilon_0}^2. \tag{3.28}$$

Again, no specific combination of angle θ_x, θ_y and θ_z can be obtained and cells can align in many directions but still satisfy the minimum energy principle.

3.5 Discussion

To date, most investigations on the effects of mechanical stimuli on cell reorientation have been done by cyclically stretching cells laying on 2D deformable substrates such as an elastic silicone membrane or polyacrylamide gel thin layer[41–45]. In these studies, cells reorient themselves away from (i.e., perpendicular to) the stretch direction where the membrane

deformation is the least and thus is most energetically favorable. However, this "stretch-avoidance" or "strain-avoidance" phenomenon does not occur when cells are embedded in a 3D matrix. Reported results have shown that fibroblasts in a 3D matrix align themselves along the axis of tensile force in response to stretching[54,152,153] and away from the axis of compressive force in response to compression[65]. Even though various hypotheses have been proposed to account for the difference between the 2D and 3D cases[64,170], it is still not clear why cells do not show "stretch-avoidance" or "strain-avoidance" in 3D.

In our studies, the seemingly different response for cells in 3D matrices is in fact consistent with their behavior in 2D, i.e., both follow minimum energy principle with cells realigning themselves to achieve minimum energy. Cells in a 3D matrix encounter complex tensile and compressive forces from three different directions simultaneously; thus, "stretch-avoidance" or "strain-avoidance" in 2D models, which is equivalent to energy minimization is not directly applicable in a 3D environment. The present study found that cells such as NAFs in 3D prefer to align in the free/stretching direction (note that in our experiment, the free direction is passively stretched due to the elasticity of the gel) and avoid the compressive direction. This is likely because cells can reorient the axis of cell bodies to the free/stretching direction and release tension through remodeling SFs via actin filament assembly. However, the compressive stress cannot be released by shortening SFs since SF shortening is prevented in normal living cells[143]. Therefore, cells such as NAFs possess lower energy when they align with the free/stretching direction. This could explain why cells embedded in a 3D matrix subjected to stretching or compression would realign themselves to the stretching direction. Moreover, with more cell-matrix interaction involved in 3D, inherent cell contractility could play an important and complex role. This leads to the observation that cells with a high inherent contractility exhibit

random distribution even though they have achieved minimum energy states through reorientation. Overall, our study suggests that even though the mechancially triggered cell reorientation in 3D can show more complex patterns, their behavior is still governed by the minimum energy principle.

To verify that the NAFs and CAFs in our studies are of very different contractility, we conducted a cell contractility assay by embedding NAFs and CAFs in collagen I gels and measured the reduction of the gels' diameter after 0 h, 4 h, 16 h, and 24 h's incubation (see Fig. 3.7(a, b)). The collagen gel containing CAFs exhibits significantly more contraction than its counterpart, indicating that CAFs generate much higher inherent contractile stress than NAFs.

In addition, we studied α-SMA expression, as an established CAF marker, in both NAFs and CAFs[171–173]. Elevated expression of the α-SMA isoform confers a high contractile activity[174]. As shown in Fig. 3.8 (a, b), CAFs used in this study express 5 times higher levels of α-SMA than NAFs, indicating higher cell contractility. As shown by our model, the difference in the inherent cell contractility leads to very different responses of NAFs and CAFs to compression. NAFs, with sufficiently small inherent strain (ε_0), aligned themselves along specific directions to achieve minimum energy, while CAFs, with large inherent contractility, adopt a random distribution because a plethora of orientations could meet the minimum energy requirement.

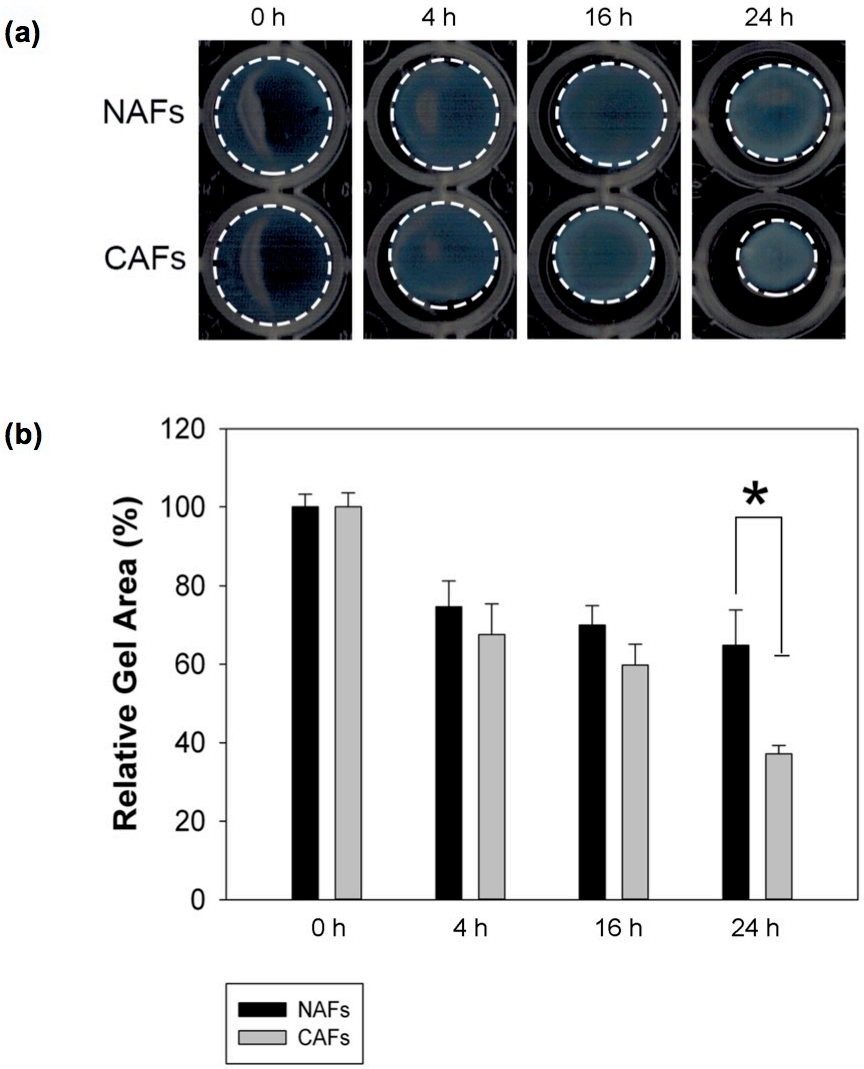

Fig. 3.7 CAFs exhibited much higher contractility than NAFs. (a) CAFs and NAFs were embedded in type I collagen gels, which were subsequently incubated for 24 h at 37°C to allow for contraction. Images of contracted gels with NAFs and CAFs were taken after 0 h, 4 h, 16 h, and 24 h. The gel circumferences are outlined with dashed white lines. (b) At the end of the contraction assay, the area of the gels was measured and expressed as a percentage of the original gel area before contraction. Error bars represent s.e.m. from N=3 independent experiments. A significant difference in relative gel area appeared 24 h after beginning the incubation, *P<0.005.

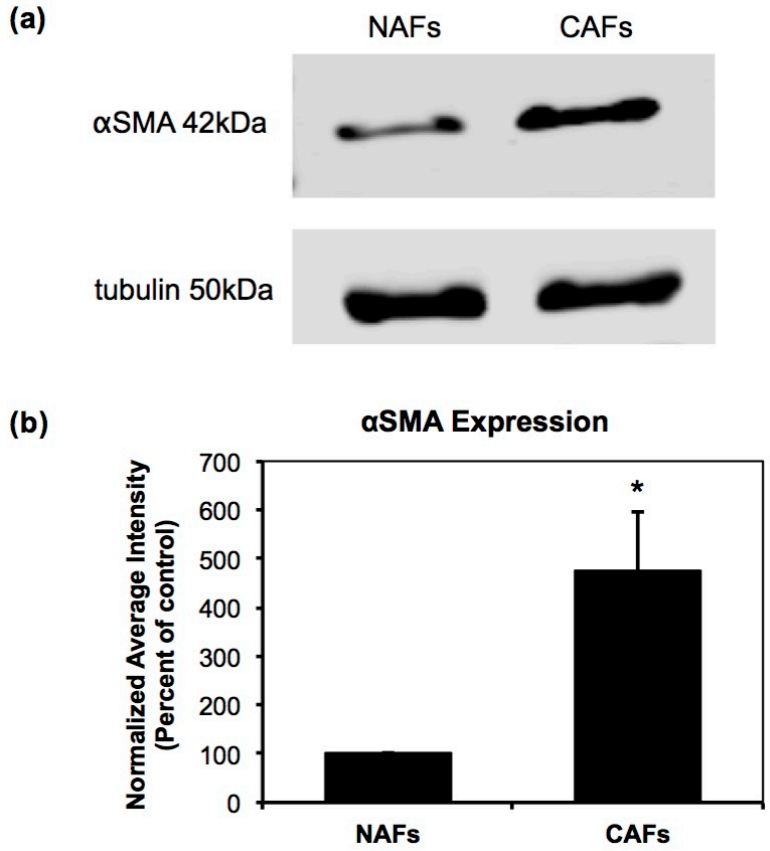

Fig. 3.8 Western blot analysis of α-SMA. (a) Western blot band image shows higher α-SMA expression in CAFs than in NAFs. (b) α-SMA band intensity was normalized by tubulin loading control. Normalized average intensity plot indicates a significant difference in α-SMA expression between NAFs and CAFs, *P<0.005, N=4.

To further confirm that cell contractility is the deterministic factor leading to the different orientation patterns between NAFs and CAFs, we stimulated NAFs with TGF-β and subjected them to compression. Cells treated with TGF-β have been previously shown to possess increased cell contractility[175–177]. Our results show that TGF-β treated NAFs do not realign towards the free direction in the lateral confined condition (see Fig. 3.9 (a)~(c)), but present a random distribution. The observation that TGF-β treated NAFs exhibit distinct reorientation patterns from untreated NAFs provides further evidence of cell contractility being a major factor in

promoting the observed differences in NAFs and CAFs' response to a compressed 3D environment.

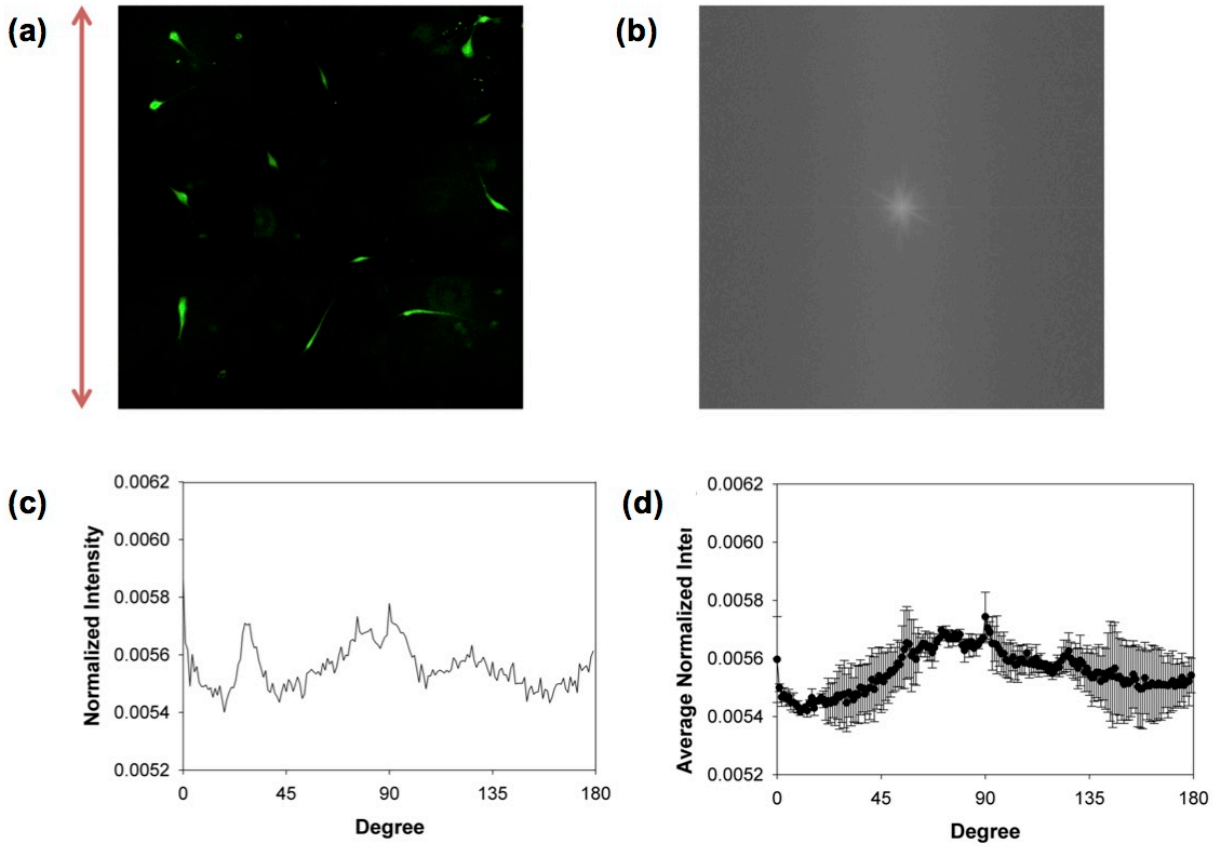

Fig. 3.9 NAFs with increased cellular contractility induced by TGF-β exposed to laterally confined compression. (a) Montages of fluorescence images of NAFs after overnight compression. (b) FFT output images of NAFs. (c) Normalized radial summation of pixel intensities over a circle projection of FFT images of NAFs. (d) The average normalized pixel intensity of NAFs from three independent experiments. The red arrows show the free direction.

While the developed model in this work includes biomechanical contributions, such as cell contractility, SF assembly, and chemical potentials, it does not include the dynamic contribution of biochemical signaling. For example, the small GTPases RhoA, Rac1 and Cdc42 are reported to be central regulators of actin dynamics[178], and the MAPK family including JNK, ERK and p38[169] have been found to be activated in cells cultured on a substrate that has been

cyclically stretched. Although it is known that cells are able to coordinate mechanical responses and biological signaling when subjected to mechanical stimuli, this process involves a large number of proteins and signaling activities, many of which are still not fully understood. As such, the theoretical model here, built upon a pure thermodynamic consideration of the minimum energy principle, still needs further verification. However, the fact that the model successfully predicted the cell reorientation under different conditions suggests that it considers the essential factors directly determining the equilibrium states achieved through cellular response to the external stimuli. We would like to point out that in our model, we focus on the effects of SFs, which is consistent with the understanding that they are the main contractile cytoskeletal machinery that play a key role in regulating cell orientation[36,42,141,147,149–151,164,165,169,178,179].

It is worth noting that a linear elasticity assumption was employed in this model; however, in the real compression scenario, both the collagen gel and SFs exhibit viscoelastic properties[151]. We believe that even with this simplification, the model still provides a meaningful explanation of the experimental observations because the model was developed on the basis of equilibrium states rather than dynamic adaptation. Viscous effects are eliminated at equilibrium. For example, if we consider the collagen gel as a viscoelastic material, using the Kelvin model[180] the relationship between stress and strain is given by

$$\varepsilon(t) = \frac{\sigma_0}{E}\left(1 - e^{-(E/\eta)t}\right), \tag{3.29}$$

where η is the viscosity describing the viscous behavior of the material. However, in this study, time t is large enough (static) so that the equation goes back to a linear relationship $\varepsilon(t) = \frac{\sigma_0}{E}$. As such, the assumption of linear elasticity is reasonable in this thermodynamics-based model. It

is worth noting that according to Roeder et al.[163], the applied 30% strain lies in the linear elastic region of collagen gel at a concentration of 2 mg/ml.

Another assumption employed in the model is that SFs are oriented parallel to the long axis of the elongated cell body. In reality, SF distributions within individual cells can vary. For example, endothelial cells can have a large variety of the SF orientations. However, for highly elongated cells such as fibroblasts and smooth muscle cells, SFs tend to be oriented in parallel[147]. For example, SFs in REF-52 fibroblasts exhibited perfect alignment with the polarity of the cell body[43]. Additional evidence such as the fluorescence images of SFs in MC3T3-E1 osteoblast cells, which show highly aligned SFs along the long axis of the cell body[181], is also reported. Therefore, we believe that it is reasonable to assume that SFs are distributed along the polarized direction of the fibroblasts.

One more factor that has not been discussed is the effect of the shear force near the wall. The fluorescence images were obtained at locations away from the boundaries throughout the sample to ensure that the shear forces caused by any boundary effects were marginal. It has been reported that shear strain is negligible compared to normal strains in the central region of a 3D gel matrix[152]. This finding supports our normal-force based model.

We would like to re-emphasize the important role of boundary conditions in this study. The cell reorientation is a result of combined z-direction compression and stretch along the x-direction for the laterally confined case and along both the x- and y-diections for the laterally unconfined case. In our work, the gel was made into square. As such, in the laterally-unconfined case, the gel only expands freely along the two lateral axes, i.e., the x- and y-directions in the model. This boundary condition has been taken into account in the model by simply setting a

square gel in a Cartesian coordinate system with the two axes of the gel parallel to the *x*- and *y*-directions, and only allowing the gel to expand freely in these two directions. In fact, we also observed that if there is no boundary constrain, i.e., in a circular gel, NAFs only respond to the compression by realigning perpendicular to the *z*-direction but without a preferred orientation in the *x*-*y* plane. This is consistent with the understanding that cell orientation is always dependent on both the loading and the boundary conditions[43].

It should also be noted that, static and cyclic loading are both biologically relavent. For example, CAFs experience continuous compressive stress in the normal direction with a growing tumor[182]. In addition, in contrast to the fact that cyclic loading is a necessity for cell reorientation on a 2D substrate[41–45,139–141], it is not required to induce cell reorientation in 3D. For example, cells as well as SFs show realignment parallel to the direction of tensile strain in both static and cyclic strain cases in 3D[153]. Comprared to well-documented 2D studies, much less has been done for 3D case regardless of the force loading manner.

3.6 Summary

We experimentally studied the reorientation of human prostatic NAFs and CAFs embedded in 3D collagen I matrices and subjected to compression. NAFs realign themselves to specific directions while CAFs show a random distribution. A theoretical model indicates that the minimum energy principle can be used to account for the behavior of both NAFs and CAFs and the significant difference in the phenotype is due to their inherent cell contractility. The importance of cell contractility in cell reorientation is further confirmed by the fact TGF-β treated NAFs with enhanced contractile force behave in a similar manner as CAFs. This new understanding of the contribution of the cell mechanical properties to their reorientation upon

external mechanical stimuli in 3D has not been reported in the literature. Taken together, the experimental and theoretical studies presented here provide new insights into the mechanisms governing the behavior of cells in a mechanically stressed 3D environment.

CHAPTER IV

MICROFLUIDIC PLATFORMS WITH INTEGRATED GRAPHENE TRANSISTORS FOR PROBING THE ELELCTRICAL ACTIVITIES OF SINGLE SYNAPSES AND DENDRITIC SPINES

4.1 Motivation

In Chapter II and III, the conducted research on cell biomechanical activities has been discussed. This chapter will focus on detecting neuron electrical activity with ultrahigh spatiotemporal resolution. As discussed in session 1.4, tremendous attention and efforts of generations of scientists have been drawn to studies of neuron electrical signaling, owing to the vital functions and intricate features of neurons; however, the limitations of conventional technologies, such as electrophysiological patch-clamping and optical imaging approaches, in terms of throughput and spatiotemporal resolution, remain a big hurdle to understanding the molecular mechanisms that regulate the formation and plasticity of spines and synapses. In fact, dendritic spines could act very distinctively from their parent dendrites, providing an unknown mechanism for regulating synaptic strength at the single spine level[183]. Furthermore, it has been reported that individual spines and synapses can display unique properties and activities[184]. Therefore, new neurotechnologies with ultra-high spatiotemporal resolution and sensitivity, capable of probing the activity of individual spines and synapses, are in urgent need.

In this chapter, a microfluidic platform integrated with graphene optoelectronic probes that can locally measure the electrical activity of individual synapses in real-time is described. First, we present the device design, modification, and validation through experiments and COMSOL™ modeling. Next, we demonstrate that the platform is capable of detecting electrical activity at a

single synapse level using scanning photocurrent microscopy and confocal microscopy, indicating an ultra-high spatial resolution. More importantly, the electrical activity alteration upon different K^+ concentration of Hank's balanced salt solution (HBSS) was recorded. This novel neurotechnology demonstrates significant potential in terms of the ultrahigh spatiotemporal resolution, charge sensitivity, and throughput.

4.2 Material and Methods

4.2.1 Device Design and Characterization

The platform consists of two main parts: (1) the graphene transistor sensing component and (2) PDMS microfluidic component. The graphene transistor sensing component comprises 21 pairs of gold electrodes deposited and patterned on the top of a glass coverslip (No. 1, VWR Vista Vision, Suwanee, GA), and a 1 cm by 1 cm monolayer graphene laid on the top, forming 21 individual graphene transistors. Each transistor is composed of a pair of gold electrodes serving as source and drain with a separation of 20, 30, and 40 μm, and a graphene membrane in between. When a diffraction-limited laser spot scans over the graphene between each pair of electrodes, a photocurrent signal occurs wherever the graphene electronic band structure bends: the built-in electrical field separates the photo-excited electron and hole pairs, and thus produces a current (see Fig. 4.1 (a) and (b)). A local photocurrent signal induced by the local electrochemical potential change appears as two adjacent spots, one with a positive sign and the other with a negative sign (a pair of red and blue spots in Fig. 4.1 (b)).

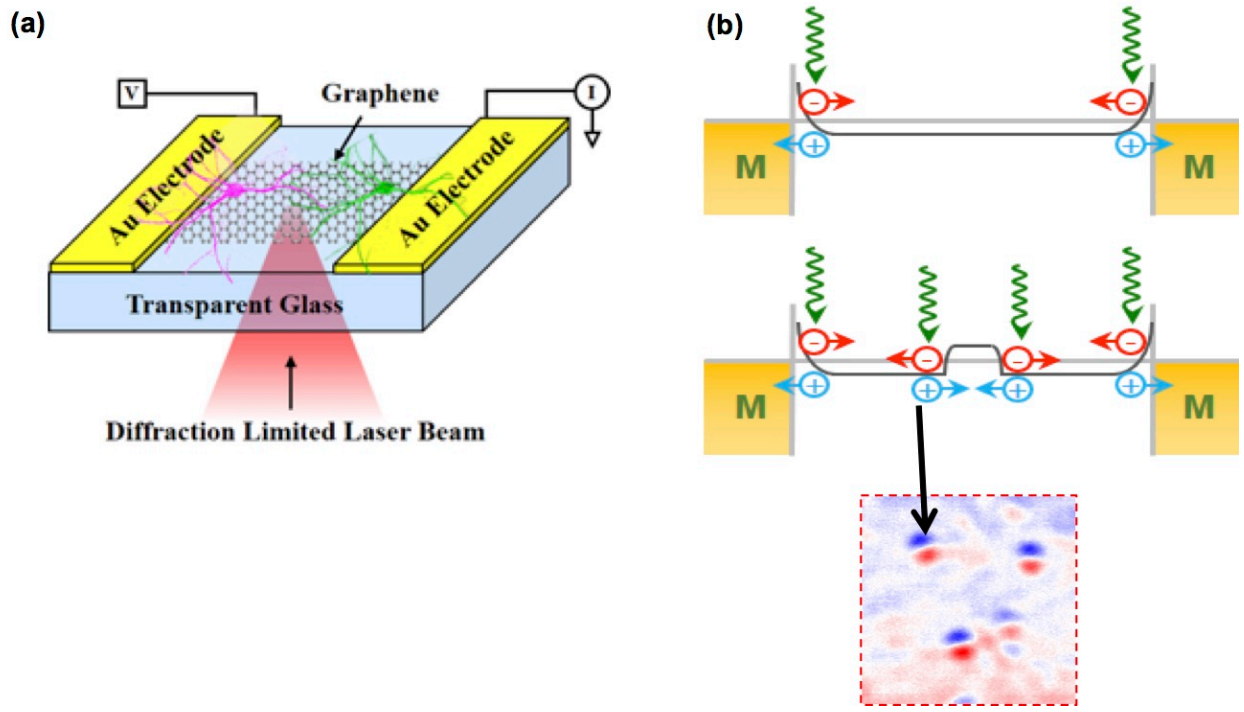

Figure 4.1 The working principle of graphene transistor based sensing. (a) A diffraction-limited laser spot scans over the graphene underneath neurons. (b) A local electrochemical potential change can shift the Fermi level of graphene, leading to a local photocurrent signal that appears as two adjacent spots in the zoom-in image, one with a positive sign and another with a negative sign (a pair of red and blue spots).

The PDMS microfluidic component is assembled on top of the graphene transistor, as shown in Fig. 4.2 (a) and (b), consisting of two layers, the bottom microchannel layer and the top pressure control chamber. The bottom layer is patterned with 4 cell-culture chambers (0.8 mm wide × 5.4 mm long × 100 µm tall), including two inner neuron culture chambers and two outer glia cell culture chambers, and 1 middle sensing channel (150 µm wide × 100 µm tall) where all graphene transistors are located. This four-chamber cell co-culture scheme has turned out to be a great success in primary cell culture *in vitro* as it greatly enhances the health of neurons, the number of synaptic contacts and the stability of formed synapses[100]. All chambers and the middle channel are connected through an array of microgrooves (50 µm wide × 75 µm long × 5 µm tall) that work as valves controlled by the top pressure chamber. The pressure chamber can be

pressurized hydraulically via the connected inlet/outlet tubing. When the valves are open, cells in different chambers can interact with each other, as shown in Fig. 4.3 (a). This connection provides two benefits: first, with on-chip co-culture of glial cells, it forms a more supportive microenvironment for neuron culture; secondly, neurons from the two chambers can extend their processes to the middle channel through the open grooves, communicate with each other and propagate information encoded in electrical signals on the top of the sensing component. The electrical activities can be measured by the sensing component in the form of photocurrent. The valves can also be closed to form separate compartments (see Fig. 4.3 (b)). In this case, groups of cells in different chambers can be treated separately. For example, two populations of neuron cells can be individually transfected with mCerulean and mCherry-Synnaptophysin so that the contact they make to form synapses can be visualized through the overlap of multiple colors. Also, chamber separation makes coating of Polylysine (PLL) at selected region possible. PLL coating, on one hand, is necessary for healthy neuron culture; on the other hand, it shields electrical signal transmission from neurons to the sensing component and thus fails the photocurrent formation. By activating the microgroove valves and only flowing PLL solution to cell culture chambers, we can achieve a PLL-free zone in the middle sensing channel and PLL-coated neuron culture chambers.

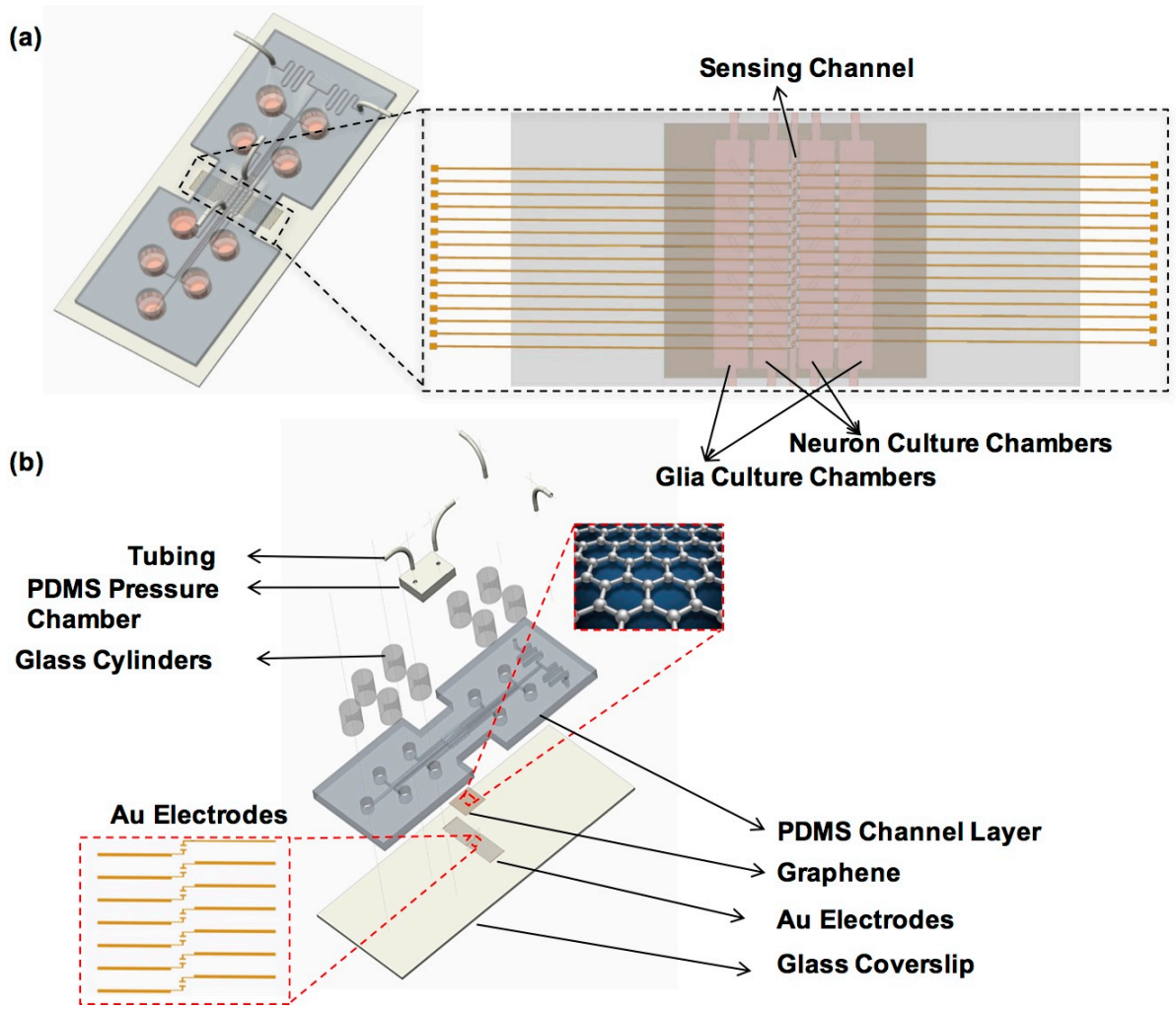

Figure 4.2 Schematics of a graphene transistor based microfluidic sensing platform. (a) A three-dimensional schematic of the assembled microfluidic platform and a zoom-in view of the electrodes and channels; (b) An exploded view of the platform.

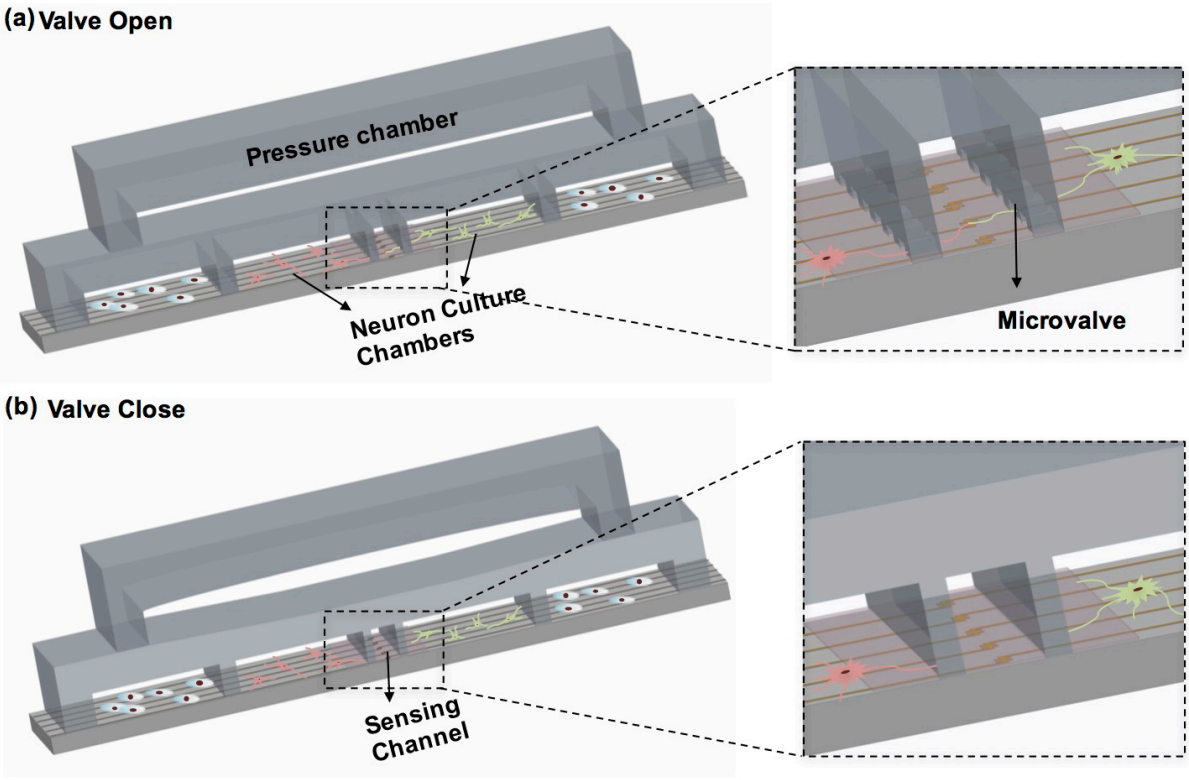

Figure 4.3 Schematics of microvalves. (a) When the valves are open, all chambers and the middle channel are connected and cells in different chambers can interact with each other. (b) When the valves are closed, all chambers and the middle channel are separated.

The middle channel branches out to two serpentine channels at the upstream of the platform that are connected to a seesaw chemical stimulant delivery system (see Fig. 4.4) via tubing. This system consists of a seesaw beam, a computer-controlled linear actuator, and two 5 ml syringe containing 4 mM and 90 mM K^+ concentration HBSS. By controlling the motion of the actuator, we are able to raise one solution up and drop the other one down cyclically, thereby switching the medium supply between 4 mM or 90 mM K^+ HBSS to the sensing area in the middle channel.

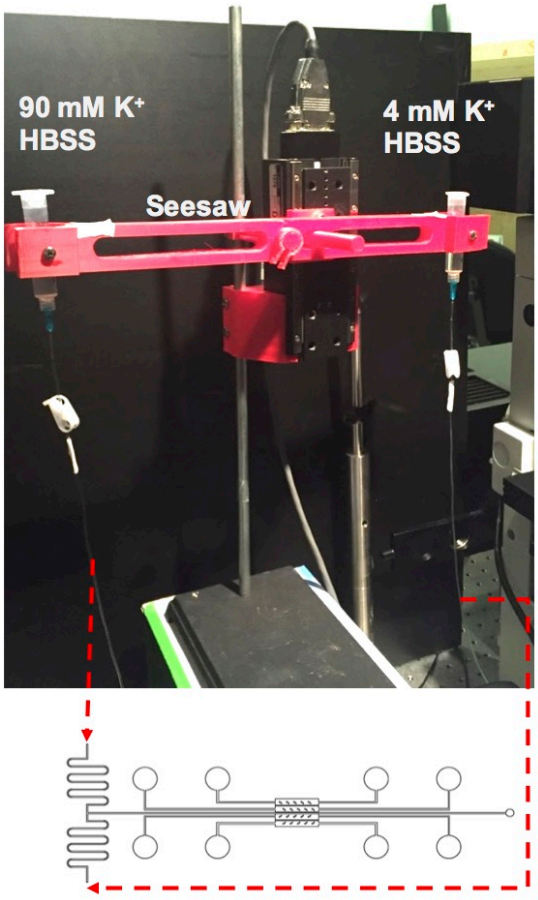

Figure 4.4 A photograph of the seesaw chemical stimulant delivery system. It is composed of a seesaw beam, a computer-controlled linear actuator, and two 5 ml syringe, alternatively providing 4 mM and 90 mM K^+ concentration HBSS to the device through the serpentine inlets by raising one solution up and drop the other one down.

The current serpentine channel design was evolved from two straight branch channels as shown in Fig. 4.5 (a). The issue with the previous design is that the fluidic resistance of the straight branch is significantly smaller than that of the middle channel, and hence the media from one branch will directly flow to the other branch instead of entering the middle channel (see Fig. 4.5 (b)). On the contrary, the serpentine structure was delicately designed to exert appropriate fluidic resistance and to achieve: (1) the medium from the high-pressure branch can be delivered to the middle sensing area; (2) the medium flow from the low-pressure branch can be cut off in

the serpentine channel. The cut-off interface should not occur right at the junction as two solutions may co-exist in the downstream middle channel; and it should not be pushed back too far either, because this will slow down the switch between the two media.

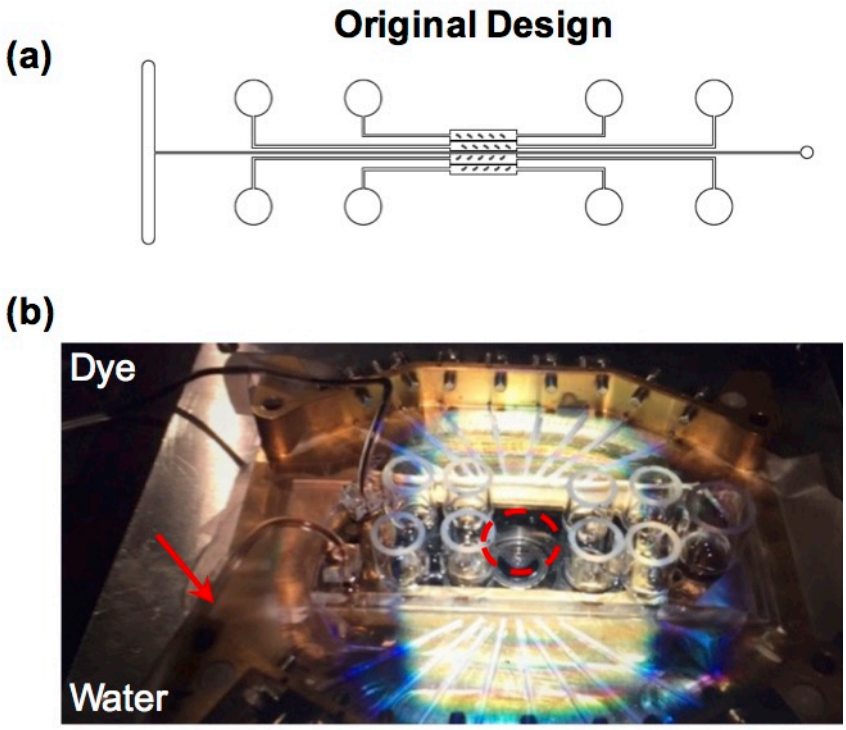

Figure 4.5 The original design with straight inlet channels. (a) The schematic of the original design. (b) In the flow test, dye and water were delivered to the middle-sensing channel via a seesaw system. After the dye was raised up, it directly flew out from the water branch instead of entering the middle channel. The red arrow denotes that the dye has entered the water tubing. The red dash circle shows no dye observed in the chamber and channel area.

To achieve the aforementioned two goals, a serpentine T-shape inlet based on a fluidic resistance analysis was implemented. We simplified two inlet branches and the middle channel as fluidic resistors, R_1, R_2, and R_3 and analyzed fluidic resistances represented by a schematic fluidic circuit in Fig. 4.6.

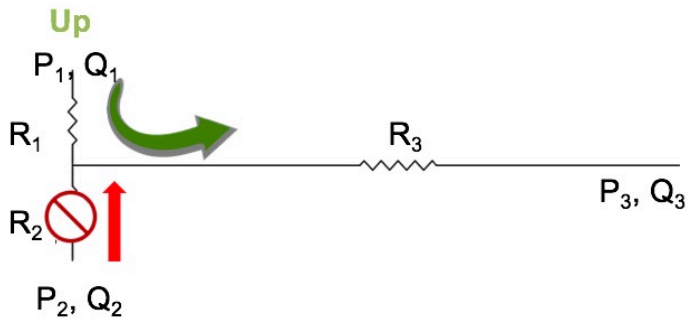

Figure 4.6 Fluidic resistance network of a serpentine T-shape branch device. P_1, P_2, and P_3 are relative pressure heads at the two inlets and the outlet; Q_1, Q_2, and Q_3 are the flow rates at each channel. Solution 1 is raised up and designed to be delivered to the middle channel. Solution 2 with lower pressure head is designed to stop at its branch.

Here we lay out the formulations:

$$Q_3 = Q_1 + Q_2, \tag{4.1}$$

$$P_2 - P_3 = R_2 Q_2 + R_3 Q_3, \tag{4.2}$$

$$P_1 - P_3 = R_1 Q_1 + R_3 Q_3. \tag{4.3}$$

Here P_1, P_2, and P_3 are relative pressure heads at the two serpentine branch inlets and the outlet of the middle channel; Q_1, Q_2, and Q_3 are flow rates at each channel. If the solution at location 1 is raised up, solution 2 needed to be stopped moving forward, therefore

$$Q_2 = \frac{2[-R_3 P_1 + (R_1 + R_3)P_2]}{(R_1 + R_2)(R_2 + 2R_3)} \leq 0. \tag{4.4}$$

Eq. 4.4 can be simplified as

$$\frac{R_1 P_2}{R_3(P_1 - P_2)} \leq 1. \tag{4.5}$$

As for rectangular channels, $R_h = \frac{12\mu L}{wh^3\left(1-0.63\frac{h}{w}\right)}$. Here, h is the height of the channel, while L and w are the length and width of the channel, respectively, and $h < w$.

Since $w_1 = w_3,\ h_1 = h_3, P_i = \rho g H_i$, Eq. 4.5 gives

$$\frac{R_1 P_2}{R_3(P_1 - P_2)} = \frac{L_1}{L_3}\frac{H_2}{H_1 - H_2} \leq 1, \tag{4.6}$$

where H_i is the height of the solution i relative to the height of the outlet, $i = 1, 2$.

Define $\alpha = \frac{H_1 - H_2}{H_2}$, Eq. 4.6 can be simplified as

$$\frac{L_1}{\alpha L_3} \leq 1. \tag{4.7}$$

In addition, Q_2 needs to be cut off by Q_1 in the branch where solution 2 resides; and therefore

$$L_1 \leq \alpha L_3 < L_1 + L_2 \tag{4.8}$$

Because of the symmetry, $L_1 = L_2$, Eq. 4.8 gives

$$L_1 \leq \alpha L_3 < 2L_1. \tag{4.9}$$

By adjusting L_1 and α, more specifically, the length of serpentine branch and the height of the two solutions, a desired flow can be achieved. Following this guideline, the design was modified as shown in Fig. 4.7 (a) and then tested by raising up the dye solution and dropping down the water side through the seesaw solution delivery system. Fig. 4.7 (b) illustrates that the dye solution successfully flew to the middle channel (in dark color) and cut off water in the other branch (in clear color). This is further confirmed through COMSOL™ modeling. Two modules, laminar flow and transport of diluted species, were applied to a 3D model and generated the

static concentration and flow fields, as shown in Fig. 4.7 (c) and Fig. 4.8. The solution in red simulates the solution with high pressure head and 90 mM K^+ concentration, while the blue solution represents the drop-down solution with a K^+ concentration of 4 mM. Both concentration and flow fields in Fig. 4.7 (c) and Fig. 4.8 show that under the current geometry, fluidic resistance, and pressure head difference, the solution with higher pressure head takes up the middle sensing channel and cuts off the other solution in its branch. This is consistent with the experimental test results with dye and water. As such, the modified design satisfies the flow requirements.

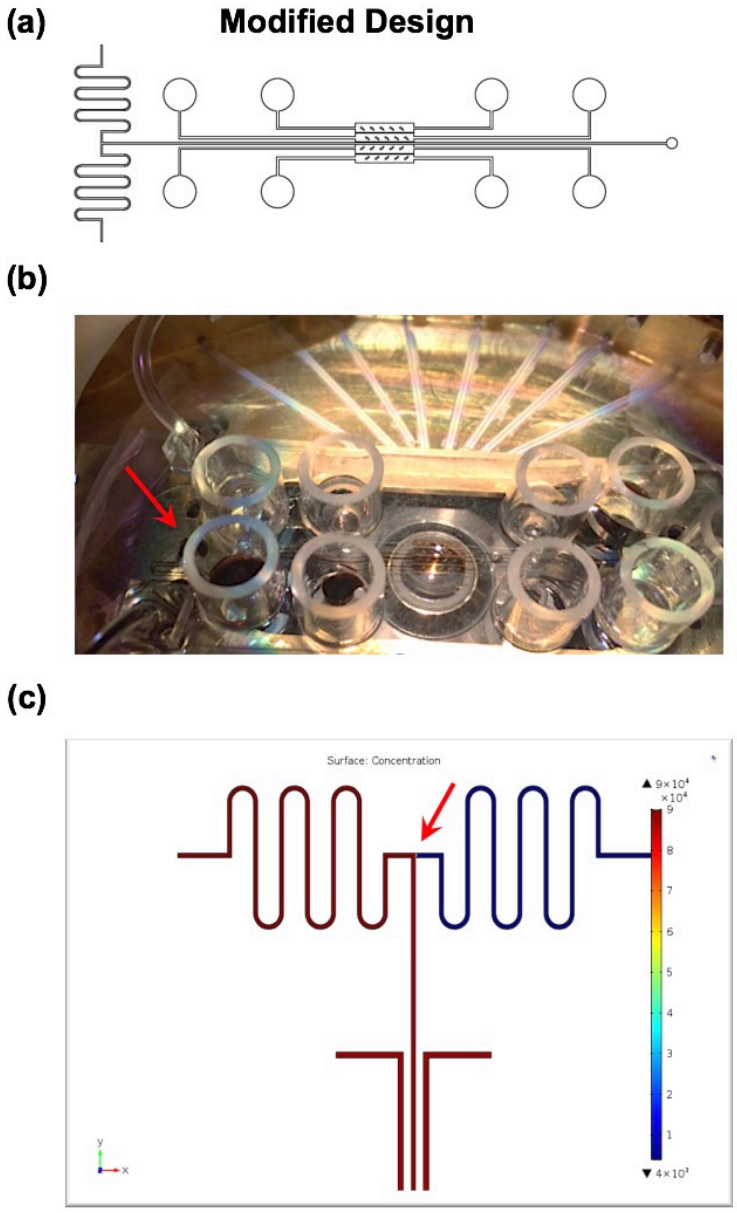

Figure 4.7 Design modification and validation. (a) Schematic of the modified design. (b) Experimental validation. We tested the new design by raising up the dye solution and dropping down the water side through the seesaw solution delivery system. It has been observed that the dye solution successfully flew into the middle channel (in dark color) and cut off water in the other branch (in clear color). (c) COMSOL^{TM} modeling validation. The concentration distribution shows that the red solution, with higher inlet pressure, takes up the middle sensing channel and cuts off the blue solution in its branch.

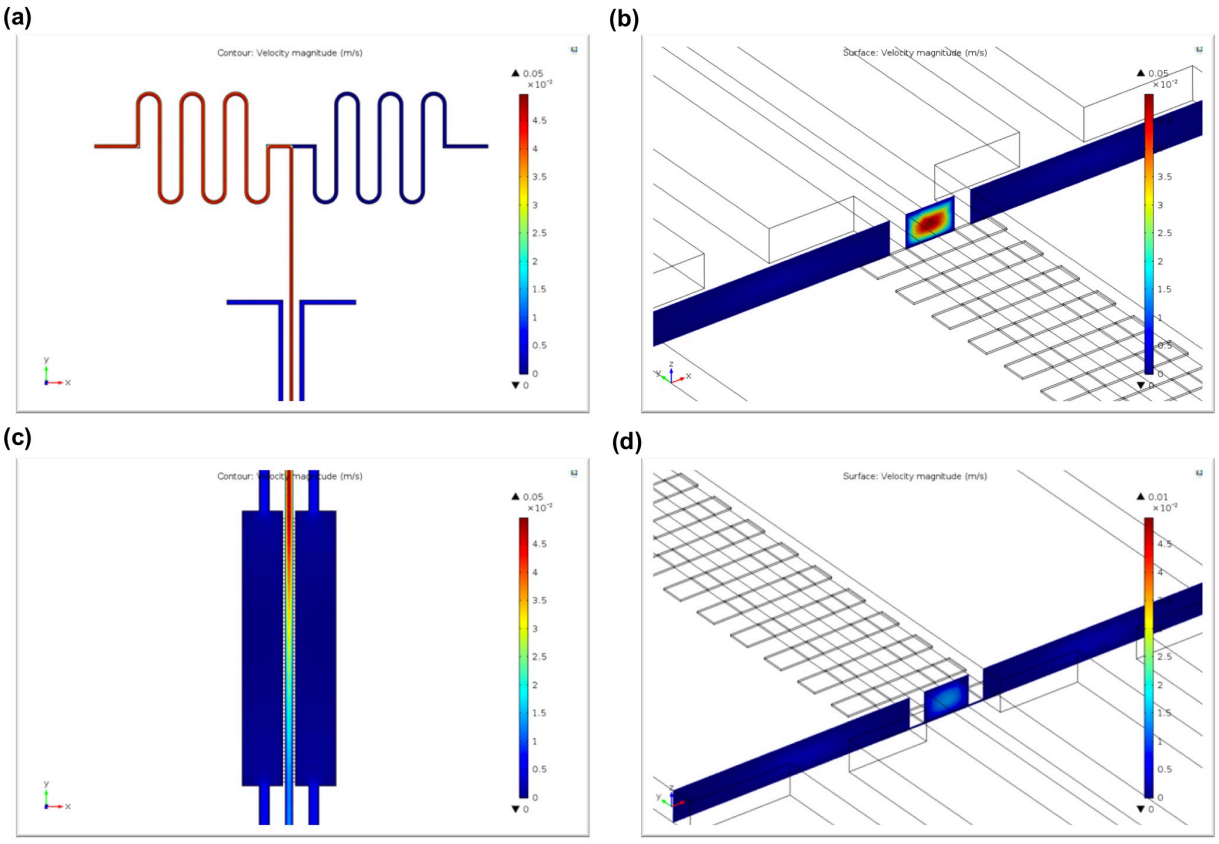

Figure 4.8 COMSOL™ modeling on flow velocity. The flow velocity distribution shows the solution with higher pressure head (entering from the left serpentine inlet) possesses a speed up to $5\times10^{-4}\ m/s$ and takes up the middle sensing channel. Meanwhile, the other solution (enter from the right serpentine inlet) is cut off and stopped in its branch.

4.2.2 Fabrication

The device was fabricated in 3 main steps: (1) microelectrode pattern and graphene synthesis and transfer, (2) PDMS microfluidic channel construction, and (3) assembly of the fabricated components and other auxiliary elements. Graphene was grown on a cooper substrate through chemical vapor deposition (CVD) technique[185]. Briefly, copper foils (Alfa Aesar 0.025 mm, 99.8% pure, annealed, uncoated) with a grain size of ~100 µm were cut into strips of 1 cm in width and then rinsed with 5% nitric acid (5 min) to eliminate contamination. We then loaded

the copper foils onto a quartz boat, and further transferred them to a horizontal furnace system. After the system was pumped down to 10 mTorr, the copper foil was annealed at 980°C with 100 sccm hydrogen flowing through the tube for 1 h. A mixed gas of 100 sccm H_2 and 20 sccm CH_4 was then introduced into the furnace for the growth of graphene at 980°C for 30 min. Then the graphene-copper was coated with a thin transfer layer of polymethyl methacrylate (PMMA) and underwent a wet etching process to remove the copper foil. The copper etchant was replaced by DI water to clean up etchant residual from the graphene. Next, the PMMA-graphene film were scooped by a glass coverslip on which electrode arrays were pre-patterned following a standard photolithography and e-beam evaporation method[186]. Finally, to remove PMMA and clean the transistors on the coverslip, acetone (overnight), isopropyl alcohol (IPA, 10 min), and DI water were sequentially used.

The microfluidic component was fabricated using a standard soft lithography technique[32,159,187,188] as mentioned in Chapter II. Inlet and outlet accesses of 3 mm in diameter were punched through the PDMS layer to facilitate cell/media loading and removal. Inlet tubing openings of 1 mm in diameter were also punched for the access of HBSS. After being plasma treated, PDMS bottom and upper layers as well as tubing supporters that help fixate the tubing were bonded together. Windows were cut off the bottom layer to allow electrode-contacting pads on the device to be bonded to a device holder.

The mold used to transfer the microchannel pattern to the PDMS pieces was fabricated through the standard photolithography. It normally yields a patterned photoresist, SU8, with rectangular cross section, which generates a PDMS microchannel with straight walls during the molding process. This configuration compromises the micro-valve performance because when the micro-valve is activated, it deforms onto the substrate and inevitably leaves two open

corners. This failed sealing cannot be adequately addressed with different aspect ratios and groove periodicity. Further, by tuning the PDMS preploymer/curing agent ratio or the PDMS thickness, the system stiffness was adjusted to a lower value in order to form a better seal. However, it resulted in a higher chance of wall buckling upon compression when the valve was pushed down, which could damage the graphene film (see Fig. 4.9). Finally, this issue was solved by changing the cross section of the microgroove to a trapezoidal shape, which successfully prevent the leakage caused by two open corners in the straight wall grooves, as shown in Fig. 4.10. In this validation test, fluorescent dye was flowed to the two cell chambers when the valves were closed. Time-lapse images on the middle channel area were taken for a time period of 12 h. The dye was then found to be leaked to the middle channel for the straight-wall device (Fig. 4.10 (d)), while this did not happen in the tapered-wall device, indicating a perfect sealing over a long-time period.

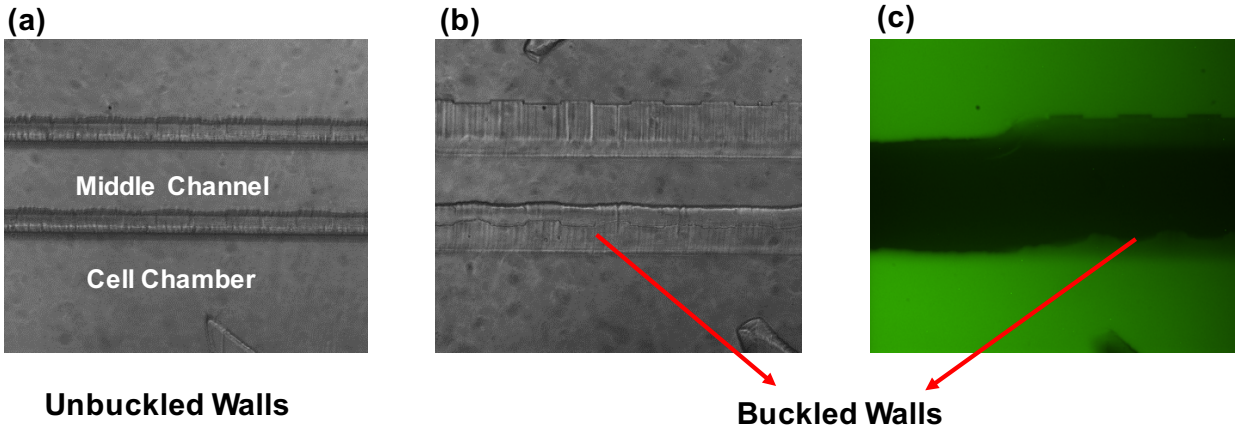

Figure 4.9 Images of unbuckled and buckled walls. (a) No wall buckling occurs in a regular device. (b, c) DIC and fluorescent images of wall buckling when the system stiffness is reduced.

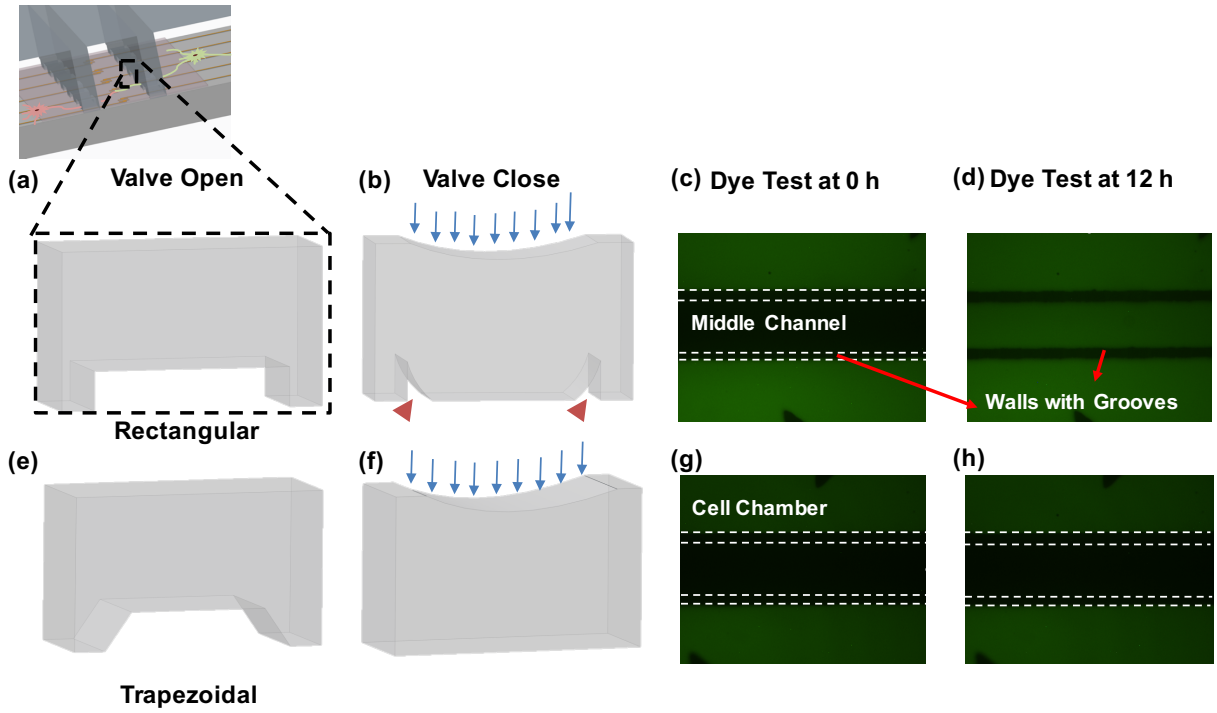

Figure 4.10 Comparison of different cross-sectional configurations of microgrooves in terms of valve performance. (a) The schematic of a microgroove with rectangular cross section. (b) The rectangular microgroove leaves two open corners when it is activated. (c, d) Overnight (12 h) test demonstrated a dye leakage into middle channel. (e) The schematic of a microgroove with trapezoidal cross section. (f) The trapezoidal microgroove yields perfect seal when it is activated. (g, h) Overnight (12 h) test demonstrated no dye leakage into middle channel.

The trapezoidal cross section was formed according to the following fabrication procedure:

(1) Prepare a 100 Si wafer with 20,000 Å thermally grown oxide and clean the wafer with acetone and IPA, and then bake the wafer at 200℃ (see Fig. 4.11 (a)).

(2) Spin coat photoresist SPR 220-3.0 at 500 RPM for 10 sec and 4500 RPM for 30 sec. Soft bake the wafer at 115℃ for 90 sec and cool it down at room temperature for 2 min (see Fig. 4.11 (b)).

(3) Pattern the photoresist by exposing the mask-covered wafer to UV light in a dose of 70,000 mJ/cm^2 via a Novacure 2100 system, followed by rehydrating the wafer at room temperature for 10 min. Then develop the photoresist for 50 sec. Rinse the wafer with DI water and blow dry with Nitrogen. Hard bake the wafer for 50 min (see Fig. 4.11 (c)).

(4) Etch the SiO_2 that is not protected by the photoresist using Buffered Oxide Etchant (BOE) for around 30 min given the total SiO_2 thickness of 20,000 Å and an etching rate of ~700 Å/min at room temperature. After the exposed SiO_2 is completely etched, rinse the wafer with DI water for 5 min, and dry it with nitrogen. Rinse the wafer with acetone and DI water to remove the photoresist, then blow dry (see Fig. 4.11 (d)).

(5) Etch the exposed Si using 30% by weight KOH in a water bath of 80℃ for 5 min given that the etching rate for 30% KOH at 80℃ is around 1 μm/min. Rinse the wafer with DI water and blow dry (see Fig. 4.11 (e)).

(6) Repeat step (4) and remove the rest of SiO_2 (see Fig. 4.11 (f)).

The above procedure yields an array of 5 um tall tapered trenches on the Si substrate, forming the first layer of the mold. Then standard photolithography was used to generate patterned microchannels. By pouring PDMS over the mold and peeling it off after it is cured, we managed to construct PDMS layers with microgrooves possessing trapezoidal cross section.

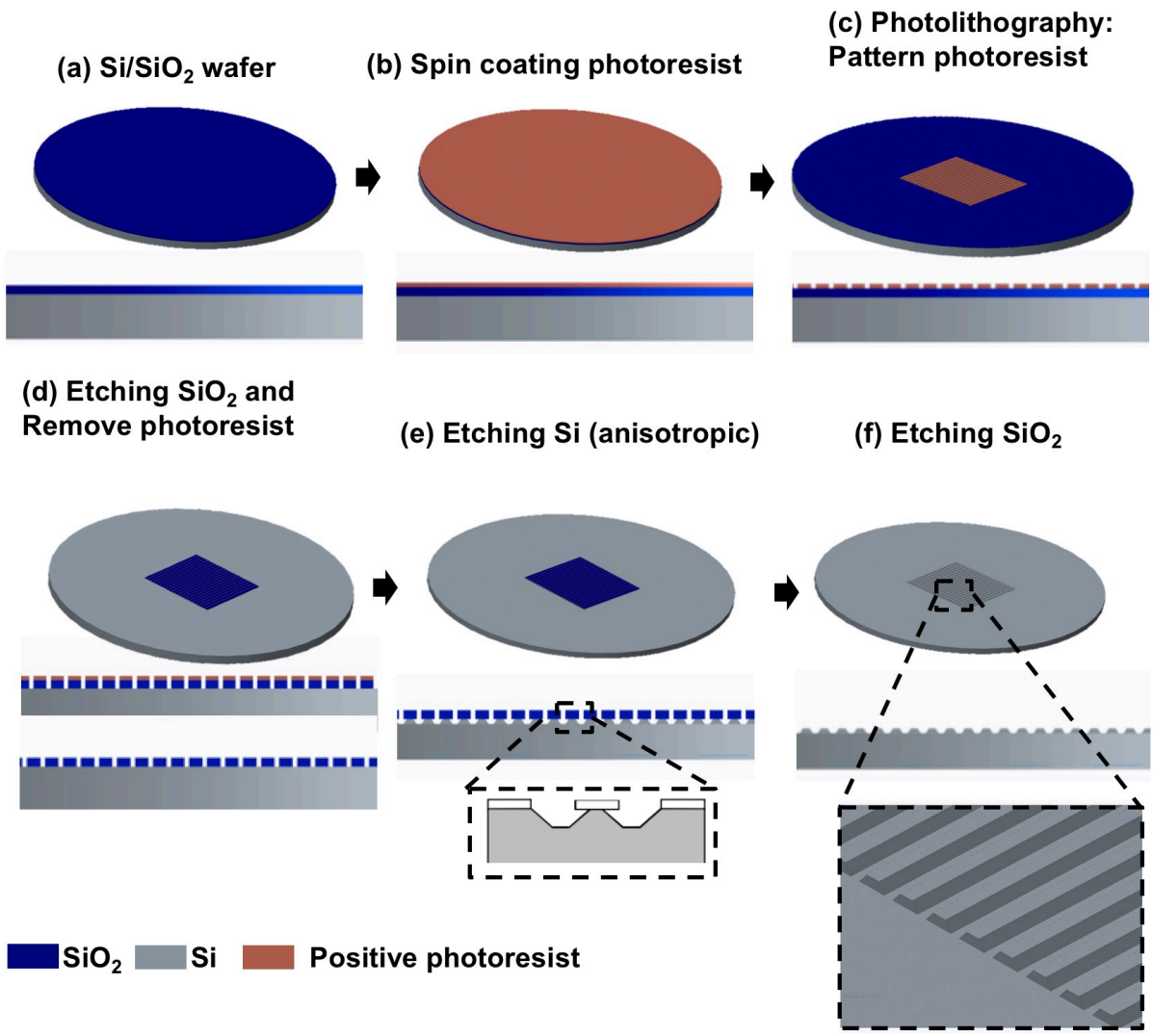

Figure 4.11 Schematic of the fabrication procedure of the master mold patterned for trenches with trapezoidal cross section. (a) Prepare a Si/SiO_2 wafer. (b) Spin coat photoresist. (c) Pattern photoresist. (d) Etch exposed SiO_2 and remove photoresist. (e) Etch exposed Si. (f) Remove SiO_2.

To assemble the graphene sensing component and the PDMS layer, we first washed the coverslip with DI water and treated the PDMS layer with air plasma. Note that the coverslip with graphene cannot be treated with air plasma since the treatment will damage the graphene membrane. We employed a water-bonding technique, which has been proven to yield a strong bonding between the coverslip and PDMS layer[189]. After these two pieces were aligned using a

custom-built alignment microscope[189], a small amount of DI water was placed into each punched holes and the PDMS layer was lifted up from the coverslip using a blade to allow DI water to spread out in between. 2 h-baking is required to strengthen the bonding after the assembly. Next, tubing was inserted into the tubing supporters and media cylinders were attached. Two cut-off window PDMS pieces were put back to keep the electrode pads dry and clean before wire bonding. In the end, all microchannels were filled with DI water and deprived of air bubbles under vacuum.

4.2.3 Neuronal Cell Culture and Transfection Procedure

Glial cells at a density of 500,000 cells/ml were loaded into the device (25,000 cells/chamber) after coated with collagen. After glia cells reached confluence, neuron cells were loaded to the neuron culture chambers (50,000 cells/chamber), as described in Chapter II.

50 μl mCerulean or mCherry-Synaptophysin with GFP-GCaMP6Ps cDNAs (3-6 μg) were added to neuron culture chambers through the two inlet reservoirs after the microgroove valves were closed. Then, the device was placed in an incubator at 37°C for 60-75 min. Next, both chambers were washed with HEPES-buffered solution (HBS) (pH 7.15) for 1 h and then added 250 μl of fresh glia-conditioned B27 Neurobasal™ culture media.

4.2.4 Operation Protocol of the Microfluidic Platform

The operation protocol of the graphene transistor based microfluidic sensing platform are listed in Table 4.1:

Table 4.1 The operation protocol of the graphene transistor based microfluidic platform

Days	Operations
1	Sterilize the device via UV exposure;
2	Push down the microgroove valves and coat the two outer cell chambers with collagen and inner chambers with PLL;
3	Load glia cells to the two outer cell chambers;
4~7	Culture glia cells to reach the desired confluence;
8	Load neuron cells to the two inner cell chambers;
9~12	Lift up the valves and culture neurons, add fresh media to the inlets and remove waste media from the outlets;
13	Activate the micro valves and transfect neurons in two chambers with mCerulean and mCherry synaptophysin, respectively, and both chambers with GFP calcium probe;
14~15	Lift up the valves and continue to culture neurons;
16	Perform confocal microscopy, scanning photocurrent microscopy, and chemical stimulation.

On Day 16, differential interference contrast (DIC) and fluorescent images of the cells located between the 21 pairs of electrodes at the middle-sensing region were collected using a

Quorum WaveFX spinning disk confocal system with an inverted Nikon Eclipse Ti microscope. After wire-bonding the electrodes to a custom-built holder, scanning photocurrent microscopy was carried out at the transistor region. More specifically, the laser beam (785 nm) was deflected by a nanometer-resolution scanning mirror and then focused by a 40X objective (NA = 0.6) into a diffraction-limited spot on graphene transistors. The local photocurrent signals due to the alteration of the photoconductance of graphene were collected through externally bonded wires using a preamplifier.

Chemical stimulant can be delivered through two schemes: static stimulation and cyclic stimulation. Static stimulation was implemented by adding 200 μl high concentration K^+ medium to the middle channel inlet reservoir and keeping this stimulation for 2~3 min, while cyclic stimulation was performed by alternatively flowing high and low concentration K^+ media to the system for 1 min via the seesaw simulant delivery system.

4.3 Results

The fluorescent images and photocurrent mapping results over the graphene transistor area were obtained through confocal microscopy and scanning photocurrent microscopy. Fig. 4.12 (a)~(d) exhibit DIC and fluorescent images of neuronal processes transfected with mCerulean in blue, GFP calcium probe in green, and mCherry synaptophysin (a pre-synaptic marker) in red. Note that mCerulean and mCherry synaptophysin were separately transfected into each of the two groups of neurons while both were transfected with GFP calcium probe. Therefore, the overlap of three colors suggests potential synaptic contacts of neurons from different populations. In addition, photocurrent mapping results in Fig. 4.12 (e)~(h) show that the red/blue pair dots spatially correspond to neuronal structures, especially the synaptic area,

represented by a red square. The photocurrent signal can be measured with a spatial resolution of ~500 nm. As such, this platform provides a sensing approach of high spatial resolution for investigating individual synapses.

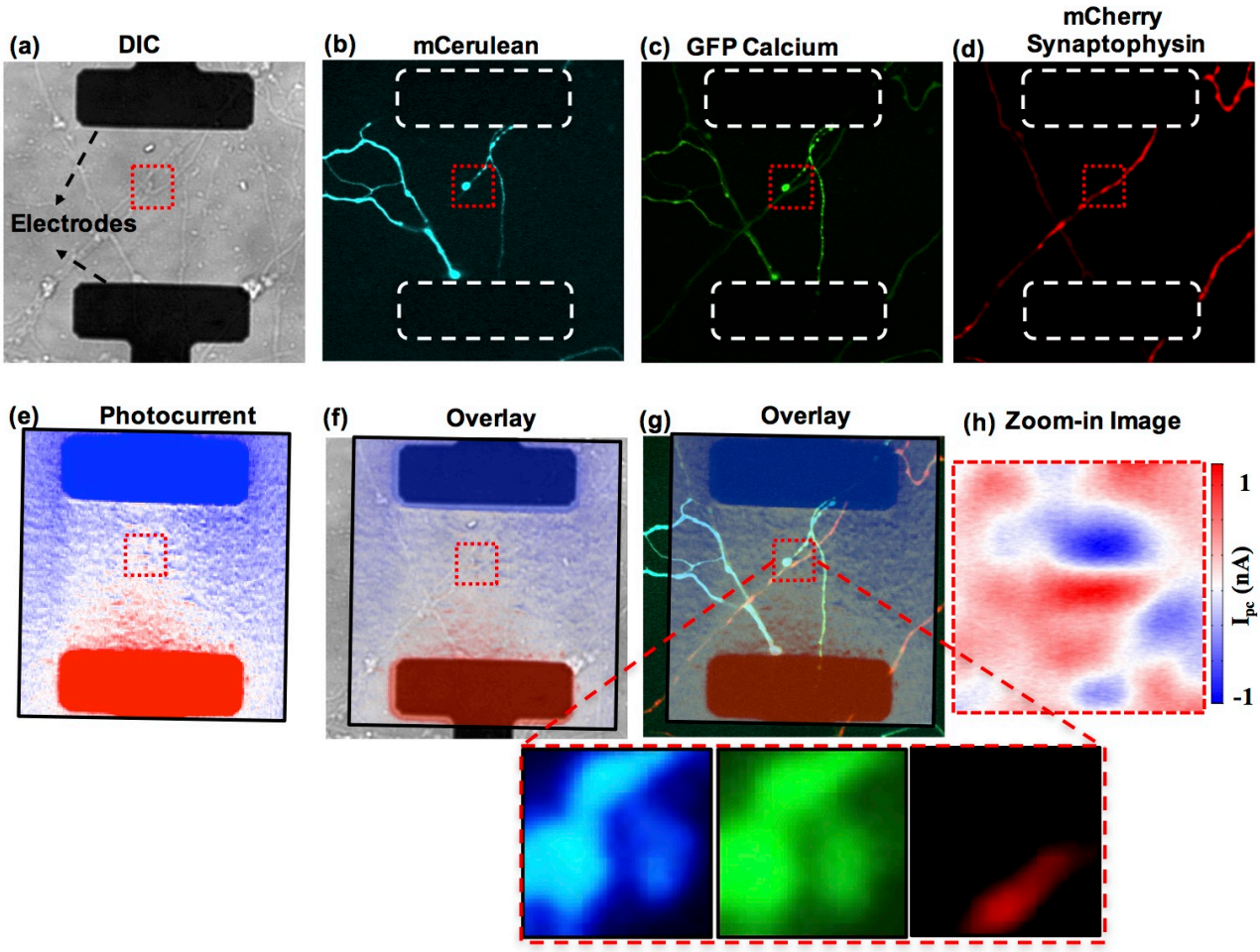

Figure 4.12 Confocal microscopic and scanning photocurrent microscopic images of neuronal processes over a single graphene transistor. (a) DIC image, (b) Fluorescent image of mCerulean (blue), (c) Fluorescent image of GFP calcium probe (green), (d) Fluorescent image of mCherry synaptophysin (red, pre-synaptic marker), (e) Scanning photocurrent mapping results (f) Overlay of DIC and photocurrent mapping images. (g) Overlay of fluorescent and photocurrent mapping images. Zoom-in fluorescent images show a synaptic contact. (h) Zoom-in image of photocurrent paired dots that spatially correspond to the synaptic area represented by a red square in DIC and fluorescent images.

We then focused the laser beam on one of the paired dots marked by a red square in Fig.

4.12 and proceeded with a static stimulation. Initially, the microfluidic device was filled with 4 mM K^+ HBSS. Then, the excessive 4 mM K^+ HBSS in the inlet and outlet reservoirs was removed and photocurrent was first recorded at a low K^+ environment. Next, 60 mM K^+ HBSS was dropped to the middle channel reservoir at 124 s, leading a signal perturbation (see Fig. 4.13 (a)). At ~170 s, a series of spontaneous depolarization events occurred in response to the high concentration of K^+ in extracellular environment, shifted the photoconductance of the graphene locally and caused a series of spikes in the measured photocurrent (see Fig. 4.13 (a)). Zoom-in plot in Fig. 4.13 (b) clearly shows more detailed information of the depolarization events. It should be noted that a single photocurrent burst lasts around 5 ms, which is consistent with the timescale of a typical neuron firing event. Therefore, it is reasonable to believe that these depolarization activities upon the stimulation of high concentration of K^+ are related to action potentials, although more biological evidences are required. Therefore, our platform successfully captured the synaptic firing activity in an ultrahigh spatiotemporal resolution. This function was further confirmed with multiple independent experiments, as shown in Fig. 4.14 (a)~(f).

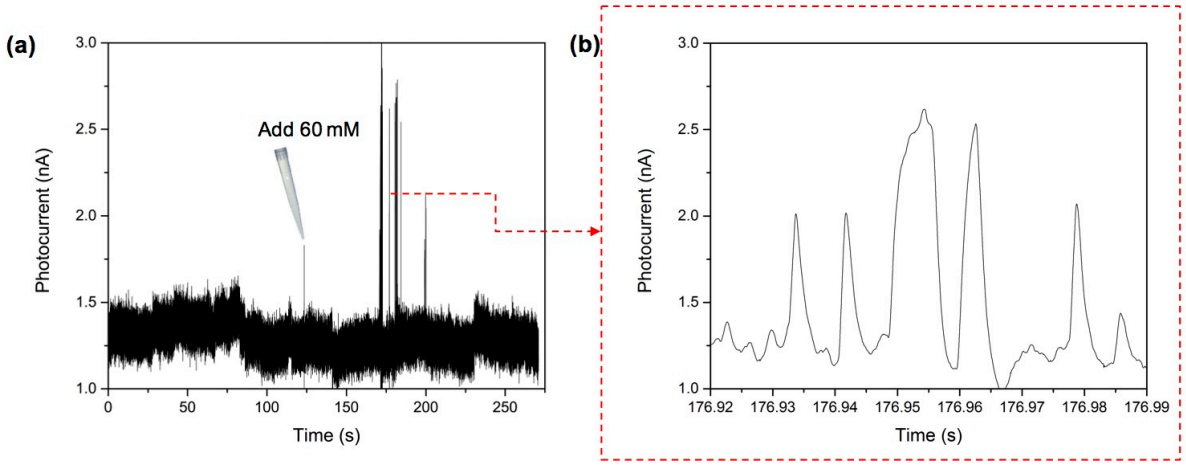

Figure 4.13 Real-time photocurrent recording upon a static stimulation. (a) A series of spontaneous neuron depolarization events occurred in response to stimulation of the 60 mM K^+. (b) Zoom-in of the depolarization signals. The time scale of a single photocurrent spike is around 5 ms, which is consistent with that of typical neuron firings.

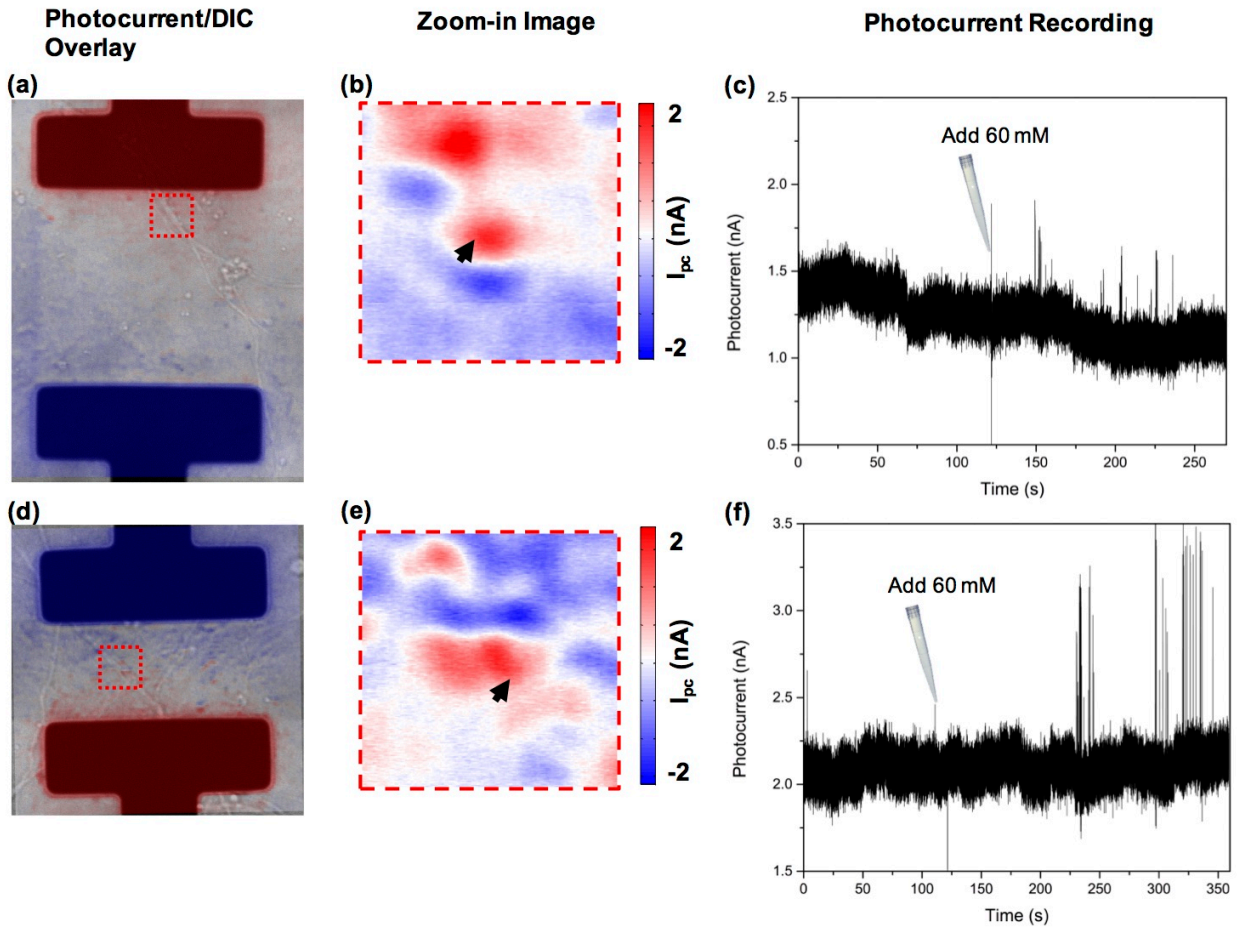

Figure 4.14 Multiple independent real-time photocurrent recordings upon a static stimulation of 60 mM K^+ solution. (a) and (d) The overlay of photocurrent and DIC images of two transistors from two devices. (b) and (e) Zoom-in images of photocurrent paired dots for the measurement of photocurrent upon chemical stimulation. (c) and (f) Real-time photocurrent recording upon a static stimulation of 60 mM K^+ solution.

Further, we performed cyclic stimulation by delivering 90 mM and 4 mM K^+ HBSS to the middle sensing channel of the device that was initially filled with 4 mM. One paired photocurrent dots denoted by a red square in Fig. 4.15 (a) was selected to proceed with this stimulation. In addition to this pair of photocurrent dots, multiple other dots marked by black arrows were also found along the same neuronal process, suggesting active electric activities at multiple synaptic locations. The stimulation was carried out with four 90 mM-4 mM cycles to

activate and restore the membrane potential periodically. Interestingly, 13 and 4 photocurrent bursts were observed during the 1st and 2nd 90 mM K^+ HBSS stimulation, respectively, while no bursts were recorded afterwards (see Fig. 4.15 (b)). To figure out the reason, fluorescent images of the cell structure before and after the stimulation were taken as shown in Fig. 4.16 (a) and (b), respectively, which exhibit significant difference. The initial intact, continuous neuronal processes became dotted and fragmented, and the intensity of fluorescence became significantly dimmer, suggesting that cells may have been greatly damaged by the high-K^+ stimulant. This provides a potential explanation on why neurons stopped responding to the 3rd and 4th 90 mM K^+ stimulation. Other reasons such as exhaustion of synaptic transmitters or decreased neuronal excitability are also possible.

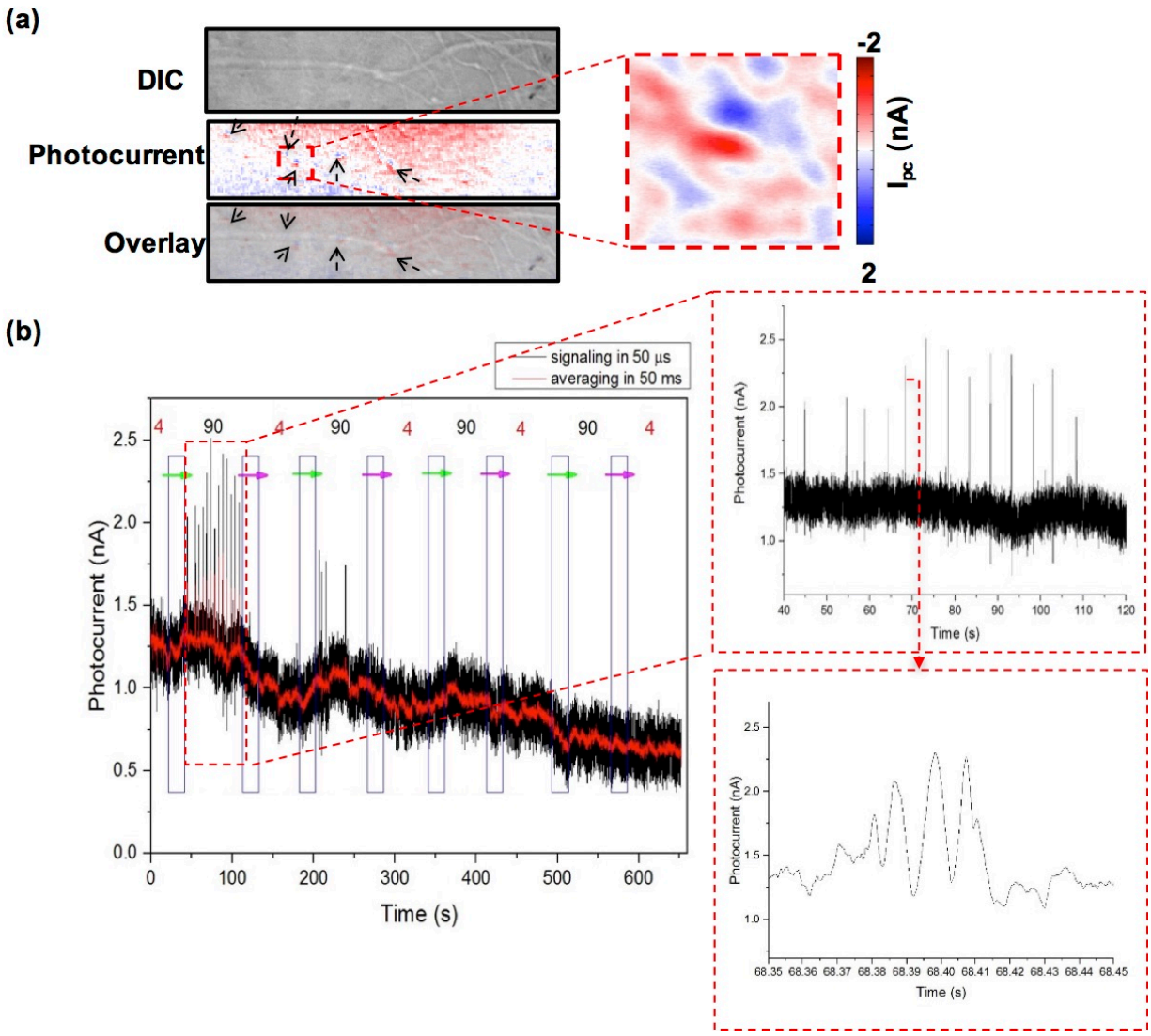

Figure 4.15 Real-time photocurrent recording upon a cyclic stimulation. (a) DIC and photocurrent overlay images. A pair of photocurrent dots marked by a red square was selected to proceed with a cyclic 4 mM and 90 mM K^+ HBSS stimulation. (b) Real-time photocurrent recording in response to a 4-cycle cyclic stimulation. Zoom-in plots show the detailed information of the bursts in the 1st cycle.

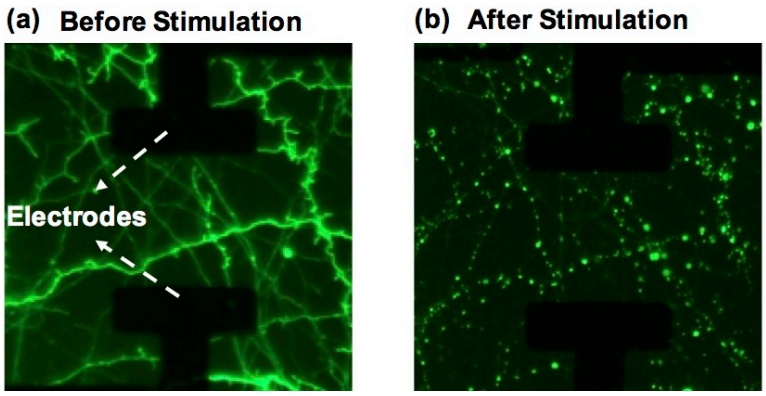

Figure 4.16 Neuronal processes were damaged after four cycles of 4 mM and 90 mM K^+ HBSS stimulation. (a) Fluorescent image before the stimulation; (b) Fluorescent image after the stimulation.

4.4 Discussion

We presented a graphene transistor based microfluidic sensing platform capable of detecting electrical activity of individual spines and synapses though scanning photocurrent microscopy. It possesses multiple favorable attributes such as high spatial resolution, high temporal resolution, high signal-to-noise (SNR) ratio, transparency, and sustainability of long term culture. It represents a promising new neurotechnology that could have significant advantages over current popular approaches including patch-clamping, optical imaging, and MEAs. Conventional patch-clamping method, despite high temporal resolution and high SNR, is laborious, time-consuming, and of very low throughput. In addition, the operation is technically challenging and heavily relying on experienced professionals[109,190]. On the other hand, optical imaging of calcium activity can access many cells at the same time; however, the temporal resolution is limited and it is difficult to detect the dynamic information encoded in an individual action potential during neuron firing activity[112]. Genetically targeted voltage indicators then appeared and gained broad popularity because it significantly improved the temporal resolution. For example, Cao et al.[191] demonstrated an optical method allowing for simultaneously recording

of the membrane potential of multiple genetically targeted neurons via expression of fluorescent voltage indicators (GEVIs). This method can also measure electrical activities of soma, dendrites, and synaptic terminals of the genetically targeted cells. Despite the promising role in neuron electrophysiological measures, it also has limitations: the signal magnitude is reduced and the dynamic response of spikes is slower compared to the conventional patch-clamping method. Therefore, it is difficult to accurately reflect the physiological information from the burst waveform and pattern. As another alternative, MEAs is an established tool to map electrical activity of neurons in large-scale networks. However, the limited spatial resolution (>30 μm) due to current thin film technology and numbers of integrated electrodes (range of hundreds) due to the external wiring, the amplification, and signal conditioning circuitry approaches[113,192] do not allow for measurement at single cell level, let alone subcellular activity recording. Recently, upgraded MEAs based on CMOS technology have emerged to solve the inherent issues in this methodology. The CMOS MEAs can be arranged in higher spatial resolution than traditional MEAs through multiplexing techniques, i.e. employing shared wires controlled by electronic switches[192]. Luca et al.[193] reported a CMOS MEAs platform with a spatial electrode separation of 21 μm, and this number was further reduced to 17.5 μm in a later work by Jan et al.[192]. However, this is still not sufficient for studying signal transmission at individual spine and synapse level. Compared to all existing approaches, the graphene transistor based microfluidic sensing platform has multiple advantages:

First, as an extracellular electrophysiological recording technique, this platform does not require intensive and skilled operation on a single fragile neuron cell as patch-clamping method does. Instead, by conveniently flowing cell suspension to the culture area and allowing axons and

dendrites to grow to the sensing area, synaptic activities of multiple cells can be detected easily. This significantly increases the throughput and efficiency of the electrophysiological recording.

Second, on the contrary to optical imaging method, this platform, in addition to precluding the effect of phototoxity, allows for real-time recording of the dynamics of single depolarization event (in a time scale of a few milliseconds).

Third, compared to all different kinds of MEAs, this sensing platform takes advantage of atomically thin 2D material, graphene, and covers a broad sensing area with only 21 pairs of electrodes versus 26,400 microelectodes in Jan et al.'s device[192]. Each of 21 transistors takes up 900 μm^2, 1350 μm^2, and 1800 μm^2 sensing area for three settings with the electrode pair distances of 20 μm, 30 μm, and 40 μm. Therefore, without the need to arrange high density spatially separated microelectrodes, this platform can achieve significantly higher spatial resolution.

This platform indeed has some limitations. For example, the quality of contact between graphene and cells is very critical in the photocurrent measurement. This is the potential reason why there is no photocurrent detected at some active synaptic areas marked by Ca^+ indicators. Secondly, although this platform can access a great number of neuronal processes simultaneously, dynamic measurement of depolarization events upon chemical stimulation has to be carried out individually. Despite the limitations, this platform is of great potential of becoming another popular electrophysiological measurement tool in the near future.

4.5 Summary

Given the importance of dendritic spines and synaptic plasticity in learning and memory, extensive attention has been drawn into neurobiology. However, many fundamental molecular

mechanisms remain open questions, largely because technological limitations prevent researchers from exploring the electrical activities at individual synapse or dendritic spine levels.

In Chapter IV, a graphene transistor based microfluidic sensing platform capable of detecting electrical activity at single synapse level in real-time was demonstrated. Many advantages of this new approach render it great potential of becoming another impactful neurotechnology that can attack important neurological issues.

CHAPTER V

A MICROFLUIDIC DIODE FOR SORTING AND IMMOBILIZATION OF CAENORHABDITIS ELEGANS

5.1 Motivation

In the previous chapters, multiple microfluidic platforms were illustrated and applied to study subcellular and cellular activities and behaviors. In this chapter, microfluidic platforms will be adopted to organismal investigations.

Caenorhabditis elegans (*C. elegans*) has been broadly used in developmental biology and neurobiology studies[194,195] since their adoption by Sydney Brenner in 1965[196], owning to its numerous attributes advantageous for experimentation. Their small size (~1 mm long, 959 cells), short lifespan, transparency, ease and low cost of culturing, and completely mapped cell lineages make *C. elegans* a favourable organismal model. Because its genome (the first multicellular genome to be sequenced) is ~65% similar to the human genome[197,198], it has been widely used to study human aging[199] and diseases such as Parkinson's and Alzheimer's disease[200], diabetes and depression[201].

After *C. elegans* are hatched from eggs, they experience four larval stages (L1, L2, L3, L4) and develop into reproductively mature adults in approximately three days. At each developmental stage, the worms feature different body sizes, biological composition and behaviors[202,203]. These variabilities result in complexity in biological assays[204,205]. In addition, the mobility of *C. elegans* leads to further difficulty in high-resolution imaging and manipulation at the cellular and sub-cellular levels for most biological processes[200,204,206–211]. Therefore,

synchronized and immobilized worms are often required in many studies. Conventionally, worm sorting is often carried out by hand-picking or chemical synchronization while immobilization is commonly implemented through glue or anaesthetics[197,200,202–214]. However, these operations involve extensive manual handling and thus are notoriously laborious, time-consuming, and of low throughput[197,200,202–205,210,212,213]. Additionally, the biological influence of the chemical agents employed in these processes are not well-understood[197]. Other methods such as the commercially-available COPAS Biosorter, despite its merits for the efficiency and ease of handling *C. elegans*, is expensive and not readily available in many laboratories[197,205]. This machine may also demand large amounts of biochemical solutions and complex operating procedures[197].

Recently, customized microfluidic devices, as inexpensive, accessible, user-friendly and highly-efficient tools, have been utilized in *C. elegans* sorting and immobilization. There are two commonly-adopted working mechanisms for sorting: (1) electrotaxis-based self-sorting, and (2) flow-driven passive-sorting. It has been reported that worms show a tendency to swim toward the cathode under an electric field, which is referred to as electrotaxis[215]. Han et al. took advantage of this feature as well as the worms' structure-dependent swimming behavior and designed a micro-bump array capable of sorting around 4 worms per minute with 95% accuracy[213]. In addition, Wang et al. demonstrated that worms at different developmental stages exhibited different deflecting angles under the same strength of electric field[203]. Based on this feature, they successfully sorted worms into all developmental stages at a throughput of ~56 worms per minute. Note that while electrotaxis-based self-sorting is becoming a promising and popular strategy, the underlying mechanisms are not yet fully understood, and hence the biological influence on worms is not completely known[205].

The other microfluidic sorting strategy, flow-driven passive-sorting, uses flow as the driving force and separates worms into different groups by size via various channel structures. For example, Solvas et al. designed a 'smart maze' worm sorter capable of sorting large numbers of adult worms from larvae[202]. Also, Ai et al. reported a sorting device allowing smaller worms to swim through micro-posts filtration more quickly than bigger worms with the assistance of flow so that larger ones would be left behind to achieve separation[205]. Similarly, Dong et al. designed a microfluidic channel with an adjustable cross-section controlled by externally applied pressure[212], which could work as a filter that allows smaller worms to pass while blocks the larger ones. All these studies are conducted with binary separation, i.e. separating two populations of worms of distinct sizes within one operation.

In addition to sorting, microfluidics also offers a simple, efficient, and highly-controllable solution to immobilize worms for further investigations by means of membrane deflection, suction channels, and geometric restriction, etc. For example, a deformable membrane has been used to squeeze the worm into a narrow slot to restrict the worm's locomotion[207,211], allowing for high-resolution, real-time fluorescent imaging of the neuronal processes of the worm. An alternative method proposed by Rohde et al.[210] employed an array of suction channels to draw the worm against the microchannel with the assistance of vacuum. Later, the suction channels were further combined with membrane deflection for better immobilization of worms[200,206]. To achieve parallel immobilization of multiple worms, S. Hulme et al.[208] reported a device comprising an array of 128 wedge-shaped microchannels capable of physically confining worms into gradually narrowing channels with the help of flow. Worms can be released by applying a reversed flow from the outlet of the device. This method does not damage the worms given that the released worms were able to live and reproduce normally. However, immobilized worms

exhibited a random orientation: head-first orientation (63 out of 116 worms) and tail-first orientation (53 out of 116 worms), which may lead to additional complexity, time and cost in the process of high-resolution subcellular imaging and analysis[216].

To establish better microfluidic *C. elegans* assays, here we propose a unique diode structure, a microchannel consisting of a curved head and a straight tail, which demonstrate rectified *C. elegans* passage with much easier translocation from the curved side. Microfluidic platforms based on this *C. elegans* diode could sort worms into different developmental stages, and allow for collection or immobilization in sequential steps. The platforms could function well even in the presence of eggs and debris, which is a common issue in many microfluidic chips with small channels because of clogging[217–220].

5.2 Material and Methods

5.2.1 *C. elegans* Culture

The *C. elegans* wild-type Bristol strain N2 was cultured at room temperature (20-22℃) on 60 mm Nematode Growth Medium (NGM) agar plates spotted with the OP50 *E. coli* strain, according to established protocols[221]. For sorting of mixed stages, non-synchronous cultures of *C. elegans* containing eggs, L1 through L4 larvae, and adults of various ages were collected by washing them off the plate with standard M9 media. To passage worms to fresh plates before the *E. coli* food source was exhausted, a chunk of NGM agar containing worms was periodically excised from a non-starved plate and placed on a new plate with an OP50 *E. coli* bacterial lawn.

5.2.2 Preparation of Synchronous Worms

To test the performance of the microfluidic *C. elegans* diode structure, several synchronized worm populations were used. For synchronization, gravid (egg-filled) worms and eggs were harvested in M9 by washing and collecting worms off plates. These worms and eggs were treated with a sodium hypochlorite/sodium hydroxide solution for 5 min, killing all adults and larvae, but leaving the eggs[221]. The bleaching solution was removed by washing eggs three times in M9 and eggs were allowed to hatch during an 18+ h bacteria-free incubation in M9. Upon egg hatching, L1 larval worms arrest in the L1 stage and do not resume development until they are placed on new NGM agar plates containing the OP50 *E. coli*[222].

5.2.3 *C. elegans* Microfluidic Diode Design

The microfluidic diode features a curved head and a straight tail. The design is based on our observation that worms entered curved channels without much resistance while they failed to get into straight channels, if the channel width is roughly the same as the worm diameter. The curvature design is also inspired by the fact that worms adopt an approximate sinusoidal waveform when they move[223–230] and show enhanced locomotion in an array of micro-posts compared to in bulk solution[228]. As shown in Fig. 5.1 (a), a worm failed to make its way through straight openings after seven attempts in front of different straight channels (denoted by red arrows) with the assistance of media flow at a flow rate of 3 µl/min (corresponding to a flow velocity of 0.3 mm/s). On the contrary, four worms easily entered the curved channels under the same flow rate (represented by green arrows). In addition to the ease of entry, the curvature generates propulsion force in the forward direction when worms are in contact with the channel wall[213], thereby facilitating passage of the worm into the channel.

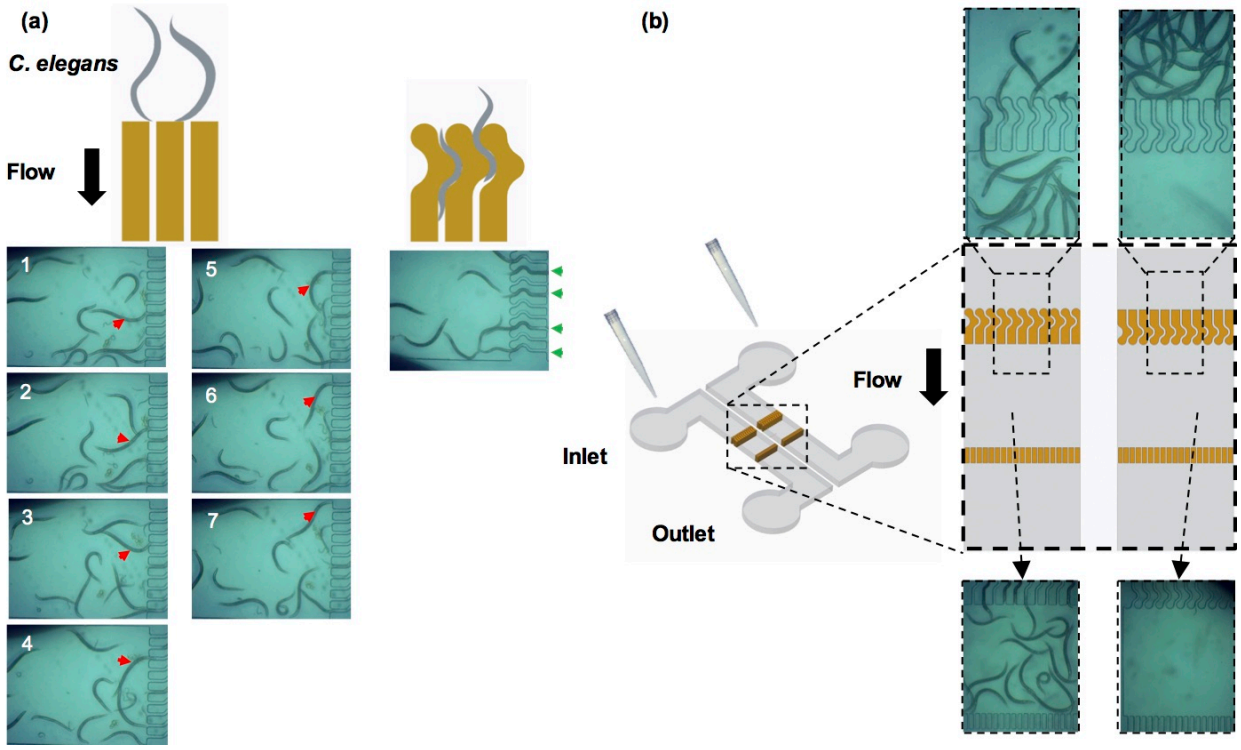

Figure 5.1 Schematic of microfluidic diode arrays. (a) Different worm entry behaviors encountering straight and curved channels. A worm failed to enter the straight openings after seven attempts (denoted by red arrows) under a flow rate of 3 µl/min. In contrast, 4 worms easily entered the curving structure under the same flow rate. (b) Schematic of microfluidic diode-based characterization device consisting of two channels with opposite diode configurations: 1. curved head and straight tail, 2. straight head and curved tail. This is designed to characterize the number of synchronized worms in an average diameter of ~35 µm that pass through the diode arrays (35 µm wide) under different flow rates.

To test the rectification effect of the microfluidic diode, we designed two sets of microfluidic diode channels with (1) a curved head and a straight tail, and (2) a straight head and a curved tail. The channel width is set to be 35 µm, which is roughly the same as the average diameter of the synchronized worms used in this test. To characterize the performance of the diode, we counted the number of worms passing through the arrays under different flow rates, as shown in Fig. 5.1 (b). The flow rate is controlled by a Nexus 3000 High Flow Syringe Pump

(Chemyx, Stafford, TX). The height of the microfluidic channels is 80 μm and the upstream and downstream channels of the microfluidic diode structure are 1.9 mm wide and 11 mm long. A row of smaller straight channels (20 μm wide) is included in the downstream to keep the worms in the device for further counting and characterization. Fig. 5.1 (b) demonstrates a significant difference on the number of passed worms for these two configurations and indicates the remarkable uni-directionality of the microfluidic diode.

5.2.4 *C. elegans* Sorting Device Design

After a systematic characterization of the diode performance, we applied the diode arrays to worm sorting. The sorting device is composed of two PDMS layers, the bottom sorting chamber (30 mm long × 9.5 mm wide × 80 μm tall) and the top pressure chamber (25 mm long × 3 mm wide × 200 μm tall). The sorting chamber is patterned with multiple rows of microfluidic diode arrays with different channel widths along the direction of the flow. This sorting device is designed to be 5 times as wide as the aforementioned characterization device to fit more diode structures, allowing for high sorting throughput. Therefore, the volume flow rate in the sorting device is also five times that in the diode characterization device for the same flow velocity.

Here we designed two settings for different purposes: setting 1 comprises five diode arrays with channel widths of 40 μm, 25 μm, 20 μm, 15 μm, and 10 μm, allowing for separation of a mixture of worms into each stage (adults and L4, L3, L2 and L1)[231]; setting 2 contains six diode arrays of 50 μm to 25 μm channel widths with an interval of 5 μm to achieve a finer division based on the worm diameter alone, given that certain stages cover a wide size range (see Fig. 5.2 (a)). Side channels branching out from the main sorting chamber are designated to

collect worms afterwards. The collection channels are closed during the sorting process and open in the collecting process. This is achieved by deflection of the PDMS roof of the collection channels controlled by a top pressure chamber, i.e., a pressure valve[117]. When the pressure chamber is pressurized hydraulically via the connected inlet/outlet tubing, the PDMS roof over the collection channel will be deformed into the channel below and seal the area. To achieve a good seal, the deformable area has to be flexible enough to completely block the 2 mm long × 1 mm wide × 80 μm tall channel underneath. However, during fabrication, to be peeled off the mold intactly, the sorting chamber area at the bottom PDMS layer has to be sturdy enough to prevent the structure from being torn apart by the adhesion force with the SU8 mold, especially with a great number of micro-arrays. In the device fabrication, we used a two-step molding method to meet both requirements. First, we poured a small amount of PDMS over the mold to form a thin layer; after it polymerized, we placed a 3D-printed block (20 mm long × 1 mm wide × 1.5 mm tall) at the pressure valve area and poured PDMS again on top of the first PDMS layer. This allows for easy peel-off of the PDMS and removal of the 3D-printed block leaves a thin membrane valve (denoted by a red circle in Fig. 5.2 (a), cross-section AA'). The valve has been proven to be functional, as shown in Fig. 5.2 (b). When the valve was turned on, the dye that was flowed into the sorting chamber did not spread to the collection area; however, the dye dispersed into the collection channels and tubing immediately after we released the pressure and turned off the valve. The valve can also be switched back on to cut off the flow.

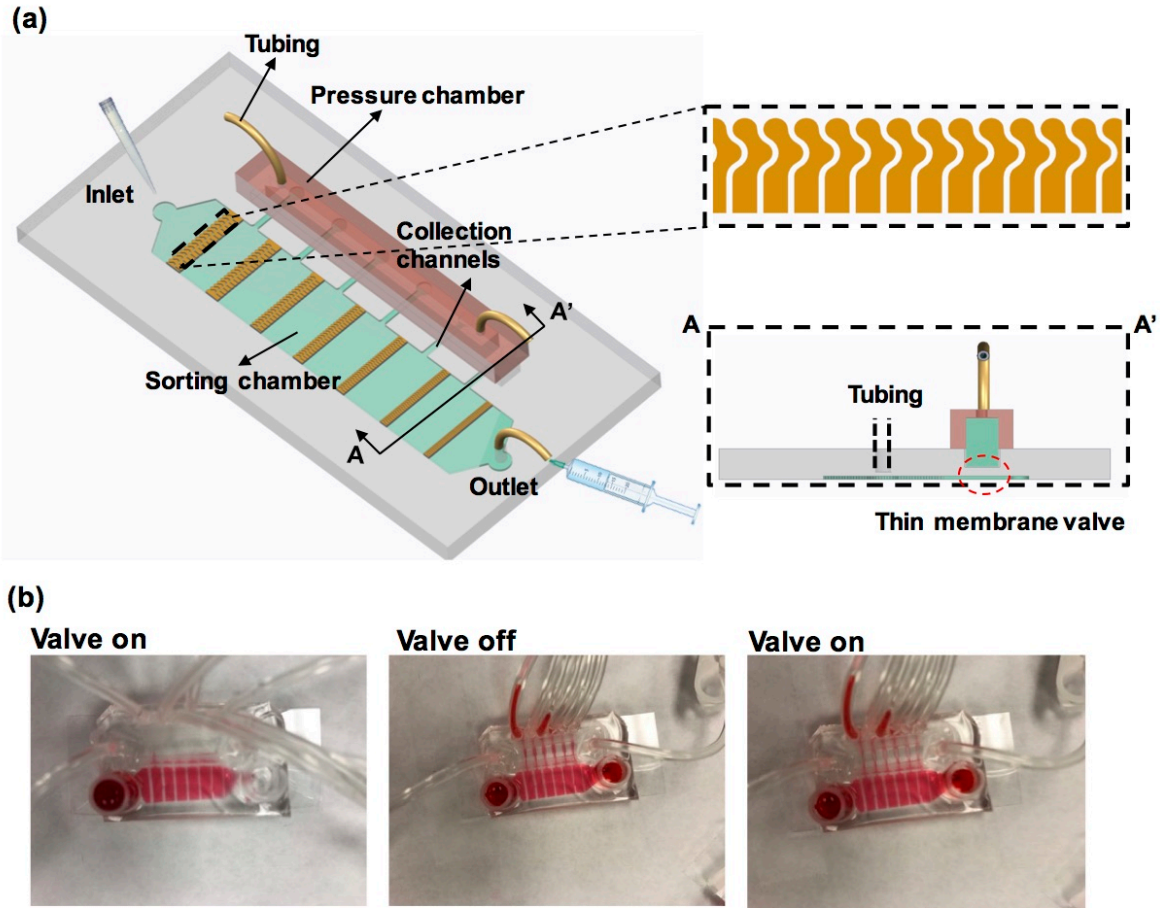

Figure 5.2 Schematic of microfluidic diode-based sorting device. (a) The sorting device comprises two PDMS layers: the bottom sorting chamber with 6 rows of microfluidic diode arrays in different widths, and the top pressure chamber that controls the thin membrane valve. (b) Photographs of controllable channel access regulated by thin membrane valves.

5.2.5 Device Fabrication

The devices were fabricated using standard soft-lithography techniques via PDMS (Sylgard 184, Dow Corning, Auburn, MI) replica molding as previously reported[232–234]. Briefly, a pre-polymer PDMS solution was mixed with a curing agent at a weight ratio of 10:1 and poured over the SU8 mold fabricated through photolithography technique. After being degassed for 1 h and cured in a 70°C oven for 2 h, the PDMS was fully polymerized. It was then cut out and peeled from the mold. Holes were punched through the PDMS for loading the worm

suspension. After this, we assembled the PDMS layer with a 100 μm-thick glass coverslip (No. 1, VWR Vista Vision, Suwanee, GA) with the assistance of oxygen plasma treatment. Next, Pyrex cloning cylinders, 8 cm in diameter and 8 cm in height (Fisher Scientific, Pittsburgh, PA) and Tygon tubing (0.20" ID x 0.60" OD) (Cole-Parmer, Vernon Hills, IL) were attached to the inlet and outlet hole area, respectively. The fabricated device was filled with sterilized water to keep the interior surface of the device hydrophilic before usage.

5.3 Results

5.3.1 Characterization of the *C. elegans* Microfluidic Diode

To characterize the performance of the microfluidic diode, we counted the number of worms that passed through the diode arrays from both the curved and the straight sides at different flow rates, as shown in Fig. 5.3. Interestingly, we observed three working regimes. I. The natural worm locomotion-dominated regime (in yellow). Worms were able to pass through the diode from the curved opening, but no worm could cross from the straight side below a flow rate of 3 μl/min or a flow velocity of 0.3 mm/s. In this regime, the flow only guides the worms to the diode arrays but does not play a role in the worm passage through the diode. II. The combined self-motion and flow-driven regime (in blue). In this regime, more worms passed through from the curved opening when the flow rate went up from 3 μl/min to 5 μl/min. Meanwhile, a few worms also crossed from the straight side with the assistance of the flow. III. The passive flow-driven-dominated regime (in pink). In this regime, flow plays a dominant role in the worm passage through the diode, i.e., worms pass through the diodes passively with the flow and the diode loses its unidirectional characteristic. As a result, no significant difference in the number of worms from the curved and straight side was observed at 7 μl/min. With the flow

rate increasing to 10 µl/min, we even observed that some worms were flushed through the downstream 20 µm-wide 'fence' channels, which was the reason that the worm number decreased at the 5-min time point.

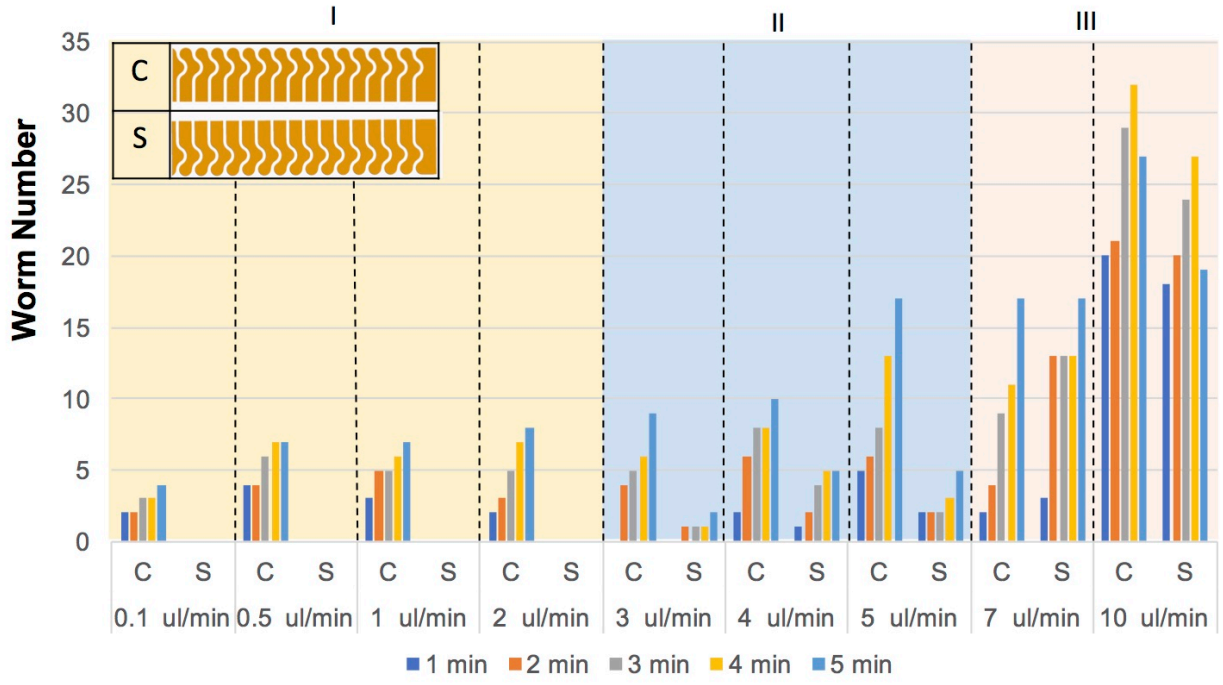

Figure 5.3 Characterization results of the microfluidic diode. The number of worms that passed the microfluidic diode arrays from both curved and straight openings at different flow rates. The results indicate three working regimes: I. The natural worm locomotion-dominated regime (in yellow); II. The combined self-motion and flow-driven regime (in blue); III. The passive flow-driven-dominated regime (in pink).

These characterization results promote us to take advantage of the diode structure for better *C. elegans* sorting at a relatively low flow rate. To date, almost all reported microfluidic *C. elegans* sorting has been demonstrated with a binary mixture of pre-synchronized worms at different stages. However, to work with a wild-type colony in the presence of egg clusters and debris, a high flow rate will lead to channel clogging by the egg clusters and debris if the channel dimension is small. As such, we hypothesize that a low flow rate that only guides the worms to

swim but does not move the egg clusters and debris could help to achieve a better sorting performance. The following sorting results confirmed the above hypothesis.

5.3.2 *C. elegans* Microfluidic Diode-based Sorting

C. elegans sorting was conducted with a colony of worms at all different stages from an *E. coli* seeded NGM agar culture plate without any pre-selection. The *C. elegans* microfluidic diode-based sorting device achieved an average throughput of 97±**4** worms per minute under a flow rate of 12 μl/min. Note that this flow rate is equivalent to 2.4 μl/min in the diode characterization device in Fig. 5.3 because the channel in this sorting device is 5 times wider. Therefore, the sorting device works in the worm locomotion-dominated regime. For sorting, we suspended worms of all different stages intermingled with egg clusters and debris from a culture plate and directly loaded the media into the inlet reservoir of the sorting device of setting 1 without any pre-selection, as shown in Fig. 5.4 (a). After 5 min, adults and L1~L4 were successfully separated in different regions, while larvae of size smaller than 10 μm were drawn out of the device through the outlet tubing. It should be noted that originally the inlet reservoir contained large egg clusters denoted by red arrows. However, these clusters did not cause any clogging issue under the current operation condition. The separated worms could be collected with the membrane valve turned off and the size of worms (n=~30) in each region were measured (see Fig. 5.4 (b)), indicating a remarkable separation performance.

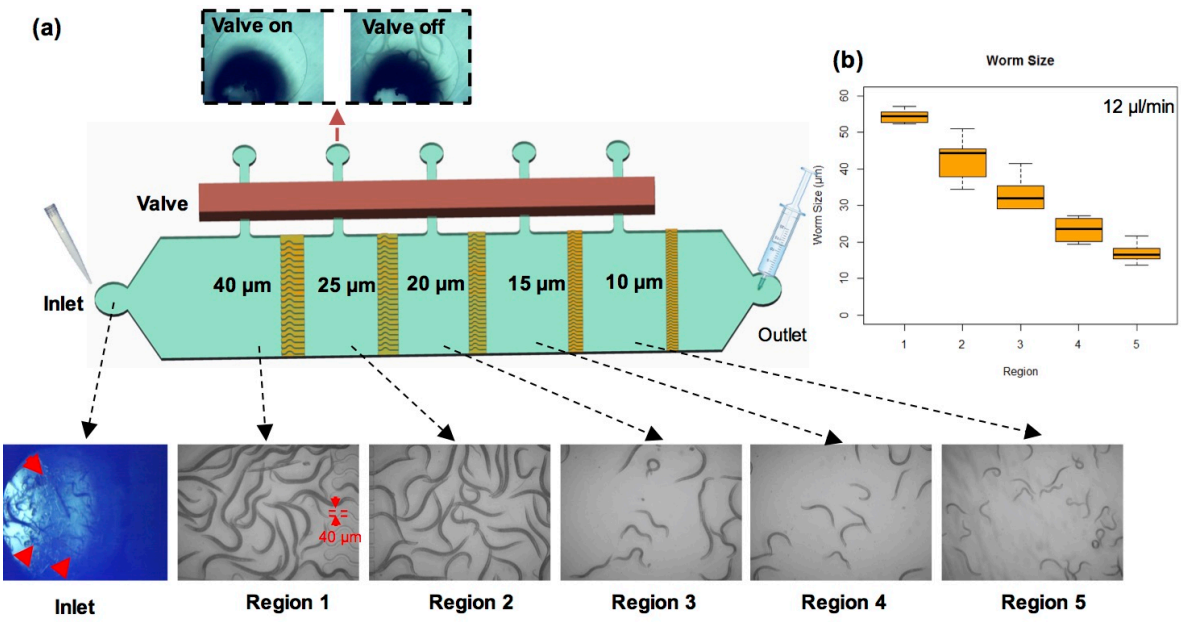

Figure 5.4 Worm sorting through a microfluidic diode-based sorting device. (a) Schematic and performance of the sorting device. It managed to separate worms into different stages from an original worm suspension with high efficiency. The red arrows denote that the mixture in the inlet reservoir contained large egg clusters. The bottom panel shows the well-sorted worms in each region. The top panel demonstrates the worm collecting process followed by sorting. When the membrane valves are closed, no worms enter the collection reservoirs; and when the membrane valves are open, sorted worms can be collected from the collection reservoirs. (b) The boxplot of worm size distribution in each region (n=~30).

We also performed worm sorting in the device of setting 2 for a finer division on worm size at 12 μl/min (see Fig. 5.5 (a)). To achieve an optimized sorting, other operation parameters were also tested. We observed a similar size distribution under 5 μl/min (equivalent to 1 μl/min in the characterization device) with a decreased average throughput of 68±6 worms per minute (Fig. 5.5 (c)). This is because fewer worms were introduced into the device per minute by the flow in this condition. In addition, to demonstrate the advantage of the diode-based sorting device, we also constructed straight channel-based sorting devices with corresponding channel sizes the same as the diode structures. These devices presented significantly deteriorated performance for both 12 μl/min and 5 μl/min flow rates (see Fig. 5.5 (b, d)). In fact, most worms

were cramped in region 1 and exhibited difficulty in passing through the channels, leading to a much worse sorting efficacy.

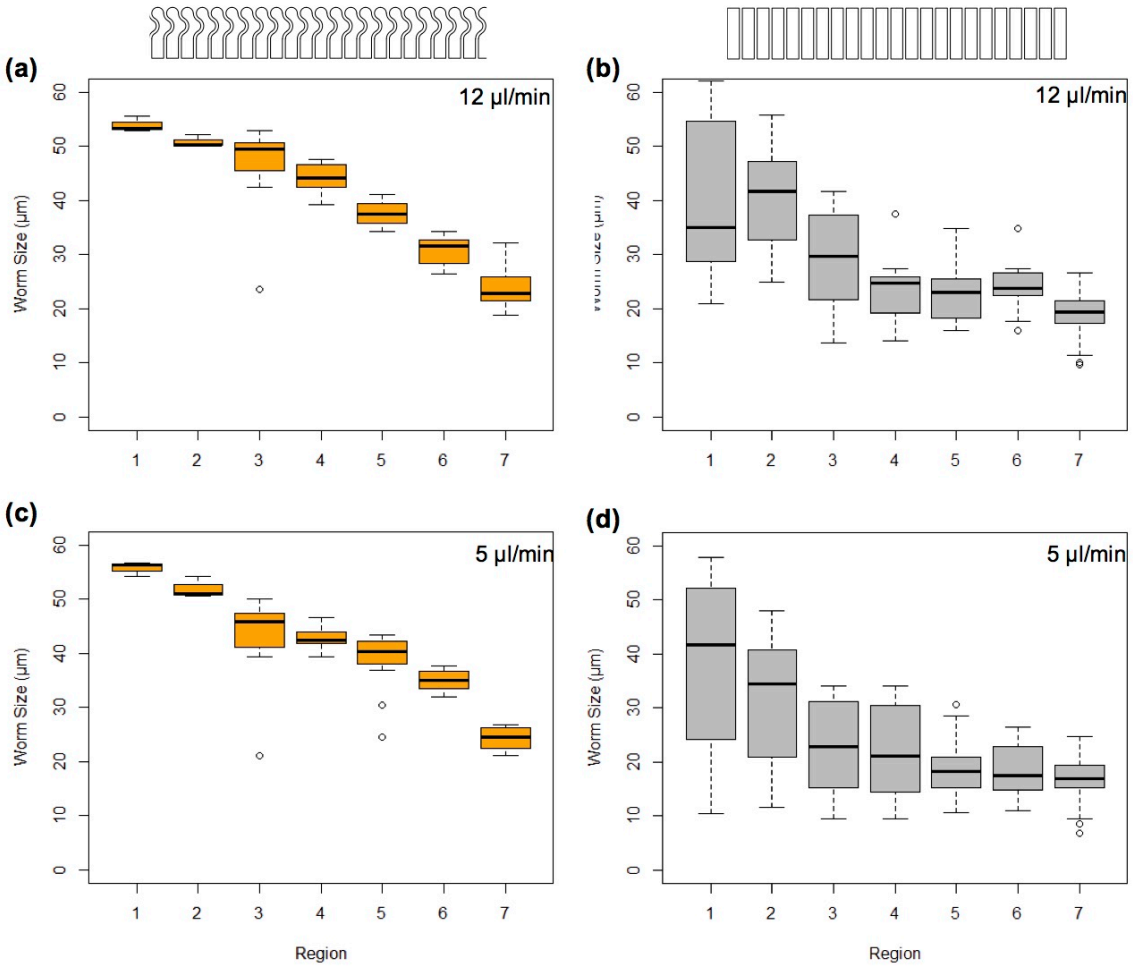

Figure 5.5 Comparison of sorting performance. (a, b) The size distribution of worms in a diode-based and a straight channel-based sorting devices under a flow rate of 12 µl/min, respectively. (c, d) The size distribution of worms in a diode-based and a straight channel-based sorting devices under a flow rate of 5 µl/min, respectively.

5.3.3 *C. elegans* Microfluidic Diode-based Immobilization

For further study of sorted worms (e.g. drug screening and microscopy studies), it is often necessary to trap the worms in a fixed position. As such, we integrated immobilization function with the sorting platform. This is realized with a switch between two perpendicular flow

directions controlled by membrane valves, as shown in Fig. 5.6 (a). When the valves were turned on, worm sorting was achieved as described previously with the assistance of a vertical flow as denoted by the blue arrow in Fig. 5.6 (a). After sorting, the membrane valves were turned off and immobilization was carried out under a horizontal flow as indicated by the black arrow. In this device, the aforementioned collection channels were replaced with modified diode arrays of regular curved heads and elongated and tapered tails (see the zoom-in graph denoted by a red dash-line square in Fig. 5.6 (a)). The immobilization was conducted under a flow of 20 μl/min (corresponding to a flow velocity of 0.3 mm/s), during which the well-sorted worms entered the tapered channels (see Fig. 5.6 (c)). The immobilization channel becomes narrower gradually, from the larger width of the upstream section to the smaller width of the downstream section (Fig. 5.6 (d)) over a length of 1.4 mm. Because of the nature of the self-driven motion, the flow and the tapered structure did not exert strong aversive mechanical impact to the worms. In fact, we observed that after being immobilized, the worms were able to wiggle their heads and tails for at least 3 hours. Importantly, all worms were oriented with their heads forward and stably kept at the same location, which allows for convenient microscopy studies of an array of worms.

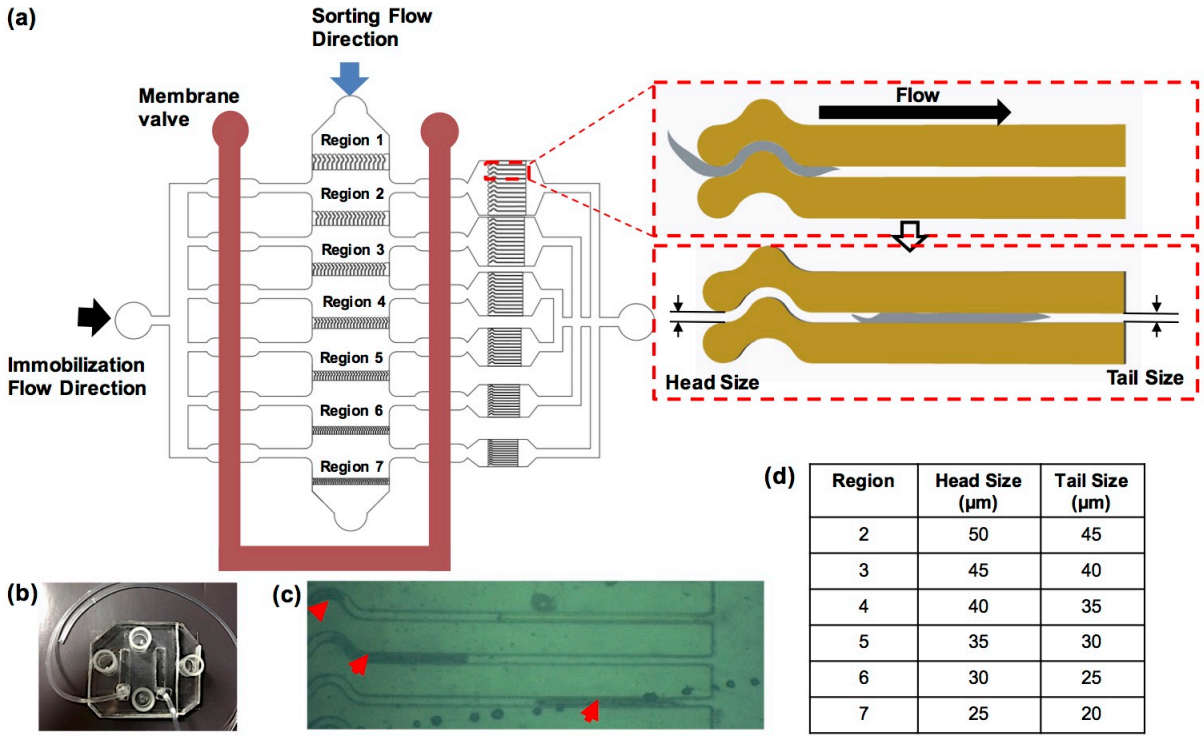

(d)

Region	Head Size (μm)	Tail Size (μm)
2	50	45
3	45	40
4	40	35
5	35	30
6	30	25
7	25	20

Figure 5.6 Worm immobilization. (a) Schematic of the device. The sorting device was expanded to include immobilization components: the modified diode channels with regular curved head and longer tapered tail. The zoom-in drawing enclosed in a red rectangle shows that the well-sorted worms entered and stayed in the tapered channels with the assistance of the flow. (b) Photograph of the device. (c) Photograph of the immobilized worms. (d) A dimension table of the heads and tails of immobilization channels at each region.

5.4 Discussion

The microfluidic *C. elegans* diode, which is designed based on the locomotion characteristics of the worms, only allows *C. elegans* to pass through from the curved side, but not the straight side, as long as the flow speed is below 0.3 mm/s. Owing to unidirectional passage nature, the diode structure facilitates worm sorting and immobilization. Importantly, with the relatively slow flow rate, we can avoid the clogging issue from egg clusters and debris and successfully separate a whole wild colony of *C. elegans* into different developmental stages.

Another merit of our *C. elegans* microfluidic diode-based sorting device is its capability of sorting worms into different size ranges within one operation. Although previous microfluidic sorting devices that adopted flow-driven passive-sorting and size-based filtration strategies have been proven to be highly efficient, they require repetitive operations and multi-stage settings to separate worms into different developmental stages[205,212]. One example is the size-based microfluidic sorting device comprising an adjustable filter structure, i.e. the cross-section of the fluidic path connecting two worm chambers can be tuned through deformation controlled by precisely applying pressure[212]. It is able to extract a single group of worms at certain stage or desired mixed groups of worms from the initial heterogeneous worm population. Through subsequent filtering steps with appropriate control pressure, a mixture of worms could be separated into populations of the five developmental stages. However, precise and repeatable control of channel cross-section for different devices could be a challenge. Another example is also a filter setting as reported by Ai et al. previously. It consists of an array of geometrically optimized micro-posts that allow worms of a specific small size to pass through with the assistance of a driving flow while trapping larger worms[205]. To separate a mixture of worms into five developmental stages, they designed four devices with varying chamber heights and post spacing. In this scheme, both devices are limited to binary separation, i.e. extracting one worm group (single stage or mixed stages) from the initial mixture within one operation. To achieve separation of multiple size ranges, both approaches involve repetitive operations of worm collection/reloading and adjustment of filter settings or control pressure in subsequent steps. Further, during these steps, more uncertainties could be introduced. For example, as Ai et al. pointed out, there was a general decrease in the worm purity when four devices were set up in sequence compared to that of a single device[205]. In the light of these limitations, our simple

sorting device based on the microfluidic *C. elegans* diode structure allows for separation of worms into different developmental stages based on their sizes in one single operation, which represents a major step forward in microfluidic *C. elegans* sorting.

It should also be noted that, after the sorting process, worms will be trapped in the corresponding regions and not be able to crawl back from the straight tail due to the uni-directionality of the microfluidic diode. This prevents contamination between neighboring worm samples and maintains the purity of each sorted group. Such advantage does not rely on external driving flow or externally applied pressure but the diode structural characteristic and worm locomotive nature. Therefore, this device will be of great convenience in drug screening assay which needs observation on the sorted worms over an extended time period.

Our microfluidic diode structure is inspired by the natural locomotive characteristics of *C. elegans*, which adopts an undulatory wave pattern when it moves[223–230]. This wavy motion is generated by dorsal-ventral muscular contractions[223,228]. Interestingly, *C. elegans* are able to adjust the frequency and wavelength of the wavy motion according to its physical surroundings because of their mechanosensitive nature[225,228,235]. Park et al.[228] demonstrated an enhanced locomotion of *C. elegans* in a square array of micro-posts compared to bulk liquid. In their work, worms wound through the posts with different spacing along corresponding diagonal directions in different speeds. The optimized geometry significantly increases L4/young adult locomotion to a frequency of ~2 Hz and a swimming speed of ~1200 μm/s (compared to a frequency of ~1.56 Hz and a swimming speed of ~126 μm/s in bulk fluid). Under such optimal micro-post setting, worms traverse an approximate full wavelength of a sinusoidal waveform when move through two consecutive posts. The post spacing was about the half-wavelength and the

propulsion force generated by the posts leads to the most efficient locomotion compared to all other settings.

Inspired by the locomotive wave pattern of worms, we designed our microfluidic diode featuring a curved section facilitating the worm self-locomotion based on the following two criteria:

1. The curve shape should simulate the estimated sinusoidal locomotion wave and span a half-wavelength.
2. The curved channel length should be approximately equal to half of the body length of the worm.

As reported previously, the L4/young adult worms have an average diameter of around 35 μm[231]. Also, we found that the worm length/diameter ratio is generally around 21 according to Maguire et al.[231] and an online worm database[236]. We start the design with this group of worms and take advantage of this approximate linear relationship between body length and diameter to scale up and down for different groups of worms.

According to Park et al.[228], the wavelength λ for the most efficient locomotion is equal to

$$\lambda = \frac{1200\ \mu m/s}{2\ Hz} = 600\ \mu m.$$

Based on the 1st criterion, our curved channel is designed to span half of λ and to contain four identical arcs with a radius of r (see Fig. 5.7a). This geometry forms an angle of $\alpha = 60°$. Thus, the radius r is

$$\sin(60°) \times 2r = \frac{\lambda}{4} \rightarrow r = 87\ \mu m.$$

Therefore, the channel length $l = 2\pi r \cdot 4\alpha/360° = 364\ \mu m$. Meanwhile, given the empirical body length/diameter ratio of ~21, the worm length is about $35\ um \times 21 = 735\ \mu m$, which is also consistent with the average body length documented in the worm database[236]. As such, the curved channel length is approximately half of the body length of the worm, which satisfies the 2nd criterion.

The 2nd criterion has two benefits: 1. It provides an optimal propulsion force leading to an enhanced locomotion to the greatest extent in conjunction with criterion 1 as discussed before; 2. It ensures a high successful rate of passage for worms within a certain diameter range without blocking the diode. This is because if the middle region of the worm, the largest part of the body, can pass the diode, the whole worm will easily get through the channel (see Fig. 5.7 (b)). On the other hand, if the worm size is too large to pass through the channel, the front part of the worm is still in the curved section and it can help to push the worm backward and get out of the channel.

Compared to the curved channel segment, the straight part does not provide any propulsion force. We designed the length of the straight channel to be around 30~40% of the body length. Therefore, when the worm head arrives at the straight part, the rear portion of the worm is still in contact with the curved surface and is able to push its body forward out of the channel. In contrast, in the situation where worm immobilization is required for further investigation, we designed the straight channel long enough to at least contain the whole worm. Thus, it can completely deprive the worm of the external thrust from the structure and keep the worm still. Together with the tapered shape, despite the minor thrust from the flow, it is able to keep the worm immobilized.

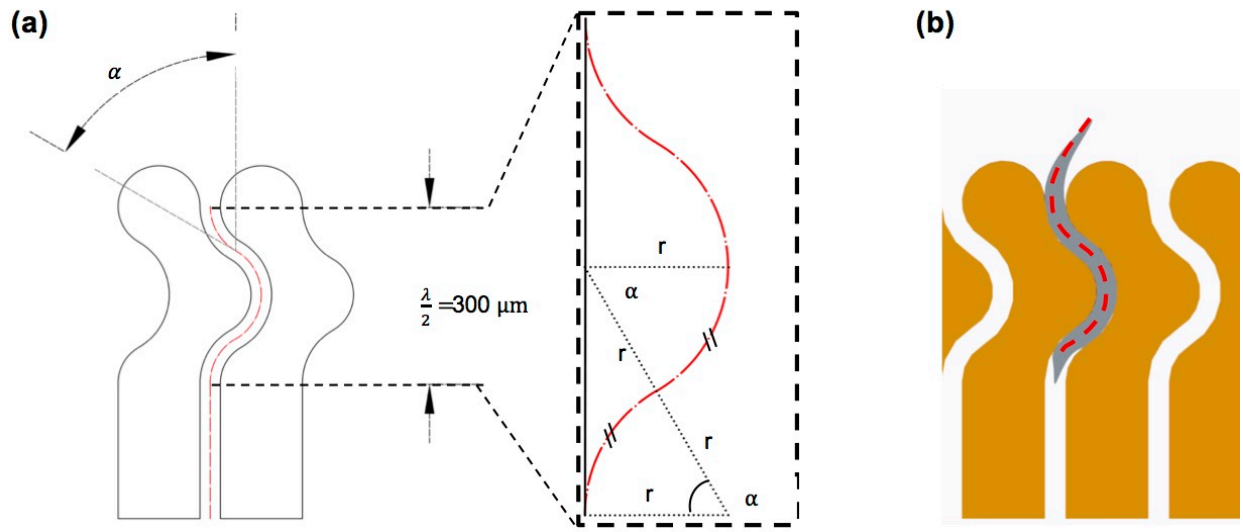

Figure 5.7 Microfluidic diode design principles. (a) The curved section simulates an approximate sinusoidal locomotion wave and spans half of the wavelength. (b) The curved channel length is roughly equal to half of the worm body length.

5.5 Summary

In this chapter, we constructed a microfluidic *C. elegans* diode based on the natural worm locomotion characteristics, allowing for unidirectional passage of *C. elegans* through the structure. A class of microfluidic *C. elegans* sorting and immobilization platforms built upon this diode structure have been designed and demonstrated with great success. The sorting device can achieve a high throughput and separate a wild colony of *C. elegans* into different developmental stages within one operation, which has not been achieved in previously reported microfluidic *C. elegans* sorting techniques. As such, this development provides a practical approach for highly efficient and accurate worm sorting even in the presence of egg clusters and debris. In addition, the platform allows for the well-sorted worms to be collected or immobilized afterwards for subsequent biological assays.

CHAPTER VI

SUMMARY AND OUTLOOK

6.1 Summary

Cell activities in response to mechanical, electrical, and chemical stimuli as well as organism behavior are extremely interesting and puzzling. The further we dig, the more discoveries and subsequent questions we uncover. In this process, technological limitations are one of the main hurdles that prevent researchers from exploring the unknowns. This dissertation presents several innovative microfluidic platforms and acquires some new findings in the fields of cell mechanotransduction, electrical activity, and *C. elegans* sorting.

In Chapters II and III, the investigations on cellular signaling and behavior under different types of mechanical forces were demonstrated. Chapter II revealed a microfluidic stretcher platform through which mechanical stimuli were applied to NAFs and CAFs to study the effects of stress exertion and relaxation on NAF activation and CAF deactivation. The fabrication approach described in this work, different from Huh et al.'s approach, allows for a better control on the device dimension and thus more precise force application to cells. In addition, the stretcher was well characterized and validated through experiments and COMSOL^{TM} modeling, showing an approximately linear relation between the applied vacuum pressure and membrane strain. Using this platform, we demonstrated that stretched NAFs exhibited phenotypes similar to CAFs in terms of depositing organized ECM with aligned fibronectin and directing cancer cell migration, indicating that mechanical stretching plays a key role in NAF activation and CAF genesis. Interestingly, the relaxed CAFs expressed ECM and α-

SMA in a similar manner as NAFs. These evidences showed that CAFs adopt less CAF-like and more NAF-like phenotype upon force relaxation, indicating a potential cancer therapeutic approach targeting tumor stroma. Additionally, this microfluidic stretcher was also employed to study the effect of mechanical stretching in different modes that mimic primary and secondary brain injuries on neuron viability. We found that long-time stretching inflicted more severe damage to neurons than short-time stretching of the same strain did, indicating the secondary brain injury may be more dangerous than the primary one. To understand the effect of mechanical stretching on electrical activity of synapses, a microfluidic stretcher integrated with graphene probes was proposed, allowing for future investigations.

Although a number of theoretical and experimental studies have reported on cell behavior subjected to mechanical stretching on a 2D stretchable membrane, little has been done in a 3D matrix, especially upon compression. Chapter III presented significantly different orientation behavior of NAFs and CAFs in response to 3D compression with a quantitative analysis via a FFT method. More specifically, NAFs reoriented themselves to specific directions upon compression, while CAFs did not exhibit any preferred orientation under compression. To understand this interesting observation, a mathematical model based upon the energy minimization principle was constructed. The model indicated that the largely distinct behaviors can be understood based on the significant difference on inherent contractile stress generated by SFs of NAFs and CAFs. This model was further validated through a series of bioassays. The finding that SFs and inherent cell contractility are deterministic factors in the cellular response to compression in 3D provided new insights into the mechanisms by which cells adjust their orientation to maintain cellular homeostasis.

In addition to cell behaviors in response to mechanical stimuli, electrical activity of neurons upon chemical stimuli are equally captivating to us in view of the vital role of neurons in cognitive functions and the limitations of current technologies. In Chapter IV, a novel microfluidic sensing platform with integrated graphene transistor arrays capable of measuring neuronal activities with ultrahigh spatiotemporal resolution was illustrated. Following the description of device design, characterization, and validation, Chapter IV demonstrated that this platform managed to capture neuron depolarization events upon chemical stimulation in real-time at single spine and synapse level. The platform will be of great use in electrophysiological recording and the study of synapse formation and plasticity at molecular level.

While the above microfluidic platforms for biological investigations span cellular and subcellular scales, in Chapter V a class of microfluidic devices applied to an organsim study were showcased. The design presented in Chapter V is capable of simultaneously sorting worms by size at a throughput of 97 ± 4 worms per minute, and allowing for worm collection or immobilization for further investigations. The key component, a microfluidic diode structure, comprises a curved head and a straight tail, which facilitates worms to enter from the curved end but prevents them from passing from the straight side. This design significantly enhances the efficiency and accuracy of worm sorting at relatively low flow rates, and hence provides a practical approach to sort worms even with the presence of egg clusters and debris. In addition, the well-sorted worms were further immobilized, kept alive and identically orientated, which could facilitate many *C. elegans*-based studies.

6.2 Outlook

Despite the significant progress achieved through microfluidics in this dissertation, there are still abundant open questions that these techniques can address. First, as demonstrated in Chapter II, CAFs facilitate cancer cell migration in a directional manner, while NAFs do not show the same feature; however, NAFs after being stretched have a similar promotive effect on cancer cell migration as CAFs. We also showed CAFs after being relaxed from a pre-stretched state exhibit NAF-like phenotype. However, a piece of puzzle is still missing: will the relaxed CAFs lose the capability of directing cancer cell migration? If this is the case, it indicates a promising anti-cancer application. As such, a future study of co-culturing relaxed CAFs and SCC61 cancer cells in the stretcher platform and recording the pattern of cancer cell movement will be very interesting.

Second, cell mechanotransduction studies in this dissertation focused on cell behavior and signaling alteration upon static mechanical stimuli; meanwhile, how cyclic forces would affect cells differently is equally interesting. The microfluidic stretcher proposed in Chapter II, instead of being connected with a vacuum line, can be connected to a syringe in which the plunger is controlled by a lead crew and nut based linear motion system. The cell phenotype can be analyzed and compared in response to cyclic stretching force with different frequencies, strains, and durations. With these studies, a more detailed picture of cell mechanotransductive behavior could be disclosed. The 3D cell compression setup in Chapter III can also be integrated with cyclic control component, too. Together with a built-in force sensor, the internal cellular force generated to resist external compressive stimulation and to keep cell homeostasis can be quantitatively measured. Although a wealth of experimental tools and theoretical models have been constructed in pursuit of the measurement of cellular forces, such as magnetic bead

cytometry[237], optical tweezers[238,239], cell stretching and shear flow platform[240,241], micropillar arrays[95], AFM, particle tracking microrheology (PTM)[242], and traction force microscopy (TFM)[243]. All of the aforementioned approaches, except PTM, are difficult to examine cell mechanical properties and the generated force by cells in a 3D matrix that is more physiologically relevant compared with 2D substrates[244]. PTM, on the other hand, can be confounded by active intracellular thermal processes because it is based on Brownian motion[245]. Therefore, cell responsive force in a 3D context remains largely elusive. This cell cyclic compression setup will be of great potential to provide perspectives on cell dynamic response in 3D.

Third, the graphene transistor based microfluidic platform illustrated in Chapter IV can be further optimized in terms of the SNR ratio by patterning the graphene film into stripes so as to prevent current from leaking to other electrode pairs. In addition, more locally chemical stimulation is desired to prevent side effects on cells out of the sensing transistor region. This can be realized by delicately arranging separated chemical delivery channel array. Further, the design of the microfluidic stretcher integrated with graphene transistors proposed in Chapter II can be implemented in bioassays to provide insights on the effect of mechanical stimuli on electrical activity of individual synapses.

In summary, although microfluidics has been recognized as a promising tool to address problems in biology and medical fields, there are still a lot of territories to explore and a lot room for applications beyond research. Hopefully, in the near future, the techniques described in this dissertation can expand their impacts to much broader scopes.

REFERENCES

1. Ricca, B. L., Venugopalan, G. & Fletcher, D. A. To pull or be pulled: parsing the multiple modes of mechanotransduction. *Curr. Opin. Cell Biol.* **25,** 558–64 (2013).

2. Galie, P. A. Cellular Mechanotransduction in the Pathogenesis and Treatment of Cardiac Fibrosis. (2011).

3. Jaalouk, D. E. & Lammerding, J. Mechanotransduction gone awry. *Nat. Rev. Mol. Cell Biol.* **10,** 63–73 (2009).

4. Gomez, F. A. *Biological applications of microfluidics*. (Wiley-Interscience, 2008).

5. Scanziani, M. & Häusser, M. Electrophysiology in the age of light. *Nature* **461,** 930–939 (2009).

6. Pagès, S., Côté, D. & De Koninck, P. Optophysiological approach to resolve neuronal action potentials with high spatial and temporal resolution in cultured neurons. *Front. Cell. Neurosci.* **5,** 20 (2011).

7. Jaalouk, D. E. & Lammerding, J. Mechanotransduction gone awry. *Nat. Rev. Mol. Cell Biol.* **10,** 63–73 (2009).

8. Humphrey, J. D., Dufresne, E. R. & Schwartz, M. A. Mechanotransduction and extracellular matrix homeostasis. *Nat. Rev. Mol. Cell Biol.* **15,** 802–812 (2014).

9. Kawashima, Y. *et al.* Mechanotransduction in mouse inner ear hair cells requires transmembrane channel-like genes. *J. Clin. Invest.* **121,** 4796–809 (2011).

10. Huang, C. & Ogawa, R. Mechanotransduction in bone repair and regeneration. *FASEB J.* **24,** 3625–32 (2010).

11. Burkholder, T. J. Mechanotransduction in skeletal muscle. *Front. Biosci.* **12,** 174–91 (2007).

12. Hahn, C. & Schwartz, M. A. Mechanotransduction in vascular physiology and atherogenesis. *Nat. Rev. Mol. Cell Biol.* **10,** 53–62 (2009).

13. Wozniak, M. A. & Chen, C. S. Mechanotransduction in development: a growing role for contractility. *Nat. Rev. Mol. Cell Biol.* **10,** 34–43 (2009).

14. Brosig, M. Mechanotransduction in Fibroblasts. (2011).

15. Ostrow, L. W. & Sachs, F. Mechanosensation and endothelin in astrocytes--hypothetical roles in CNS pathophysiology. *Brain Res. Brain Res. Rev.* **48,** 488–508 (2005).

16. Vollrath, M. A., Kwan, K. Y. & Corey, D. P. The micromachinery of mechanotransduction in hair cells. *Annu. Rev. Neurosci.* **30,** 339–65 (2007).

17. Paszek, M. J. *et al.* Tensional homeostasis and the malignant phenotype. *Cancer Cell* **8,** 241–

54 (2005).

18. Wong, V. W., Longaker, M. T. & Gurtner, G. C. Soft tissue mechanotransduction in wound healing and fibrosis. *Semin. Cell Dev. Biol.* **23,** 981–6 (2012).

19. Rustad, K. C., Wong, V. W. & Gurtner, G. C. The role of focal adhesion complexes in fibroblast mechanotransduction during scar formation. *Differentiation.* **86,** 87–91 (2013).

20. Knies, Y., Bernd, A., Kaufmann, R., Bereiter-Hahn, J. & Kippenberger, S. Mechanical stretch induces clustering of beta1-integrins and facilitates adhesion. *Exp. Dermatol.* **15,** 347–55 (2006).

21. Connelly, J. T., Vanderploeg, E. J., Mouw, J. K., Wilson, C. G. & Levenston, M. E. Tensile loading modulates bone marrow stromal cell differentiation and the development of engineered fibrocartilage constructs. *Tissue Eng. Part A* **16,** 1913–23 (2010).

22. Polacheck, W. J., Li, R., Uzel, S. G. M. & Kamm, R. D. Microfluidic platforms for mechanobiology. *Lab Chip* **13,** 2252–67 (2013).

23. Tse, J. M. Compressive Stress Enhances Coordinated Migration of Mammary Carcinoma Cells by by. *Chem. Eng.* (2010).

24. Kim, D.-H., Wong, P. K., Park, J., Levchenko, A. & Sun, Y. Microengineered platforms for cell mechanobiology. *Annu. Rev. Biomed. Eng.* **11,** 203–33 (2009).

25. Guck, J. *et al.* The optical stretcher: a novel laser tool to micromanipulate cells. *Biophys. J.* **81,** 767–84 (2001).

26. Lincoln, B., Wottawah, F., Schinkinger, S., Ebert, S. & Guck, J. High-throughput rheological measurements with an optical stretcher. *Methods Cell Biol.* **83,** 397–423 (2007).

27. Guck, J. *et al.* The optical stretcher: a novel laser tool to micromanipulate cells. *Biophys. J.* **81,** 767–84 (2001).

28. Guck, J. *et al.* Optical deformability as an inherent cell marker for testing malignant transformation and metastatic competence. *Biophys. J.* **88,** 3689–98 (2005).

29. De Vlaminck, I. & Dekker, C. Recent Advances in Magnetic Tweezers. *Annu. Rev. Biophys.* **41,** 453–472 (2012).

30. Zhao, R., Boudou, T., Wang, W. G., Chen, C. S. & Reich, D. H. Decoupling cell and matrix mechanics in engineered microtissues using magnetically actuated microcantilevers. *Adv. Mater.* **25,** 1699–1705 (2013).

31. Huh, D. *et al.* Reconstituting organ-level lung functions on a chip. *Science* **328,** 1662–8 (2010).

32. Ao, M. *et al.* Stretching Fibroblasts Remodels Fibronectin and Alters Cancer Cell Migration. *Sci. Rep.* **5,** 8334 (2015).

33. Park, J. S. *et al.* Differential effects of equiaxial and uniaxial strain on mesenchymal stem

cells. *Biotechnol. Bioeng.* **88,** 359–68 (2004).

34. Wang, D. *et al.* A stretching device for imaging real-time molecular dynamics of live cells adhering to elastic membranes on inverted microscopes during the entire process of the stretch. *Integr. Biol. (Camb).* **2,** 288–93 (2010).

35. Kim, H. J., Huh, D., Hamilton, G. & Ingber, D. E. Human gut-on-a-chip inhabited by microbial flora that experiences intestinal peristalsis-like motions and flow. *Lab Chip* **12,** 2165 (2012).

36. Kaunas, R., Nguyen, P., Usami, S. & Chien, S. Cooperative effects of Rho and mechanical stretch on stress fiber organization. *Proc. Natl. Acad. Sci. U. S. A.* **102,** 15895–900 (2005).

37. Kamotani, Y. *et al.* Individually programmable cell stretching microwell arrays actuated by a Braille display. *Biomaterials* **29,** 2646–55 (2008).

38. Winston, F. K., Macarak, E. J., Gorfien, S. F. & Thibault, L. E. A system to reproduce and quantify the biomechanical environment of the cell. *J Appl Physiol* **67,** 397–405 (1989).

39. Simmons, C. S. *et al.* Integrated strain array for cellular mechanobiology studies. *J. Micromech. Microeng.* **21,** 54016–54025 (2011).

40. Tremblay, D., Chagnon-Lessard, S., Mirzaei, M., Pelling, A. E. & Godin, M. A microscale anisotropic biaxial cell stretching device for applications in mechanobiology. *Biotechnol. Lett.* **36,** 657–65 (2014).

41. Neidlinger-Wilke, C., Grood, E. S., Wang JH-C, Brand, R. a & Claes, L. Cell alignment is induced by cyclic changes in cell length: studies of cells grown in cyclically stretched substrates. *J. Orthop. Res.* **19,** 286–93 (2001).

42. Wang, J. H., Goldschmidt-Clermont, P. & Yin, F. C. Contractility affects stress fiber remodeling and reorientation of endothelial cells subjected to cyclic mechanical stretching. *Ann. Biomed. Eng.* **28,** 1165–71 (2000).

43. Livne, A., Bouchbinder, E. & Geiger, B. Cell reorientation under cyclic stretching. *Nat. Commun.* **5,** 3938 (2014).

44. Krishnan, R. *et al.* Fluidization, resolidification, and reorientation of the endothelial cell in response to slow tidal stretches. *Am. J. Physiol. Cell Physiol.* **303,** C368-75 (2012).

45. Iba, T. & Sumpio, B. E. Morphological response of human endothelial cells subjected to cyclic strain in vitro. *Microvasc. Res.* **42,** 245–254 (1991).

46. Zhao, L., Sang, C., Yang, C. & Zhuang, F. Effects of stress fiber contractility on uniaxial stretch guiding mitosis orientation and stress fiber alignment. *J. Biomech.* **44,** 2388–94 (2011).

47. Neidlinger-Wilke, C., Wilke, H. J. & Claes, L. Cyclic stretching of human osteoblasts affects proliferation and metabolism: a new experimental method and its application. *J. Orthop. Res.* **12,** 70–8 (1994).

48. Dartsch, P. C. & Hämmerle, H. Orientation response of arterial smooth muscle cells to mechanical stimulation. *Eur. J. Cell Biol.* **41,** 339–46 (1986).

49. Wang, H., Ip, W., Boissy, R. & Grood, E. S. Cell orientation response to ciclically deformed substrates:experimental validation of cell model. *J. Biomech.* **28,** 1543–1552 (1995).

50. Morita, Y., Watanabe, S., Ju, Y. & Yamamoto, S. In vitro experimental study for the determination of cellular axial strain threshold and preferential axial strain from cell orientation behavior in a non-uniform deformation field. *Cell Biochem. Biophys.* **67,** 1249–59 (2013).

51. Yang, G., Crawford, R. C. & Wang, J. H.-C. Proliferation and collagen production of human patellar tendon fibroblasts in response to cyclic uniaxial stretching in serum-free conditions. *J. Biomech.* **37,** 1543–50 (2004).

52. Zhang, L., Kahn, C. J. F., Chen, H.-Q., Tran, N. & Wang, X. Effect of uniaxial stretching on rat bone mesenchymal stem cell: orientation and expressions of collagen types I and III and tenascin-C. *Cell Biol. Int.* **32,** 344–52 (2008).

53. Wang, J. H.-C. *et al.* Cyclic mechanical stretching of human tendon fibroblasts increases the production of prostaglandin E2 and levels of cyclooxygenase expression: a novel in vitro model study. *Connect. Tissue Res.* **44,** 128–33 (2003).

54. Henshaw, D. R., Attia, E., Bhargava, M. & Hannafin, J. A. Canine ACL fibroblast integrin expression and cell alignment in response to cyclic tensile strain in three-dimensional collagen gels. *J. Orthop. Res.* **24,** 481–90 (2006).

55. Yu, H.-S., Kim, J.-J., Kim, H.-W., Lewis, M. P. & Wall, I. Impact of mechanical stretch on the cell behaviors of bone and surrounding tissues. *J. Tissue Eng.* **6,** 2041731415618342 (2015).

56. He, Y., Macarak, E. J., Korostoff, J. M. & Howard, P. S. Compression and tension: differential effects on matrix accumulation by periodontal ligament fibroblasts in vitro. *Connect. Tissue Res.* **45,** 28–39 (2004).

57. El-Awady, A. R. *et al.* Human periodontal ligament fibroblast responses to compression in chronic periodontitis. *J. Clin. Periodontol.* **40,** 661–71 (2013).

58. Kwok, C. B. *et al.* Compression-induced alignment and elongation of human mesenchymal stem cell (hMSC) in 3D collagen constructs is collagen concentration dependent. *J. Biomed. Mater. Res. - Part A* **101 A,** 1716–1725 (2013).

59. Jain, R. K., Martin, J. D. & Stylianopoulos, T. The role of mechanical forces in tumor growth and therapy. *Annu. Rev. Biomed. Eng.* **16,** 321–46 (2014).

60. Mouw, J. K., Connelly, J. T., Wilson, C. G., Michael, K. E. & Levenston, M. E. Dynamic compression regulates the expression and synthesis of chondrocyte-specific matrix molecules in bone marrow stromal cells. *Stem Cells* **25,** 655–663 (2007).

61. Terraciano, V. *et al.* Differential response of adult and embryonic mesenchymal progenitor

cells to mechanical compression in hydrogels. *Stem Cells* **25,** 2730–2738 (2007).

62. Park, S.-H. *et al.* An electromagnetic compressive force by cell exciter stimulates chondrogenic differentiation of bone marrow-derived mesenchymal stem cells. *Tissue Eng.* **12,** 3107–3117 (2006).

63. Si, F., Li, B., Margolin, W. & Sun, S. X. Bacterial growth and form under mechanical compression. *Sci. Rep.* **5,** 11367 (2015).

64. Au-Yeung, K. L., Sze, K. Y., Sham, M. H. & Chan, B. P. Development of a micromanipulator-based loading device for mechanoregulation study of human mesenchymal stem cells in three-dimensional collagen constructs. *Tissue Eng. Part C. Methods* **16,** 93–107 (2010).

65. Girton, T. S., Barocas, V. H. & Tranquillo, R. T. Confined compression of a tissue-equivalent: collagen fibril and cell alignment in response to anisotropic strain. *J. Biomech. Eng.* **124,** 568–75 (2002).

66. Girton, T. S., Barocas, V. H. & Tranquillo, R. T. Confined Compression of a Tissue-Equivalent: Collagen Fibril and Cell Alignment in Response to Anisotropic Strain. *J. Biomech. Eng.* **124,** 568 (2002).

67. Altman, G. H. *et al.* Cell differentiation by mechanical stress. *FASEB J.* **16,** 270–2 (2002).

68. Kanzaki, H., Chiba, M., Shimizu, Y. & Mitani, H. Periodontal ligament cells under mechanical stress induce osteoclastogenesis by receptor activator of nuclear factor kappaB ligand up-regulation via prostaglandin E2 synthesis. *J. Bone Miner. Res.* **17,** 210–20 (2002).

69. Demou, Z. N. Gene expression profiles in 3D tumor analogs indicate compressive strain differentially enhances metastatic potential. *Ann. Biomed. Eng.* **38,** 3509–20 (2010).

70. Mauck, R. L., Byers, B. a., Yuan, X. & Tuan, R. S. Regulation of cartilaginous ECM gene transcription by chondrocytes and MSCs in 3D culture in response to dynamic loading. *Biomech. Model. Mechanobiol.* **6,** 113–125 (2007).

71. Cheng, G., Tse, J., Jain, R. K. & Munn, L. L. Micro-environmental mechanical stress controls tumor spheroid size and morphology by suppressing proliferation and inducing apoptosis in cancer cells. *PLoS One* **4,** e4632 (2009).

72. Goga, Y., Chiba, M., Shimizu, Y. & Mitani, H. Compressive force induces osteoblast apoptosis via caspase-8. *J. Dent. Res.* **85,** 240–244 (2006).

73. Huang, C.-Y. C., Hagar, K. L., Frost, L. E., Sun, Y. & Cheung, H. S. Effects of cyclic compressive loading on chondrogenesis of rabbit bone-marrow derived mesenchymal stem cells. *Stem Cells* **22,** 313–23 (2004).

74. Huang, C.-Y. C., Reuben, P. M. & Cheung, H. S. Temporal expression patterns and corresponding protein inductions of early responsive genes in rabbit bone marrow-derived mesenchymal stem cells under cyclic compressive loading. *Stem Cells* **23,** 1113–1121 (2005).

75. Owan, I. *et al.* Mechanotransduction in bone: osteoblasts are more responsive to fluid forces than mechanical strain. *Am. J. Physiol.* **273,** C810-5 (1997).

76. Li, G. *et al.* Mechanical compressive force inhibits adipogenesis of adipose stem cells. *Cell Prolif.* **46,** 586–594 (2013).

77. Lu, D. & Kassab, G. S. Role of shear stress and stretch in vascular mechanobiology. *J. R. Soc. Interface* **8,** 1379–85 (2011).

78. Chiu, J.-J. & Chien, S. Effects of disturbed flow on vascular endothelium: pathophysiological basis and clinical perspectives. *Physiol. Rev.* **91,** 327–87 (2011).

79. Andrews, A. M., Jaron, D., Buerk, D. G., Kirby, P. L. & Barbee, K. a. Direct, real-time measurement of shear stress-induced nitric oxide produced from endothelial cells in vitro. *Nitric Oxide - Biol. Chem.* **23,** 335–342 (2010).

80. Leskov, V. P. & Zatevakhin, I. I. The role of the immune system in the pathogenesis of atherosclerosis. *Angiol. Sosud. Khir.* **11,** 9–14 (2005).

81. Nerem, R. M. Shear force and its effect on cell structure and function. *ASGSB Bull.* **4,** 87–94 (1991).

82. Hsu, P. P. *et al.* Effects of flow patterns on endothelial cell migration into a zone of mechanical denudation. *Biochem. Biophys. Res. Commun.* **285,** 751–9 (2001).

83. Li, Y.-S. J., Haga, J. H. & Chien, S. Molecular basis of the effects of shear stress on vascular endothelial cells. *J. Biomech.* **38,** 1949–1971 (2005).

84. Varma, S. & Voldman, J. A cell-based sensor of fluid shear stress for microfluidics. *Lab Chip* **15,** 1563–1573 (2015).

85. Shav, D., Gotlieb, R., Zaretsky, U., Elad, D. & Einav, S. Wall shear stress effects on endothelial-endothelial and endothelial-smooth muscle cell interactions in tissue engineered models of the vascular wall. *PLoS One* **9,** e88304 (2014).

86. Warabi, E. *et al.* Effect on endothelial cell gene expression of shear stress, oxygen concentration, and low-density lipoprotein as studied by a novel flow cell culture system. *Free Radic. Biol. Med.* **37,** 682–694 (2004).

87. Warabi, E. *et al.* Shear stress stabilizes NF-E2-related factor 2 and induces antioxidant genes in endothelial cells: Role of reactive oxygen/nitrogen species. *Free Radic. Biol. Med.* **42,** 260–269 (2007).

88. Wang, J., Heo, J. & Hua, S. Z. Spatially resolved shear distribution in microfluidic chip for studying force transduction mechanisms in cells. *Lab Chip* **10,** 235–239 (2010).

89. Galie, P., van Oosten, A., Chen, C. S. & Janmey, P. Application of multiple levels of fluid shear stress to endothelial cells plated on polyacrylamide gels. *Lab Chip* **15,** 1205–1212 (2015).

90. Dasbiswas, K., Majkut, S., Discher, D. E. & Safran, S. a. Substrate stiffness-modulated

registry phase correlations in cardiomyocytes map structural order to coherent beating. *Nat. Commun.* **6,** 1–8 (2015).

91. Guo, W., Frey, M. T., Burnham, N. A. & Wang, Y. Substrate rigidity regulates the formation and maintenance of tissues. *Biophys. J.* **90,** 2213–20 (2006).

92. Lo, C. M., Wang, H. B., Dembo, M. & Wang, Y. L. Cell movement is guided by the rigidity of the substrate. *Biophys. J.* **79,** 144–52 (2000).

93. Liou, Y.-R. *et al.* Substrate stiffness regulates filopodial activities in lung cancer cells. *PLoS One* **9,** e89767 (2014).

94. Eroshenko, N., Ramachandran, R., Yadavalli, V. K. & Rao, R. R. Effect of substrate stiffness on early human embryonic stem cell differentiation. *J. Biol. Eng.* **7,** 7 (2013).

95. Fu, J. *et al.* Mechanical regulation of cell function with geometrically modulated elastomeric substrates. *Nat. Methods* **7,** 733–736 (2010).

96. Tan, J. L. *et al.* Cells lying on a bed of microneedles: an approach to isolate mechanical force. *Proc. Natl. Acad. Sci. U. S. A.* **100,** 1484–1489 (2003).

97. Ghibaudo, M. *et al.* Traction forces and rigidity sensing regulate cell functions. *Soft Matter* **4,** 1836 (2008).

98. Stiles, J. & Jernigan, T. L. The basics of brain development. *Neuropsychol. Rev.* **20,** 327–48 (2010).

99. Millet, L. J. & Gillette, M. U. Over a century of neuron culture: from the hanging drop to microfluidic devices. *Yale J. Biol. Med.* **85,** 501–21 (2012).

100. Shi, M. *et al.* Glia co-culture with neurons in microfluidic platforms promotes the formation and stabilization of synaptic contacts. *Lab Chip* **13,** 3008 (2013).

101. Beck, H. & Yaari, Y. Plasticity of intrinsic neuronal properties in CNS disorders. *Nat. Rev. Neurosci.* **9,** 357–69 (2008).

102. Takeuchi, T., Duszkiewicz, A. J. & Morris, R. G. M. The synaptic plasticity and memory hypothesis: encoding, storage and persistence. *Philos. Trans. R. Soc. Lond. B. Biol. Sci.* **369,** 20130288 (2014).

103. Scanziani, M. & Häusser, M. Electrophysiology in the age of light. *Nature* **461,** 930–939 (2009).

104. Rojas, R. *Neural Networks: A Systematic Introduction*. (Springer Science & Business Media, 2013).

105. NEHER, E. & SAKMANN, B. Single-channel currents recorded from membrane of denervated frog muscle fibres. *Nature* **260,** 799–802 (1976).

106. Yajuan, X., Xin, L. & Zhiyuan, L. A comparison of the performance and application differences between manual and automated patch-clamp techniques. *Curr. Chem. Genomics* **6,**

87–92 (2012).

107. Obien, M. E. J., Deligkaris, K., Bullmann, T., Bakkum, D. J. & Frey, U. Revealing neuronal function through microelectrode array recordings. *Front. Neurosci.* **9,** 423 (2015).

108. Fertig, N., Blick, R. H. & Behrends, J. C. Whole cell patch clamp recording performed on a planar glass chip. *Biophys. J.* **82,** 3056–62 (2002).

109. Zhao, Y. *et al.* Patch clamp technique: review of the current state of the art and potential contributions from nanoengineering. *Proc. Inst. Mech. Eng. Part N J. Nanoeng. Nanosyst.* **222,** 1–11 (2008).

110. Marshall, J. D. & Schnitzer, M. J. Optical strategies for sensing neuronal voltage using quantum dots and other semiconductor nanocrystals. *ACS Nano* **7,** 4601–4609 (2013).

111. Ryglewski, S., Pflueger, H. J. & Duch, C. Expanding the neuron's calcium signaling repertoire: intracellular calcium release via voltage-induced PLC and IP3R activation. *PLoS Biol.* **5,** e66 (2007).

112. Müller, J. *et al.* High-resolution CMOS MEA platform to study neurons at subcellular, cellular, and network levels. *Lab Chip* **15,** 2767–2780 (2015).

113. Berdondini, L. *et al.* Active pixel sensor array for high spatio-temporal resolution electrophysiological recordings from single cell to large scale neuronal networks. *Lab Chip* **9,** 2644 (2009).

114. Folch, A. *Introduction to BioMEMS*. (CRC Press, 2012).

115. Beebe, D. J., Mensing, G. a & Walker, G. M. Physics and applications of microfluidics in biology. *Annu. Rev. Biomed. Eng.* **4,** 261–286 (2002).

116. Sia, S. K. & Whitesides, G. M. Microfluidic devices fabricated in poly(dimethylsiloxane) for biological studies. *Electrophoresis* **24,** 3563–3576 (2003).

117. Unger, M. A., Chou, H.-P., Thorsen, T., Scherer, A. & Quake, S. R. Monolithic Microfabricated Valves and Pumps by Multilayer Soft Lithography. *Science (80-.).* **288,** (2000).

118. Regehr, K. J. *et al.* Biological implications of polydimethylsiloxane-based microfluidic cell culture. *Lab Chip* **9,** 2132–9 (2009).

119. Abate, A. R., Lee, D., Do, T., Holtze, C. & Weitz, D. A. Glass coating for PDMS microfluidic channels by sol–gel methods. *Lab Chip* **8,** 516 (2008).

120. Zhou, J., Ellis, A. V. & Voelcker, N. H. Recent developments in PDMS surface modification for microfluidic devices. *Electrophoresis* **31,** 2–16 (2010).

121. Zhang, Y., Ishida, M., Kazoe, Y., Sato, Y. & Miki, N. Water-vapor permeability control of PDMS by the dispersion of collagen powder. *IEEJ Trans. Electr. Electron. Eng.* **4,** 442–449 (2009).

122. Kalluri, R. & Zeisberg, M. Fibroblasts in cancer. *Nat. Rev. Cancer* **6,** 392–401 (2006).

123. Augsten, M. Cancer-associated fibroblasts as another polarized cell type of the tumor microenvironment. *Front. Oncol.* **4,** 62 (2014).

124. CDC | Get the Facts | Traumatic Brain Injury | Injury Center. Available at: http://www.cdc.gov/traumaticbraininjury/get_the_facts.html. (Accessed: 19th October 2015)

125. Slemmer, J. E. *et al.* Causal role of apoptosis-inducing factor for neuronal cell death following traumatic brain injury. *Am. J. Pathol.* **173,** 1795–805 (2008).

126. Werner, C. & Engelhard, K. Pathophysiology of traumatic brain injury. *Br. J. Anaesth.* **99,** 4–9 (2007).

127. Hemorrhage, T. S. Traumatic Brain Injury (TBI). 1–7

128. Xia, Y. & Whitesides, G. M. Soft Lithography. *Angew. Chemie Int. Ed.* **37,** 550–575 (1998).

129. Hsu, C.-H., Chen, C. & Folch, A. 'Microcanals' for micropipette access to single cells in microfluidic environments. *Lab Chip* **4,** 420–4 (2004).

130. Gates, B. D., Xu, Q., Love, J. C., Wolfe, D. B. & Whitesides, G. M. Unconventional Nanofabrication. *Annu. Rev. Mater. Res.* **34,** 339–372 (2004).

131. Brown, X. Q., Ookawa, K. & Wong, J. Y. Evaluation of polydimethylsiloxane scaffolds with physiologically-relevant elastic moduli: interplay of substrate mechanics and surface chemistry effects on vascular smooth muscle cell response. *Biomaterials* **26,** 3123–3129 (2005).

132. Choi, K. M. & Rogers, J. A. A photocurable poly(dimethylsiloxane) chemistry designed for soft lithographic molding and printing in the nanometer regime. *J. Am. Chem. Soc.* **125,** 4060–1 (2003).

133. Gray, D. S., Tien, J. & Chen, C. S. Repositioning of cells by mechanotaxis on surfaces with micropatterned Young's modulus. *J. Biomed. Mater. Res. A* **66,** 605–14 (2003).

134. Liu, M., Sun, J., Sun, Y., Bock, C. & Chen, Q. Thickness-dependent mechanical properties of polydimethylsiloxane membranes. *J. Micromechanics Microengineering* **19,** 35028 (2009).

135. Olumi, A. F. *et al.* Carcinoma-associated Fibroblasts Direct Tumor Progression of Initiated Human Prostatic Epithelium. *Cancer Res.* **59,** 5002–5011 (1999).

136. Zheng, L.-H., Cai, F.-F., Ge, I., Biskup, E. & Cheng, Z.-P. Stromal fibroblast activation and their potential association with uterine fibroids (Review). *Oncol. Lett.* **8,** 479–486 (2014).

137. Maller, O., DuFort, C. C. & Weaver, V. M. YAP forces fibroblasts to feel the tension. *Nat. Cell Biol.* **15,** 570–2 (2013).

138. Friedl, P. & Gilmour, D. Collective cell migration in morphogenesis, regeneration and cancer. *Nat. Rev. Mol. Cell Biol.* **10,** 445–57 (2009).

139. De, R., Zemel, A. & Safran, S. A. Dynamics of cell orientation. *Nat. Phys.* **3,** 655–659 (2007).

140. De, R. & Safran, S. A. Dynamical theory of active cellular response to external stress. *Phys. Rev. E. Stat. Nonlin. Soft Matter Phys.* **78,** 31923 (2008).

141. Pirentis, A. P., Peruski, E., Iordan, A. L. & Stamenović, D. A Model for Stress Fiber Realignment Caused by Cytoskeletal Fluidization During Cyclic Stretching. *Cell. Mol. Bioeng.* **4,** 67–80 (2011).

142. Li, Y. *et al.* Engineering cell alignment in vitro. *Biotechnol. Adv.* **32,** 347–65

143. Burridge, K. & Wittchen, E. S. The tension mounts: stress fibers as force-generating mechanotransducers. *J. Cell Biol.* **200,** 9–19 (2013).

144. García, J. R. & García, A. J. Cellular mechanotransduction: sensing rigidity. *Nat. Mater.* **13,** 539–40 (2014).

145. Lazopoulos, K. a. & Pirentis, a. Substrate stretching and reorganization of stress fibers as a finite elasticity problem. *Int. J. Solids Struct.* **44,** 8285–8296 (2007).

146. Petroll, W. M., Cavanagh, H. D., Barry, P., Andrews, P. & Jester, J. V. Quantitative analysis of stress fiber orientation during corneal wound contraction. *J. Cell Sci.* **104 (Pt 2,** 353–63 (1993).

147. Kaunas, R. & Hsu, H.-J. A kinematic model of stretch-induced stress fiber turnover and reorientation. *J. Theor. Biol.* **257,** 320–30 (2009).

148. Gavara, N., Roca-Cusachs, P., Sunyer, R., Farré, R. & Navajas, D. Mapping cell-matrix stresses during stretch reveals inelastic reorganization of the cytoskeleton. *Biophys. J.* **95,** 464–71 (2008).

149. Wang, J. H. Substrate deformation determines actin cytoskeleton reorganization: A mathematical modeling and experimental study. *J. Theor. Biol.* **202,** 33–41 (2000).

150. Qian, J., Liu, H., Lin, Y., Chen, W. & Gao, H. A mechanochemical model of cell reorientation on substrates under cyclic stretch. *PLoS One* **8,** e65864 (2013).

151. Stamenović, D., Lazopoulos, K. A., Pirentis, A. & Suki, B. Mechanical Stability Determines Stress Fiber and Focal Adhesion Orientation. *Cell. Mol. Bioeng.* **2,** 475–485 (2009).

152. Eastwood, M., Mudera, V. C., McGrouther, D. A. & Brown, R. A. Effect of precise mechanical loading on fibroblast populated collagen lattices: morphological changes. *Cell Motil. Cytoskeleton* **40,** 13–21 (1998).

153. Riehl, B. D., Park, J.-H., Kwon, I. K. & Lim, J. Y. Mechanical stretching for tissue engineering: two-dimensional and three-dimensional constructs. *Tissue Eng. Part B. Rev.* **18,** 288–300 (2012).

154. Foolen, J., Deshpande, V. S., Kanters, F. M. W. & Baaijens, F. P. T. The influence of matrix integrity on stress-fiber remodeling in 3D. *Biomaterials* **33,** 7508–18 (2012).

155. Tse, J. M. *et al.* Mechanical compression drives cancer cells toward invasive phenotype. *Proc. Natl. Acad. Sci. U. S. A.* **109,** 911–6 (2012).

156. Kwok, C. B. *et al.* Compression-induced alignment and elongation of human mesenchymal stem cell (hMSC) in 3D collagen constructs is collagen concentration dependent. *J. Biomed. Mater. Res. A* **101,** 1716–25 (2013).

157. Shachar, M., Benishti, N. & Cohen, S. Effects of mechanical stimulation induced by compression and medium perfusion on cardiac tissue engineering. *Biotechnol. Prog.* **28,** 1551–9

158. Ao, M. *et al.* Cross-talk between paracrine-acting cytokine and chemokine pathways promotes malignancy in benign human prostatic epithelium. *Cancer Res.* **67,** 4244–53 (2007).

159. Yang, L. *et al.* Biomechanics of cell reorientation in a three-dimensional matrix under compression. *Exp. Cell Res.* **350,** 1–14 (2016).

160. Ayres, C. *et al.* Modulation of anisotropy in electrospun tissue-engineering scaffolds: Analysis of fiber alignment by the fast Fourier transform. *Biomaterials* **27,** 5524–34 (2006).

161. Alexander, J. K., Fuss, B. & Colello, R. J. Electric field-induced astrocyte alignment directs neurite outgrowth. *Neuron Glia Biol.* **2,** 93–103 (2006).

162. Achilli, M. & Mantovani, D. Tailoring mechanical properties of collagen-based scaffolds for vascular tissue engineering: The effects of pH, temperature and ionic strength on gelation. *Polymers (Basel).* **2,** 664–680 (2010).

163. Roeder, B. A., Kokini, K., Sturgis, J. E., Robinson, J. P. & Voytik-Harbin, S. L. Tensile Mechanical Properties of Three-Dimensional Type I Collagen Extracellular Matrices With Varied Microstructure. *J. Biomech. Eng.* **124,** 214 (2002).

164. Walcott, S. & Sun, S. X. A mechanical model of actin stress fiber formation and substrate elasticity sensing in adherent cells. *Proc. Natl. Acad. Sci. U. S. A.* **107,** 7757–62 (2010).

165. Kang, J. *et al.* Response of an actin filament network model under cyclic stretching through a coarse grained Monte Carlo approach. *J. Theor. Biol.* **274,** 109–19 (2011).

166. Shao, Y., Mann, J. M., Chen, W. & Fu, J. Global architecture of the F-actin cytoskeleton regulates cell shape-dependent endothelial mechanotransduction. *Integr. Biol. (Camb).* **6,** 300–11 (2014).

167. Çengel, Y. *Fundamentals of thermal-fluid sciences*. (McGraw-Hill Higher Education, 2012).

168. Tilney, L. G. & Tilney, M. S. The actin filament content of hair cells of the bird cochlea is nearly constant even though the length, width, and number of stereocilia vary depending on the hair cell location. *J. Cell Biol.* **107,** 2563–74 (1988).

169. Hsu, H.-J., Lee, C.-F., Locke, A., Vanderzyl, S. Q. & Kaunas, R. Stretch-induced stress fiber remodeling and the activations of JNK and ERK depend on mechanical strain rate, but not FAK. *PLoS One* **5,** e12470 (2010).

170. Eastwood, M., Mudera, V. C., McGrouther, D. a. & Brown, R. a. Effect of precise mechanical loading on fibroblast populated collagen lattices: Morphological changes. *Cell Motil. Cytoskeleton* **40,** 13–21 (1998).

171. Mao, Y., Keller, E. T., Garfield, D. H., Shen, K. & Wang, J. Stromal cells in tumor microenvironment and breast cancer. *Cancer Metastasis Rev.* **32,** 303–15 (2013).

172. Madar, S. *et al.* Modulated expression of WFDC1 during carcinogenesis and cellular senescence. *Carcinogenesis* **30,** 20–7 (2009).

173. Gabbiani, G. The myofibroblast in wound healing and fibrocontractive diseases. *J. Pathol.* **200,** 500–3 (2003).

174. Hinz, B. Masters and servants of the force: the role of matrix adhesions in myofibroblast force perception and transmission. *Eur. J. Cell Biol.* **85,** 175–81 (2006).

175. Liu, X. D. *et al.* Persistence of TGF-beta1 induction of increased fibroblast contractility. *Vitr. Cell. Dev. Biol.* **37,** 193–201 (2001).

176. Lijnen, P., Petrov, V., Rumilla, K. & Fagard, R. Transforming growth factor-beta 1 promotes contraction of collagen gel by cardiac fibroblasts through their differentiation into myofibroblasts. *Methods Find. Exp. Clin. Pharmacol.* **25,** 79–86 (2003).

177. Ura, H. *et al.* Effects of transforming growth factor-á released from gastric carcinoma cells on the conreaction of collagen-matrix gels containing fibroblasts. *Cancer Res.* **51,** 3550–3554 (1991).

178. Tojkander, S., Gateva, G. & Lappalainen, P. Actin stress fibers--assembly, dynamics and biological roles. *J. Cell Sci.* **125,** 1855–64 (2012).

179. Nagayama, K., Kimura, Y., Makino, N. & Matsumoto, T. Strain waveform dependence of stress fiber reorientation in cyclically stretched osteoblastic cells: effects of viscoelastic compression of stress fibers. *Am. J. Physiol. Cell Physiol.* **302,** C1469-78 (2012).

180. Mow, V. C. & Huiskes, R. *Basic orthopaedic biomechanics & mechano-biology*. (Lippincott Williams & Wilkins, 2005).

181. Nagayama, K., Kimura, Y., Makino, N. & Matsumoto, T. Strain waveform dependence of stress fiber reorientation in cyclically stretched osteoblastic cells: effects of viscoelastic compression of stress fibers. *Am. J. Physiol. Cell Physiol.* **302,** C1469-78 (2012).

182. Tse, J. M. *et al.* From the Cover: Mechanical compression drives cancer cells toward invasive phenotype. *Proc. Natl. Acad. Sci.* **109,** 911–916 (2012).

183. Yuste, R. Electrical Compartmentalization in Dendritic Spines. *Annu. Rev. Neurosci.* **36,** 429–449 (2013).

184. Trommershäuser, J., Schneggenburger, R., Zippelius, A. & Neher, E. Heterogeneous Presynaptic Release Probabilities: Functional Relevance for Short-Term Plasticity. *Biophys. J.* **84,** 1563–1579 (2003).

185. Li, X. *et al.* Large-area synthesis of high-quality and uniform graphene films on copper foils. *Science* **324,** 1312–4 (2009).

186. Li, X. *et al.* Transfer of large-area graphene films for high-performance transparent conductive electrodes. *Nano Lett.* **9,** 4359–63 (2009).

187. Jean, L. *et al.* The Rho family GEF Asef2 regulates cell migration in three dimensional (3D) collagen matrices through myosin II. *Cell Adh. Migr.* **8,** 460–467 (2014).

188. Brown, J. A. *et al.* Metabolic consequences of interleukin-6 challenge in developing neurons and astroglia. *J. Neuroinflammation* **11,** 183 (2014).

189. Brewer, B. *DEVELOPMENT OF MICROFLUIDIC CELL CULTURE PLATFORMS FOR INVESTIGATING CELLULAR PHENOMENA*. (2015).

190. Dunlop, J., Bowlby, M., Peri, R., Vasilyev, D. & Arias, R. High-throughput electrophysiology: an emerging paradigm for ion-channel screening and physiology. *Nat. Rev. Drug Discov.* **7,** 358–368 (2008).

191. Cao, G. *et al.* Genetically targeted optical electrophysiology in intact neural circuits. *Cell* **154,** 904–13 (2013).

192. Müller, J. *et al.* High-resolution CMOS MEA platform to study neurons at subcellular, cellular, and network levels. *Lab Chip* **15,** 2767–2780 (2015).

193. Berdondini, L. *et al.* Active pixel sensor array for high spatio-temporal resolution electrophysiological recordings from single cell to large scale neuronal networks. *Lab Chip* **9,** 2644 (2009).

194. Bargmann, C. I. Genetic and Cellular Analysis of Behavior in C. Elegans. *Annu. Rev. Neurosci.* **16,** 47–71 (1993).

195. Bargmann, C. I. Neurobiology of the Caenorhabditis elegans genome. *Science* **282,** 2028–33 (1998).

196. Riddle, D. L., Blumenthal, T., Meyer, B. J. & Priess, J. R. *C. elegans II*. *C. elegans II* (Cold Spring Harbor Laboratory Press, 1997).

197. Bakhtina, N. a. & Korvink, J. G. Microfluidic laboratories for C. elegans enhance fundamental studies in biology. *RSC Adv.* **4,** 4691–4709 (2014).

198. Chung, K. *et al.* Microfluidic chamber arrays for whole-organism behavior-based chemical screening. *Lab Chip* **11,** 3689–97 (2011).

199. Hulme, S. E. & Whitesides, G. M. Chemistry and the Worm: Caenorhabditis elegans as a Platform for Integrating Chemical and Biological Research. *Angew. Chemie Int. Ed.* **50,** 4774–4807 (2011).

200. Zeng, F., Rohde, C. B. & Yanik, M. F. Sub-cellular precision on-chip small-animal immobilization, multi-photon imaging and femtosecond-laser manipulation. *Lab Chip* **8,** 653–656 (2008).

201. Kaletta, T. & Hengartner, M. O. Finding function in novel targets: C. elegans as a model organism. *Nat. Rev. Drug Discov.* **5,** 387–399 (2006).

202. Solvas, X. C. i *et al.* High-throughput age synchronisation of Caenorhabditis elegans. *Chem. Commun.* **47,** 9801 (2011).

203. Wang, X. *et al.* Lab on a Chip Highly efficient microfluidic sorting device for synchronizing developmental stages of C. elegans based on deflecting electrotaxis. **15,** (2014).

204. Chung, K., Crane, M. M. & Lu, H. Automated on-chip rapid microscopy, phenotyping and sorting of C. elegans. *Nat. Methods* **5,** 637–643 (2008).

205. Ai, X., Zhuo, W., Liang, Q., McGrath, P. T. & Lu, H. A high-throughput device for size based separation of C. elegans developmental stages. *Lab Chip* **14,** 1746–52 (2014).

206. Gilleland, C. L., Rohde, C. B., Zeng, F. & Yanik, M. F. Microfluidic immobilization of physiologically active Caenorhabditis elegans. *Nat. Protoc.* **5,** 1888–1902 (2010).

207. Chokshi, T. V., Ben-Yakar, A. & Chronis, N. CO_2 and compressive immobilization of C. elegans on-chip. *Lab Chip* **9,** 151–157 (2009).

208. Hulme, S. E., Shevkoplyas, S. S., Apfeld, J., Fontana, W. & Whitesides, G. M. A microfabricated array of clamps for immobilizing and imaging C. elegans. *Lab Chip* **7,** 1515–1523 (2007).

209. Chronis, N., Zimmer, M. & Bargmann, C. I. Microfluidics for in vivo imaging of neuronal and behavioral activity in Caenorhabditis elegans. *Nat. Methods* **4,** 727–731 (2007).

210. Rohde, C. B., Zeng, F., Gonzalez-Rubio, R., Angel, M. & Yanik, M. F. Microfluidic system for on-chip high-throughput whole-animal sorting and screening at subcellular resolution. *Proc. Natl. Acad. Sci. U. S. A.* **104,** 13891–5 (2007).

211. Ma, H., Jiang, L., Shi, W., Qin, J. & Lin, B. A programmable microvalve-based microfluidic array for characterization of neurotoxin-induced responses of individual C. elegans. *Biomicrofluidics* **3,** 44114 (2009).

212. Dong, L., Cornaglia, M., Lehnert, T. & Gijs, M. A. M. Versatile size-dependent sorting of C. elegans nematodes and embryos using a tunable microfluidic filter structure. *Lab Chip* **16,** 574–585 (2016).

213. Han, B., Kim, D., Hyun Ko, U. & Shin, J. H. A sorting strategy for C. elegans based on size-dependent motility and electrotaxis in a micro-structured channel. *Lab Chip* **12,** 4128 (2012).

214. Gupta, B. & Rezai, P. Microfluidic Approaches for Manipulating, Imaging, and Screening C. elegans. *Micromachines* **7,** 123 (2016).

215. Rezai, P. *et al.* Electrotaxis of Caenorhabditis elegans in a microfluidic environment. *Lab Chip* **10,** 220–226 (2010).

216. Chokshi, T. V, Bazopoulou, D. & Chronis, N. An automated microfluidic platform for calcium imaging of chemosensory neurons in Caenorhabditis elegans. *Lab Chip* **10,** 2758–

2763 (2010).

217. Aubry, G., Zhan, M. & Lu, H. Hydrogel-droplet microfluidic platform for high-resolution imaging and sorting of early larval Caenorhabditis elegans. *Lab Chip* **15,** 1424–31 (2015).

218. Yan, Y. *et al.* A continuous-flow C. elegans sorting system with integrated optical fiber detection and laminar flow switching. *Lab Chip* **14,** 4000–4006 (2014).

219. Shanmugam, M. M. & Santra, T. S. Microfluidic devices in advanced caenorhabditis elegans research. *Molecules* **21,** 1–16 (2016).

220. Song, P., Dong, X. & Liu, X. A microfluidic device for automated, high-speed microinjection of Caenorhabditis elegans. *2015 Transducers - 2015 18th Int. Conf. Solid-State Sensors, Actuators Microsystems, TRANSDUCERS 2015* **11912,** 658–661 (2015).

221. Stiernagle, T. Maintenance of C. elegans. *WormBook* 1–11 (2006). doi:10.1895/wormbook.1.101.1

222. Yang, L. *et al.* A microfluidic diode for sorting and immobilization of Caenorhabditis elegans. *Biomed. Microdevices* **19,** 38 (2017).

223. Karbowski, J. *et al.* Conservation rules, their breakdown, and optimality in Caenorhabditis sinusoidal locomotion. *J. Theor. Biol.* **242,** 652–669 (2006).

224. Pierce-Shimomura, J. T. *et al.* Genetic analysis of crawling and swimming locomotory patterns in C. elegans. *Proc. Natl. Acad. Sci.* **105,** 20982–20987 (2008).

225. Fang-Yen, C. *et al.* Biomechanical analysis of gait adaptation in the nematode Caenorhabditis elegans. *Proc Natl Acad Sci U S A* **107,** 20323–20328 (2010).

226. Wen, Q. *et al.* Proprioceptive Coupling within Motor Neurons Drives C. elegans Forward Locomotion. *Neuron* **76,** 750–761 (2012).

227. Sznitman, J., Purohit, P. K., Krajacic, P., Lamitina, T. & Arratia, P. E. Material properties of Caenorhabditis elegans swimming at low reynolds number. *Biophys. J.* **98,** 617–627 (2010).

228. Park, S. *et al.* Enhanced Caenorhabditis elegans locomotion in a structured microfluidic environment. *PLoS One* **3,** e2550 (2008).

229. Gjorgjieva, J., Biron, D. & Haspel, G. Neurobiology of Caenorhabditis elegans Locomotion: Where Do We Stand? *Bioscience* **64,** 476–486 (2014).

230. Zhen, M. & Samuel, A. D. C. elegans locomotion: small circuits, complex functions. *Curr. Opin. Neurobiol.* **33,** 117–126 (2015).

231. Maguire, S. M., Clark, C. M., Nunnari, J., Pirri, J. K. & Alkema, M. J. The C. elegans touch response facilitates escape from predacious fungi. *Curr. Biol.* **21,** 1326–1330 (2011).

232. Xia, Y. & Whitesides, G. M. SOFT LITHOGRAPHY. *Annu. Rev. Mater. Sci.* **28,** 153–184 (1998).

233. Whitesides, G. M., Ostuni, E., Takayama, S., Jiang, X. & Ingber, D. E. Soft Lithography in Biology and Biochemistry. *Annu. Rev. Biomed. Eng.* **3,** 335–373 (2001).

234. McDonald, J. C. & Whitesides, G. M. Poly(dimethylsiloxane) as a material for fabricating microfluidic devices. *Acc. Chem. Res.* **35,** 491–499 (2002).

235. Korta, J., Clark, D. A., Gabel, C. V, Mahadevan, L. & Samuel, A. D. T. Mechanosensation and mechanical load modulate the locomotory gait of swimming C-elegans. *J. Exp. Biol.* **210,** 2383–2389 (2007).

236. Altun, Z. F. & Hall, D. H. INTRODUCTION TO C. elegans ANATOMY. (2017). doi:10.3908/wormatlas.1.1

237. Fabry, B. *et al.* Scaling the microrheology of living cells. *Phys. Rev. Lett.* **87,** 148102 (2001).

238. Schmidt, C. E., Horwitz, A. F., Lauffenburger, D. A. & Sheetz, M. P. Integrin-cytoskeletal interactions in migrating fibroblasts are dynamic, asymmetric, and regulated. *J. Cell Biol.* **123,** 977–91 (1993).

239. Hénon, S., Lenormand, G., Richert, A. & Gallet, F. A new determination of the shear modulus of the human erythrocyte membrane using optical tweezers. *Biophys. J.* **76,** 1145–51 (1999).

240. Steward, R. L., Cheng, C.-M., Ye, J. D., Bellin, R. M. & LeDuc, P. R. Mechanical stretch and shear flow induced reorganization and recruitment of fibronectin in fibroblasts. *Sci. Rep.* **1,** 147 (2011).

241. Krishnan, R. *et al.* Reinforcement versus fluidization in cytoskeletal mechanoresponsiveness. *PLoS One* **4,** e5486 (2009).

242. Ruthardt, N., Lamb, D. C. & Bräuchle, C. Single-particle tracking as a quantitative microscopy-based approach to unravel cell entry mechanisms of viruses and pharmaceutical nanoparticles. *Mol. Ther.* **19,** 1199–211 (2011).

243. Legant, W. R. *et al.* Multidimensional traction force microscopy reveals out-of-plane rotational moments about focal adhesions. *Proc. Natl. Acad. Sci. U. S. A.* **110,** 881–6 (2013).

244. Huang, H., Kamm, R. D. & Lee, R. T. Cell mechanics and mechanotransduction: pathways, probes, and physiology. *Am. J. Physiol. Cell Physiol.* **287,** C1-11 (2004).

245. Crocker, J. C. & Hoffman, B. D. Multiple-particle tracking and two-point microrheology in cells. *Methods Cell Biol.* **83,** 141–78 (2007).